**Development, Numerical Implementation, and Application of Methods to Simulate Solute Transport Processes in Porous Media Systems**

by

Vivek S. Bedekar

A dissertation submitted to the Graduate Faculty of
Auburn University
in partial fulfillment of the
requirements for the Degree of
Doctor of Philosophy

Auburn, Alabama
May 4, 2019



Approved by

Dr. T. Prabhakar Clement (Chair), Department of Civil Engineering
Dr. Jose G. Vasconcelos (Co-chair), Department of Civil Engineering
Dr. Ming-Kuo Lee, Department of Geosciences
Dr. Xing Fang, Department of Civil Engineering

## Abstract

Solute transport in porous media has been the attention of a plethora of studies over the last several decades. This research identifies gaps in existing knowledge within the realm of solute transport in porous media systems and has made several new contributions. The scientific contributions of this dissertation effort can be broadly classified into three categories: (1) development of numerical methods for solving solute transport equations; (2) implementing numerical modeling capabilities and solution techniques in solute transport simulators; and (3) application of numerical modeling simulators to understand transport processes in various real-world problems. The numerical modeling simulators involved in this research primarily comprise of simulators that are commonly known as MODFLOW-family of codes, owing the name to the underlying flow simulator called MODFLOW. MT3D is the associated solute transport simulator, SEAWAT is the variable-density flow and transport simulator, and RT3D is the reactive transport simulator, and all these codes use MODFLOW as the flow simulator. MODFLOW-USG and MODFLOW 6 are the latest versions of MODFLOW that, among other enhancements, offer unstructured grid capability.

As part of this research, a rigorous formulation for the dissolved and adsorbed mass storage for the finite-difference approximation of solute transport equation was developed. The new formulation for the convective form of equation conserves mass, an important consideration for solving solute transport equations. The reformulation was implemented in MT3D. Other improvements to MT3D include: incorporation of solute transport capabilities in the lake and stream flow; implementation of a contaminant treatment system to simulate above-ground pump and treat systems; multi-species kinetic reaction capabilities; and handling of transport within dry

model cells. The new version of MT3D was called MT3D-USGS, released by U.S. Geological Survey (USGS) as a public domain code.

During the development of MT3D-USGS code we discussed several transport issues with the MODFLOW-USG development team, including an inherent lack of capability in the governing equation of solute transport to handle any flow balance errors originating from an iterative flow solution, resulting in anomalous concentrations in the solute transport solution. To address this issue, we jointly developed a practical, new solution technique that stabilizes the concentration values. Finally, a new numerical code, DRT3D, was also developed by coupling reaction simulation capabilities of RT3D and density-dependent code SEAWAT.

Numerical models were developed to study several applied physical problems. First, the SEAWAT code was used to study the saltwater intrusion processes occurring within low-lying island aquifers. The study showed that lake formation on small islands can substantially deplete subsurface water resources. In a second study, the temporal trends of freshwater depletion and replenishment on small islands during dry and wet conditions were examined. The findings from this research suggest that freshwater is replenished at a faster rate relative to the depletion during dry conditions. Finally, the unstructured grid functionality offered by MODFLOW-USG was utilized to design coaxial circular grid cells to a variety of axisymmetric problems using the MODFLOW-USG modeling framework. The axisymmetric model design can also be implemented with the unstructured grid functionality offered by MODFLOW 6.

The research included here is a collection of studies that have contributed to the development of numerical methods, source code improvement, and application of the models for solving practical problems. The results of these research efforts were published in a peer-reviewed USGS report and four peer-reviewed journal publications.

**Acknowledgments**

First and foremost, I thank my advisor Dr. T. Prabhakar Clement, for being a constant source of support and encouragement. It was a joy to work with Dr. Clement who gave me ample freedom to pursue my research ideas and guided me throughout the research process. He is an excellent mentor and I enjoyed having lively debates with him during our research. I also thank him for the crucial financial support he provided during my studies.

While working on my PhD, I had a full-time job with S.S. Papadopulos and Associates, Inc (SSP&A). I could not have done my research work without full support from SSP&A. In particular, I thank Dr. Matthew Tonkin for inspiring me and giving me leeway from consulting work during critical periods of my studies enabling me to focus and work on my PhD. I also thank my colleagues at SSP&A who always encouraged me.

My family has played a vital role in supporting me during my studies over the past several years. I am grateful to my wife Prajakta, and my kids Shruti and Shreyas, who have encouraged me along the way. I deeply appreciate the role that my parents and my teachers from past schools and universities have played in laying the foundation that enabled me to carry my research.

I want to express my deep gratitude for those who have been a source of inspiration for me to work hard: Dr. Sorab Panday, Christopher Neville, Ashutosh Mahashabde, and Advait Khare. They have taught me the value of hard work and diligence. I also thank all my co-authors with whom I have worked during publication of this research.

I would be remiss not to acknowledge the administrative staff of Auburn University who have been outstanding in their responsiveness throughout my association with the university. Thanks to Auburn University for enabling me to work on my PhD as a distance learning student.

**Table of contents**

## List of Tables

## List of Figures

## List of Abbreviations

| | |
|---|---|
| 2D | Two-Dimensions or Two-Dimensional |
| 3D | Three-Dimensions or Three-Dimensional |
| AQTESOLV | AQuifer TEst SOLVer |
| ASTM | American Society of Testing and Materials |
| CTS | Contaminant Treatment System package of MT3D-USGS |
| DISU | Unstructured Discretization input file |
| DNAPL | Dense Non-Aqueous Phase Liquids |
| DOE | U.S. Department of Energy |
| DRT3D | Density-dependent RT3D |
| ET | Evapotranspiration |
| FEFLOW | Finite Element subsurface FLOW system software |
| LAK | Lake package of MODFLOW |
| LNAPL | Light Non-Aqueous Phase Liquids |
| LSM | Log Scaling Method |
| MODFLOW | Modular Flow, finite-difference flow simulation software |
| MODFLOW 6 | Sixth core version of MODFLOW |
| MODFLOW-SURFACT | HydroGeoLogic, Inc.'s version of MODFLOW |
| MODFLOW-USG | Unstructured grid version of MODFLOW |
| MT3D | Modular Transport, 3D, solute transport software |
| MT3DMS | Multi Species version of MT3D |
| MT3D-USGS | Version of MT3D released by USGS |
| NAPL | Non-Aqueous Phase Liquids |

| | |
|---|---|
| N-R | Newton-Raphson method |
| NCDC | National Climatic Data Center |
| NOAA | National Oceanic and Atmospheric Administration |
| PHT3D | Coupled PHREEQC-2/MT3D reactive transport software |
| RADMOD | MODFLOW preprocessor for axisymmetric models |
| RT3D | Reactive Transport, 3D software |
| SEAM3D | Sequential Electron Acceptor Model, 3D software |
| SEAWAT | Coupled MODFLOW/MT3D variable-density software |
| SFR | Stream Flow Routing package of MODFLOW |
| SIDS | Small Island Developing States |
| SSP&A | S. S. Papadopulos and Associates, Inc. |
| TDS | Total Dissolved Solids |
| TVD | Total Variation Diminishing |
| US EPA | United States Environmental Protection Agency |
| USGS | United States Geological Survey |
| UZF | Unsaturated-Zone Flow package of MODFLOW |

# Chapter 1. Introduction

## 1.1 Background

Solute transport models are widely used for simulating the fate and transport of contaminants in groundwater aquifers. Currently, several computer codes, with varying degrees of capabilities, are available for researchers and practitioners to simulate a wide range of groundwater contamination problems. On one end of the spectrum are simpler solute transport simulators that are based on analytical solutions that have several simplifying assumptions, but they are computationally efficient with simulation speed ranging from seconds to minutes. These tools are often used as screening level tools for performing quick order-of-magnitude calculations. Examples include BIOSCREEN (USEPA, 1996), CHEMFLO (USEPA, 2003), ATRANS (Neville, 2014), to name a few. On the other end of the spectrum are numerical simulation codes that are capable of simulating highly complex physical and chemical processes, with multiple components in multiple phases, multiple simulation domains, and are supported by large amounts of data for model calibration. These tools often require considerable computational resources (simulation speed varying from hours to days) and their efficiency depends on the size of the model domain and the processes that are being simulated. Examples of highly complex multi-component, multi-phase solute transport codes include TOUGH2 (Pruess, 1991), and STOMP (White and Oostrom, 2000); an example of vadose zone heat and solute transport code is HYDRUS (Šimůnek et al, 2006); and examples of large-scale surface water – groundwater interaction codes include MODHMS (HGL, 2011), MIKE SHE (DHI, 2004), HydroGeoSphere (HGS: Therrien et al, 2005), and PARFLOW (Maxwell et al, 2009).

For most of the practical applications related to solute transport modeling, more efficient simulators are preferred that can incorporate complexity sufficiently to represent all key physical

and chemical processes, and at the same time use certain simplifying assumptions that keep the simulation resource requirements within practical limits and yet yield results that are measurable and defensible. One important group of such practical and widely-used simulators are, what are commonly known as, the MODFLOW-family of codes.

MODFLOW (McDonald and Harbaugh, 1988) is the flow simulator developed by the U.S. Geological Survey (USGS). The first release of MODFLOW was in 1983 and since then several versions and variations of MODFLOW have been released (MODFLOW-2000: Harbaugh et al, 2000; MODFLOW-2005: Niswonger et al, 2011; MODFLOW 6: Langevin et al, 2017). MODFLOW is a finite-difference flow simulation software named after the 'modular' structure of the program in which each flow process and boundary condition could be invoked as a separate module. Although based on finite-difference approximations the MODFLOW code uses a control-volume approach rendering it, in effect, to work like a finite volume code. With this control-volume approximation, the flow, solute transport, variable-density flow and transport, and reactive transport simulations can be formulated using a mass conserved approach. More recently, Panday et al (2017), developed an unstructured grid version of MODFLOW, known as MODFLOW-USG, which uses a more flexible control volume approach that does not impose any restriction on the size and shape of the model grid cells.

Subsequent to the early releases of MODFLOW, a solute transport code called MT3D (Zheng, 1990) was developed. Flow solution provided by MODFLOW is used by MT3D to solve the solute transport equation. The initial release of MT3D was followed by several versions with various enhancements (MT3DMS: Zheng and Wang, 1999; MT3D'99: Zheng, 1999). The combined use of MODFLOW and MT3D codes enables the numerical simulation of solute transport in three-dimensional porous media. With the availability of MODFLOW and MT3D, a

variable-density flow and transport code called SEAWAT (Guo and Langevin, 2002; Langevin et al, 2007) was developed by coupling the two codes. Several variations of MT3D have also been developed to simulate reactive transport within porous media. The codes capable of simulating reactive transport include RT3D (Clement 1997, 2003), SEAM3D (Waddill and Widdowson 1998; Widdowson 2002), and PHT3D (Prommer et al. 2003). These consortium of simulation codes are commonly known as the MODFLOW-family of codes.

## 1.2 Knowledge Gaps and Research Questions

Our review indicated that currently available MODFLOW-family of transport codes have some inconsistencies in the way the storage term is represented when the non-conservative form of the transport equation is formulated. We also identified some limitations in the way in which currently available MODFLOW-family of transport codes account for mass balance errors. Additionally, we found that the axisymmetric conceptualization of flow and transport models is not fully validated.

Our review of saltwater intrusion modeling literature indicated gaps in scientific understanding of the impact of lake formation on the freshwater availability in small islands that have a negative water balance (potential evapotranspiration greater than precipitation). Furthermore, our review also indicated that the impacts of climate change and the related variations in the precipitation patterns on the changes in freshwater storage in small island aquifers is not fully understood. We further identified that reactions in conjunction with variable-density flow and transport have not been studied extensively.

The aim of this dissertation is to address some of the knowledge gaps identified above by answering the following research questions:

1. What is the appropriate treatment of storage term when the non-conservative form of the transport equation is formulated?
2. How should local flow imbalances be handled when solving solute transport equations?
3. How can we test and validate unstructured versions of the MODFLOW-family of codes used for simulating axisymmetric problems?
4. What are the impacts of lake formation on the freshwater availability of small islands that have a negative water balance?
5. What are the impacts of climate change and the related variations in the precipitation patterns on the changes in freshwater storage in small island aquifers?
6. What is the impact of reactions in an unstable variable-density flow system when denser water is sinking into, and reacting with, a less dense flow system?

## 1.3 Research Objectives

The specific objectives of this study are:

1. Derive storage term formulations for dissolved and adsorbed phases when the non-conservative form of the transport equation is formulated.
2. Address the limitations of solute transport equation in handling local flow imbalances in numerical models.
3. Conduct a benchmark analysis of axisymmetric modeling using the unstructured grid version of MODFLOW, MODFLOW-USG.
4. Study the impact of lake formation on the freshwater availability of small islands that have a negative water balance.

5. Develop a numerical simulator by combining the capabilities of SEAWAT and RT3D to study density-driven mixing and reactions of solute plumes with different densities.

## 1.4 Outline of the Dissertation Chapters

The MODFLOW-family of codes form the basis of this dissertation. The research topics presented in this dissertation can be organized into three broad categories: (1) development of numerical methods in solving solute transport equations; (2) implementing various numerical modeling capabilities and solution techniques within the MODFLOW-family of codes; and (3) application of numerical modeling tools to understand the transport processes in various real-world problems.

Chapter 2 of this dissertation provides a summary of the scientific contributions made while developing a new version of the MT3D code called MT3D-USGS. The MT3D code is a solute transport simulator capable of solving the advection-dispersion equation while considering equilibrium-controlled linear and non-linear adsorption, non-equilibrium adsorption, zeroth- and first-order degradation, and dual-porosity transport and offers various solutions schemes like the method of characteristics, finite-difference approximation, and total variation diminishing to solve the transport equation. As part of this research, several enhancements were made to the MT3D source code. A new mass conserved formulation was developed for the storage term in the convective form of solute transport equation. Other improvements to the MT3D code included: incorporation of solute transport capabilities in the lake and stream flow; implementation of a contaminant treatment system package to simulate above-ground pump and treat systems; multi-species kinetic reaction capabilities; and handling of transport within dry model cells. These improvements range from fundamental changes to the finite-difference

approximations of the governing equation, to simple representation of physical processes within the numerical model. In collaboration with the USGS, the enhancements to MT3D were released as an open source public domain code called MT3D-USGS and the details are documented in a peer-reviewed USGS report (Bedekar et al, 2016a). In addition, the storage formulation portion of this effort is currently being integrated into a journal article.

During the development of MT3D-USGS code we discussed several transport issues with the MODFLOW-USG development team (Panday et al, 2017; Panday, 2017), and during these discussions it came to light that the governing equation used for solute transport was not equipped to handle any flow balance errors originating from the flow solution. Numerical solutions using finite-difference approximations are most often solved using iterative methods that stop iterating when convergence is assumed to fall below a certain error tolerance. This could lead to flow balance errors that could result in anomalous concentrations in the solute transport solution. In order to address this issue, we jointly developed a practical, new solution technique that stabilizes the concentration values in the solute transport solution. Details of this novel solution technique are presented in Chapter 3. A journal article was published based on this study (Panday, Bedekar, Langevin, 2017a). My specific contribution included identification of the problem, jointly working with others to develop the solution, and contributing to the journal manuscript. I contributed substantially to this original research which is not included in any other theses or dissertations.

MODFLOW-USG belongs to the MODFLOW-family of codes that offers unstructured grid functionality with a control-volume finite-difference formulation. MODFLOW-USG provides flexibility to design model grids of any shape. Under this topic, MODFLOW-USG grids were uniquely designed using coaxial circular grid cells to simulate axisymmetric models

within the MODFLOW-framework. As part of this effort, we validated the axisymmetric solutions by comparing the MODFLOW-USG results of several benchmark problems that have well-tested solutions. Validity of axisymmetric models was tested by solving a pumping test problem, a vadose zone flow problem, and a saltwater intrusion problem within a circular island. The results of this model validation study are summarized in Chapter 4. A journal article has been published based on this study (Bedekar et al, 2019a).

As discussed in the previous section, SEAWAT is a variable-density flow and transport simulator that combines MODFLOW and MT3D codes. In this study, the SEAWAT code was used to study the saltwater intrusion processes occurring within low-lying island aquifers, and to examine the impacts of lake formation on freshwater availability in small islands. It was found that on low-lying islands with dry climates, where evapotranspiration exceeds rainfall, the freshwater storage can substantially decrease if sea level rise results in lake formation within interior topographic lows. The modeling study showed that lake formation on small islands can act like a pumping well that can divide the existing freshwater lens into smaller portions. The results of this field-scale modeling study are presented in Chapter 5. This work has been published in a journal article (Gulley, J., A. Mayer, J. Martin, and V. Bedekar, 2016). I was the lead, and the only, modeler in this modeling study and I completed all the modeling tasks, developed and ran the model, and closely coordinated with other authors to complete this work. This modeling effort was original research and the results are not included any other theses or dissertations.

As a follow-up to this study, we also conducted another modeling study using both experimental and numerical models to examine the temporal trends of freshwater depletion and replenishment on small islands under dry and wet conditions in island aquifers. The laboratory

investigations were completed by coordinating the efforts with our experimental team members at the University of Alabama. The findings from this research suggest that freshwater is replenished at a faster rate relative to the depletion occurring during dry conditions. Subsurface freshwater sustainability was also examined for shorter duration recharge events and the study found that the initial duration of groundwater recharge, even though for a short period, has a significant impact on freshwater replenishment. These results are summarized in Chapter 6. A journal article has been published based on this study (Bedekar et al, 2019b).

The final chapter of this dissertation presents the details of a new reactive transport code and a set of problems used for testing reactive transport processes involving dense plumes. A new numerical code, DRT3D, was developed by implementing reaction simulation capabilities of RT3D into the density-dependent code SEAWAT (note this code uses a combination of MODLOW, MT3D, and RT3D). The numerical solution obtained using DRT3D was qualitatively tested using a set of verification problems. The impetus for creating this benchmark study is: (1) to provide a simulation tool for designing and analyzing density enhanced mixing and reactions; and (2) to provide a proof of concept of density-enhanced mixing of a reactant for improving the performance of in-situ remediation at field sites. The details of the new code and the verification problems are presented in Chapter 7.

Chapter 8 provides a brief summary of all key findings of this dissertation and also provides some recommendations for future work.

## Chapter 2 – Development of MT3D-USGS

MT3D (Zheng, 1990) is a groundwater solute transport code which was developed by Dr. Chunmiao Zheng and was first released in 1990. Over the past 25 years, MT3D has become the industry standard for simulating groundwater solute transport problems and is one of the most widely used solute transport codes. This code has a modular structure and it works with the USGS flow code MODFLOW. Several updated versions of MT3D have been released over the past 25 years, one of the most significant being the inclusion of multiple species option, for which the code was renamed MT3DMS in 1999 (Zheng and Wang, 1999). As outlined by Zheng (2009), over the past two decades, simulation capabilities of MT3DMS have significantly expanded through new extensions and related codes, such as MT3D'99 (Zheng, 1999), RT3D (Clement 1997, 2003), SEAM3D (Waddill and Widdowson 1998; Widdowson 2002), and PHT3D (Prommer et al. 2003).

Since the first release of MT3D, various organizations have made several improvements to the MT3DMS code for solving several applied field problems. The objective of this work was to review some of these methods and develop a new version of MT3D that will have all these features, and also make MT3D fully compatible with all the recent packages available within the latest version of the USGS' MODFLOW code. The updated version of the code was called MT3D-USGS. The suffix USGS signifies that the code was released by USGS, not to be confused with the unstructured grid flow simulator MODFLOW-USG. MT3D-USGS supports only rectangular model cells and does not support the unstructured grids. Developments to MT3D-USGS were completed in Fall 2016.

The developments first address a fundamental improvement in the storage formulation of the solute transport equation when it is expressed in the convective form. The new formulation

conserves mass, an important consideration for solving the transport equation. The development of the new method is discussed in the next section. In addition to the reformulation of the storage term, several other features were also implemented in the MT3D-USGS code. All the key features are briefly described in the last section of this chapter.

## 2.1 Improvements in Fundamental Transport Solution Formulation

The governing equation for solute transport in porous media, when expressed in the divergence form, is equivalent to the convective form for steady-state uniform flow conditions. In transient flow conditions, the convective form of the transport equation does not conserve mass. To correct this, an additional term in the transport equation that accounts for the change in mass due to the change in volume of water is needed. In numerical solutions the additional term is often approximated in an inconsistent manner which leads to errors. The source of the error and the appropriate numerical treatment of this term for ensuring conservation of mass in groundwater flow simulations are presented in this work. The finite-difference numerical solution currently implemented in the widely used groundwater solute transport model MT3DMS is examined and a new alternative approach is discussed. In addition, four alternative numerical solutions to solve the change in adsorbed mass are examined and the applicability and limitations of each alternative solution is discussed. Although the use and the limitations of various alternative approaches presented in this work are discussed in the context of MT3D, the methods are applicable to all numerical models that solve the transport equation under unconfined flow conditions.

### 2.1.1 Governing Equations

The solute transport equation in porous media is based on the principle of mass conservation. The partial differential equation that is used to describe solute transport in porous media may be written as follows (Bear, 1979):

$$\frac{\partial(\theta C)}{\partial t} = -\frac{\partial(q_i C)}{\partial x_i} + \frac{\partial}{\partial x_i}\left(\theta D_{ij}\frac{\partial C}{\partial x_j}\right) + q_s C' + \sum R_n \qquad (2.1)$$

where, $\theta$ is the water content [$L^3/L^3$] defined as the volume of water per unit volume of porous media, C is the concentration [$M/L^3$], t is time [T], $q_i$ is the Darcy velocity [L/T], $x_{i,j}$ is distance along 3 Cartesian coordinate axes [L], $D_{ij}$ is the hydrodynamic dispersion tensor [$L^2/T$], $q_s$ is the volumetric flow rate of a source or sink per unit volume of porous media [$L^3/T/L^3$; or 1/T], C' is the concentration of a source or sink [$M/L^3$], and $\sum R_n$ are the chemical reaction terms [$M/L^3/T$]. The product of water content and concentration ($\theta C$) gives the mass of dissolved solute per unit volume of porous media, $M_d$ [$M/L^3$].

In equation 2.1, the first and second terms on the right-hand-side represent the total flow through porous media via advection and dispersion processes, respectively. The third term on the right-hand-side of equation 2.1 represents the addition and removal of mass to and from the system via sources and sinks, respectively. The final term, $\sum R_n$, represents various reaction terms, including decay, chemical reactions, and rate limited mass exchange with an immobile domain in dual porosity problems. The term appearing on the left-hand-side of equation 2.1 represents the change in mass with respect to time.

Equation 2.1 is referred to as the 'divergence' form of the transport equation. The inclusion of flow related terms, i.e. water content $\theta$ and the Darcy velocity $q_i$, within the differential operators enables the equation to express the change and movement of mass. This form of the

equation conserves mass and is therefore also called the 'conservative' form. A detailed discussion about the differences between the two forms of equations is presented in Diersch (2002).

Application of the product rule to the left-hand-side term of equation 2.1 to calculate the change in mass storage term as shown in equation 2.2, should be done if and only if the terms $\partial\theta$ and $\partial$C are small.

$$\frac{\partial(\theta C)}{\partial t} = \theta \frac{\partial C}{\partial t} + C \frac{\partial \theta}{\partial t} \tag{2.2}$$

An expression similar to equation 2.2 can be written for the advection term, $\frac{\partial(q_i C)}{\partial x_i}$, of the transport equation. By incorporating the continuity equation, the second term on the right-hand-side of equation 2.2 can be cancelled by a similar term obtained by applying the product rule to the advection term. The reduced form of the transport equation thus obtained is called the convective form, and is expressed as follows (Zheng and Bennett, 2002; Diersch, 2005).

$$\theta \frac{\partial C}{\partial t} = q_i \frac{\partial C}{\partial x_i} + \frac{\partial}{\partial x_i}\left(D_{ij} \frac{\partial C}{\partial x_j}\right) + q_s C' + \sum R_n \tag{2.3}$$

Note that the flow related terms in equation 2.3 are not within the differential operator. Equation 2.3 conserves mass under steady-state flow conditions, as the second term on the right-hand-side of equation 2.2 equals zero and if the Darcy velocity, $q_i$, remains uniform.

With the convective form of the transport equation, assuming a uniform velocity $q_i$ for the spatial derivative, $\frac{\partial(q_i C)}{\partial x_i}$, can become a significant source of error if the Darcy velocity across the distance $\partial$x changes considerably. However, the advective term can be implemented with a finite-volume approximation so that the advective flux is calculated at model cell faces, thereby

eliminating the need to use a single Darcy velocity for a finite control volume as discussed in the next section. For transient flow simulations, mass conservation for the mass storage change can be achieved by accounting for the change in the volume of water over time. This is achieved by including the term $C\frac{\partial\theta}{\partial t}$ introduced in equation 2.2 and applying appropriate numerical treatment of this term as discussed in the next section.

In the published literature, there are only two papers that the we are aware of that address issues related to solute storage change in transient flow problems with the use of convective form of equation. Goode (1992) pointed out some important issues and unacknowledged approximations in solute transport modeling. Goode (1992) highlights the importance of including fluid-storage change in the solute transport equation for transient flow problems in order to calculate transport velocities and to calculate dilution appropriately. Saaltink et al (2004) present a numerical formulation and temporal weighting scheme to conserve mass when using a convective form of transport equation by essentially including an additional term to account for fluid-storage change.

This work focuses on the change of solute mass with respect to time in transient flow problems. Next, we propose a corrected formulation to address the mass balance errors introduced by numerical solutions used with the convective form of the transport equation when the change in water content and concentration over a time-step is not insignificant. The widely used solute transport simulator MT3DMS (Zheng and Wang, 1999) is used for illustration and discussion of the proposed methodologies.

### 2.1.2 Solution to Inconsistencies in Dissolved Mass Storage Change

Solute transport simulation software like MODFLOW-SURFACT (Panday and Huyakorn, 2008) and HYDRUS (Šimůnek et al, 1998) solve the divergence form of the solute transport equation. The finite difference numerical solution implemented by both programs is:

$$\frac{\Delta(\theta C)}{\Delta t} = \frac{\theta^k C^k - \theta^{k-1} C^{k-1}}{\Delta t} \tag{2.4}$$

where, superscripts *k* and *k-1* represent the current and previous transport time-steps respectively. For the convective form of the transport equation, the finite-difference numerical solution is commonly implemented for equation 2.2, as shown in either equation 2.5 or 2.6.

$$\frac{\Delta(\theta C)}{\Delta t} = \theta^k \frac{\Delta C}{\Delta t} + C^k \frac{\Delta \theta}{\Delta t} \tag{2.5}$$

$$\frac{\Delta(\theta C)}{\Delta t} = \theta^{k-1} \frac{\Delta C}{\Delta t} + C^{k-1} \frac{\Delta \theta}{\Delta t} \tag{2.6}$$

where, $\Delta\theta$ is the change in volume of water per unit aquifer volume over the transport time-step and is calculated as $\theta^k - \theta^{k-1}$. Similarly, $\Delta C$ is the change in concentration over the transport time-step and is calculated as $C^k - C^{k-1}$. Equation 2.5 uses the current time-step value of water content and concentration while equation 2.6 uses water content and concentration from the previous time-step. MT3DMS (Zheng and Bennett, 2002) and VS2D (Healy, 1990) use equation 2.5 for temporal discretization of the storage term.

Alternatively, equation 2.4 can be used to derive the numerical implementation for the convective form as follows:

$$\frac{\Delta(\theta C)}{\Delta t} = \frac{\theta^k C^k - \theta^{k-1} C^{k-1}}{\Delta t} = \frac{\theta^k C^k - C^{k-1}(\theta^k - \Delta\theta)}{\Delta t} = \frac{\theta^k (C^k - C^{k-1}) + C^{k-1}\Delta\theta}{\Delta t} = \theta^k \frac{\Delta C}{\Delta t} + C^{k-1} \frac{\Delta \theta}{\Delta t} \tag{2.7}$$

Note that equation 2.7 is different than equations 2.5 and 2.6 in its treatment of the water content and concentration values. Equation 2.7 conserves mass, whereas both equations 2.5 and 2.6 do not conserve mass. Equations 2.5 and 2.6 either over or under calculate the rate of change of mass by either completely ignoring or by double counting the term $\Delta\theta\Delta C/\Delta t$.

Saaltink et al (2004) presented a temporal discretization scheme for solving the mass storage change term in which the concentration and water content time derivatives may be used at different time levels and called it a reverse time weighting scheme. Equation 2.8 of Saaltink et al (2004) uses equation 2.5 presented above, which if correctly implemented as shown in equation 2.7, would conserve mass. Saaltink et al (2004) highlight an important aspect of the convective form of transport equation: the advective term of the solute transport equation also needs to be corrected in the spatial derivative just as it is corrected in the temporal derivative. Alternatively, the advective flux term may use velocity at model cell faces as is done in MT3DMS (Zheng and Wang, 1999), thus avoiding the use of an averaged velocity $q_i$ across the model cell. Although Saaltink et al (2004) take a very different approach to the transient flow problem by imposing different temporal weights on the water content and Darcy velocity terms, they heuristically arrive at the same conclusion as derived in equation 2.7.

The expression derived in equation 2.7 provides a mass conservative numerical solution for using the convective form of the transport equation by: (1) including an additional term that accounts for the change in the volume of water over a transport time-step; and (2) appropriately using the concentration from the previous time-step to compensate for the approximation introduced by ignoring the term $\Delta\theta\Delta C/\Delta t$ when $\Delta\theta$ and $\Delta C$ are not insignificant. Equations 2.8 and 2.9 are two additional variants of equation 2.7 that present a mass conserved solution, suitable for using with the convective form of the transport equation.

$$\frac{\Delta(\theta C)}{\Delta t} = \theta^{k-1}\frac{\Delta C}{\Delta t} + C^{k}\frac{\Delta \theta}{\Delta t} \quad (2.8)$$

$$\frac{\Delta(\theta C)}{\Delta t} = \theta^{k-1}\frac{\Delta C}{\Delta t} + C^{k-1}\frac{\Delta \theta}{\Delta t} + \frac{\Delta \theta \Delta C}{\Delta t} \quad (2.9)$$

The correction derived in equation 2.7 for the finite volume approximation was implemented in MT3D-USGS. The problem described in the next section illustrates the impact of this change on the mass storage calculations. Results using the new formulation are compared against an analytical solution as well as the solution generated using MT3DMS version 5.3. MODFLOW (Harbaugh et al. 2000) was used for generating the flow solution.

### 2.1.3 Illustrative Example

A single model cell with a length of 10 meters in all three dimensions served as the problem for testing the new formulation. The model cell starts completely saturated, i.e. the initial head is equal to the top elevation of the cell with a porosity of 0.1. Hence, the total volume ($V_t$) of the model cell and the initial volume of water ($V_w$) in the model is 1,000 $m^3$ and 100 $m^3$, respectively. A conservative solute with an initial dissolved concentration of 100 $g/m^3$ (a total mass of 10,000 g) is simulated. A pump removes water at a rate of 25 $m^3$/day for 2 days (50 $m^3$) before injecting 50 $m^3$ of clean water (C' equal to 0.0) at the same rate over a period of 2 more days. In the first half of the simulation (2 days of extraction), half of the dissolved mass was removed from the system without affecting the concentration; in the second half of the simulation (2 days of injection of clean water) the mass remaining at the end of 2 days remained unchanged while the simulated concentration went down due to dilution. Variations in the simulated concentration and mass storage were examined with the following two numerical schemes: (1) Numerical scheme shown in equation 2.5 (as used in MT3DMS); (2) Storage formulation as derived in equation 2.7 (this option was called IALTFM = 2).

Figure 2.1 compares the solutions from the two numerical schemes with an analytical solution. The analytical solution is a simple dilution calculation for the second stress period that simulates injection of clean water. Because MT3DMS uses concentration from the current time-step, $C^k$ (equation 2.5), it is dependent on the time-step size used in the flow and transport model. As shown in Figure 2.1, the numerical solution is close to the analytical solution when a very small time-step size of 0.1 days is used. As smaller time-steps were used, the difference between $C^k$ and $C^{k-1}$ became smaller, and therefore, the solution using equation 2.5 approached the analytical solution. Despite this small time-step length, the calculated concentration is 51.2 g/m$^3$ at the end of 4 days – a 2% error compared to the analytical solution of 50 g/m$^3$. Increasing the time-step size exacerbated the error (Figure 2.1). For example, using a time-step size of 2 days led to a calculated concentration of 66.7 g/m$^3$, or a 33% error. Alternatively, the numerical solution that implements equation 2.7 (IALTFM = 2 in Figure 2.1) is independent of the time-step size because of the corrected storage calculation.

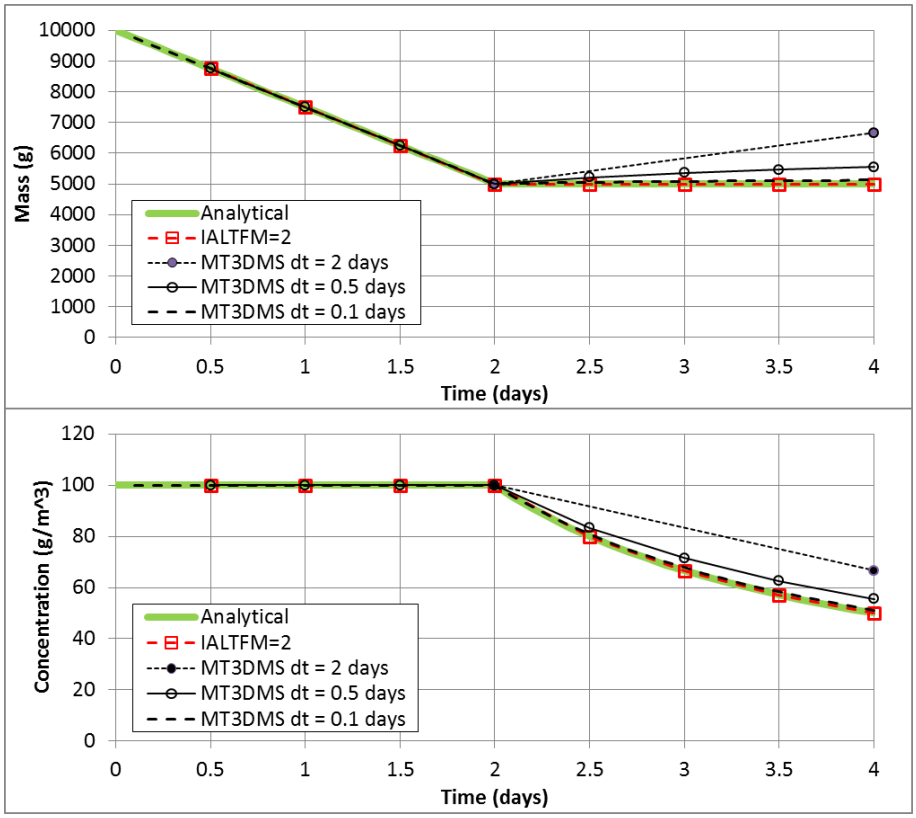


Figure 2.1 – Change in mass and concentration over time. Contaminated water is extracted for the first two days followed by injection of clean water for a period of 2 days.

It is important to note that the simulations in this example used the same time-step size for transport as was used in the flow solution. When using MODFLOW and MT3DMS, modelers often specify a smaller time-step size in the transport simulation as compared to the flow simulation to improve stability of the transport solution and/or minimize numerical dispersion. In situations where the transport step-size is smaller than the flow time-step size, due to either user specifications or model-reduced transport steps stemming from Courant or Peclet number restrictions, it is imperative that the volume of water used in the transport solution be interpolated for the current transport time-step. Furthermore, the mass recorded in the MT3DMS "mass output" file at the end of a transport time-step uses the volume of water reported for the end of a flow time-step, which may be significantly larger than the transport time-step. As a

result, the model underpredicts the calculated mass if the groundwater head drops during the flow time-step and can overpredict mass if the groundwater head rises within a flow time-step. However, since the concentration calculations use the rate of change in storage of water, which remains the same for a given flow time-step, concentration calculations are not affected by the head value at the end of flow time-step.

Another important aspect related to the need for head interpolation at the transport time-steps is to accurately calculate seepage velocities that affect advection as well as dispersion calculations. It is acknowledged that in implementing various storage formulations in MT3DMS, head interpolation at transport time-steps, to update the velocity calculations, was ignored. Not updating the velocities at the end of transport time-steps that are finer than the flow time-steps introduces error in velocity calculations but does not introduce flow balance errors even though the velocities are inaccurate. Goode (1992) discusses the errors introduced in the transport solution as a result of ignoring transient flow in transport simulations and how that affects the dilution and velocity calculations. When implementing velocity updates for each transport time-step, careful consideration is needed when a model layer converts from confined to unconfined flow or vice versa because the storage coefficient used by the flow solution switches between specific storage and specific yield, depending on the nature of the change in conditions. As a result, the volume of water considered by the change in mass storage will be different. However, for practical purposes the errors caused by ignoring the interpolation of head is small relative to uncertainty and variability inherent in model parameters (Goode, 1992). In MODFLOW and MT3DMS, this issue can be completely alleviated by using the same time-stepping levels in both flow and transport simulations.

### 2.1.4 Adsorbed Mass Storage Change

Another mass balance problem, which is quite similar to the one discussed above, occurs when simulating change in mass storage within a sorbing cell. Reversible instantaneous equilibrium adsorption models assume that the sorption-desorption processes are instantaneous, and that the dissolved and adsorbed concentrations are in equilibrium with each other. Total mass in the system is the sum of dissolved and adsorbed masses. Equation 2.2 represents the change in dissolved mass with time. Equation 2.10 presents the change in adsorbed mass with time.

$$\frac{\partial(M_s)}{\partial t} = \frac{\partial(\rho_b C_s)}{\partial t} \tag{2.10}$$

where, $M_s$ is the mass of contaminant adsorbed on soil per unit volume of porous media [M/L$^3$], $\rho_b$ is the bulk density defined as the mass of soil per unit volume of porous media [M/L$^3$], and $C_s$ is the sorbed concentration defined as the mass of sorbed solute per unit mass of soil [M/M]. Various isotherms define the relationship between the sorbed and dissolved phase concentrations. The discussion in this work is applicable to any equilibrium-controlled sorption isotherm, although the derivation and the illustrative examples considered below assume a linear sorption isotherm. Equation 2.11 shows the relationship between the sorbed and dissolved concentrations with a linear isotherm (Zheng and Bennett, 2002).

$$C_s = K_d C \tag{2.11}$$

where, $K_d$ is the distribution coefficient [L$^3$/M]. Total mass $M$ [M/L$^3$] can be calculated by adding the dissolved mass $M_d$ and adsorbed mass $M_s$. Change in total mass over time can be obtained by adding equations 2.2 and 2.10. For a linear isotherm, equation 2.11 can be used to

express adsorbed mass in terms of dissolved concentration. Equation 2.12 shows the change in total mass over time as,

$$\frac{\partial(M)}{\partial t} = \frac{\partial(\theta C)}{\partial t} + \frac{\partial(\rho_b C_s)}{\partial t} \tag{2.12}$$

Assuming a linear isotherm, as given by equation 2.11, the numerical solution for equation 2.10 can be written as:

$$\frac{\Delta(M_s)}{\Delta t} = \frac{(\rho_b K_d C)^k - (\rho_b K_d C)^{k-1}}{\Delta t} \tag{2.13}$$

Modeling codes like HYDRUS (Šimůnek et al, 1998) solve Richards' equation to simulate flow in vadose zone and have to keep track of saturation, for use in the transport equation, within all model cells. The MODFLOW-family of codes solve for hydraulic head by ignoring the complexities and non-linearities associated with unsaturated-zone by considering flow only within the saturated region. MT3DMS also considers only the saturated portion of the aquifer within a model cell. Transient flow problems pose a challenge in solving for the change in adsorbed mass within the thickness of the model cell over which the head varies from one flow time-step to the other especially when the adsorption is equilibrium controlled. For example, in transient flow, when the head falls in a groundwater system by Δh, say as a result of extraction pumping, the fate of the adsorbed mass over the height Δh largely depends on the nature of contamination and the soil type. The sorbed mass over the height Δh should be tracked and accounted for. Meanwhile, the adsorbed concentration for the saturated portion can change in the course of the pumping and the interval over which the head falls can potentially have a different sorbed concentration. The adsorbed mass associated with the height over which the head falls needs to be integrated to fully account for the mass that exists in the desaturated portion of the soil column. From the simulation standpoint, this adsorbed mass does not participate in the

transport processes within the saturated portion of the soil column. Conversely, the adsorbed mass within the dewatered portion of the soil column is relevant when the head rises and the sorbed mass reenters the saturated portion of the groundwater system.

In numerical solutions, detailed tracking of the sorbed mass separately for various heights within a grid block can become a cumbersome task. Selecting a number of discrete sections over which sorbed mass is separately tracked for each individual section will be problem specific and a generic sub-discretization scheme that will satisfy all situations is not possible. The only alternative, even with vadose zone simulators, is to use a finer vertical discretization if detailed sorbed mass tracking is desired. To implement a numerical solution that assumes uniform concentration over the entire grid block, certain approximations have to be made. Four alternative numerical solutions are examined here to solve for the change in total mass with respect to time within a sorbing system. The results obtained using the four alternate solutions were compared to the solution provided by MT3DMS. All four alternatives presented here are applicable to both the divergence as well as the convective form of equations.

To examine the issues related to the adsorbed mass changes with transient flow, we reconsider the illustrative example presented above with adsorption/desorption. The model cell with a total volume of 1,000 $m^3$ and a porosity of 0.1 was initially specified as fully saturated. At the end of the 2-day extraction period, the saturated volume of the model cell was 500 $m^3$. During the following two days, the injection of clean water makes the model cell fully saturated again. Consider an equilibrium controlled linear isotherm with a distribution coefficient $K_d$ of 0.1 L/kg. With an initial dissolved concentration of 100 $g/m^3$ (or mg/L), the initial sorbed concentration is 10 mg/kg. Using a bulk density ($\rho_b$) of 1.5 kg/L, the initial sorbed mass in the model cell is 15,000 g. Thus, the initial total mass in the model cell is 25,000 g.

#### 2.1.4.1 Alternative 1

The first alternative assumes that the full model cell thickness of every model cell is available for sorbed mass storage. Furthermore, this alternative is useful regardless of whether the vadose zone is simulated in MT3DMS or not. When the unsaturated zone is simulating using the MODFLOW/MT3D pairing, the Unsaturated-Zone Flow package [UZF1; Niswonger et al (2006)] calculates and passes flux and storage terms in the unsaturated zone to a modified version of MT3DMS that simulates variably saturated transport (Morway et al, 2013). Among the modifications, a residual water content is maintained for each model cell wherein variable saturated flow is simulated. This approach assumes that the water content varies within the specific yield space of the grid block, or in other words is in addition to the residual water content. Thus, the water content, $\theta$, in this alternative is the total water within the grid block divided by the volume of the grid block. Figure 2.2 (1) shows a schematic for this alternative.

When the unsaturated zone is not explicitly simulated, water within the saturated portion of the grid block is assumed to be 'smeared' throughout the full model cell thickness for the adsorption process to occur in. That is, a continuous film of water is assumed to cover the soil particles over the entire model cell. Using this alternative approach, the water content for the grid block is variable with changing volume of water. Since the volume of porous media under consideration does not change with time, equation 2.13 can be simplified as follows.

$$\frac{\Delta(M_s)}{\Delta t} = \rho_b K_d \frac{C^k - C^{k-1}}{\Delta t} = \rho_b K_d \frac{\Delta C}{\Delta t} \tag{2.14}$$

The total change in mass can be computed by adding equations 2.7 and 2.14. Equation 2.15 shows the result of adding the two equations and rearranging the terms.

$$\frac{\Delta M}{\Delta t} = \frac{\Delta M_d}{\Delta t} + \frac{\Delta M_s}{\Delta t} = \theta^k \left(1 + \frac{\rho_b K_d}{\theta^k}\right) \frac{\Delta C}{\Delta t} + C^{k-1} \frac{\Delta \theta}{\Delta t} = \theta^k R^k \frac{\Delta C}{\Delta t} + C^{k-1} \frac{\Delta \theta}{\Delta t} \tag{2.15}$$

Where, $R^k$ is the retardation factor calculated at the end of each transport time-step as shown in equation 2.15. Note that the retardation factor $R$ is required to be calculated at each transport time-step along with the updated water content. Since the entire model cell thickness is considered in alternative 1 and it may not be fully saturated, water content and porosity cannot be interchangeably used.

Figure 2.3 shows the results using alternative 1. As expected, the total mass removed in the first two days is equal to the total extraction volume of water multiplied by the dissolved phase concentration, or 5,000 g, the dissolved phase concentration remains constant at 100 g/m$^3$. During the second stress period (days 3 and 4), the injection of clean water dilutes the dissolved phase concentration. Using alternative 1, the calculated dissolved concentration is 80 g/m$^3$ at the end of the injection period. Recalling that approximately 20% of the initial mass (5,000 g of the total initial mass of 25,000 g) was removed from the system, a 20% reduction in concentration for the same volume of water makes sense.

Alternative 1 assumes the sorbed mass to be 'smeared' over the entire grid block. A very small saturated thickness within a large model cell (small water content) results in a large retardation factor. In MODFLOW/MT3D models that simulate variably saturated conditions, if the water content is expected to approach zero, this alternative will lead to very high retardation factor, resulting in a very slow-moving plume. This alternative should be avoided if small saturated thicknesses are expected in a model cell that does not solve for vadose zone conditions. On the other hand, this alternative, is suitable for vadose zone flow simulations in which a residual water content is always expected to be present.

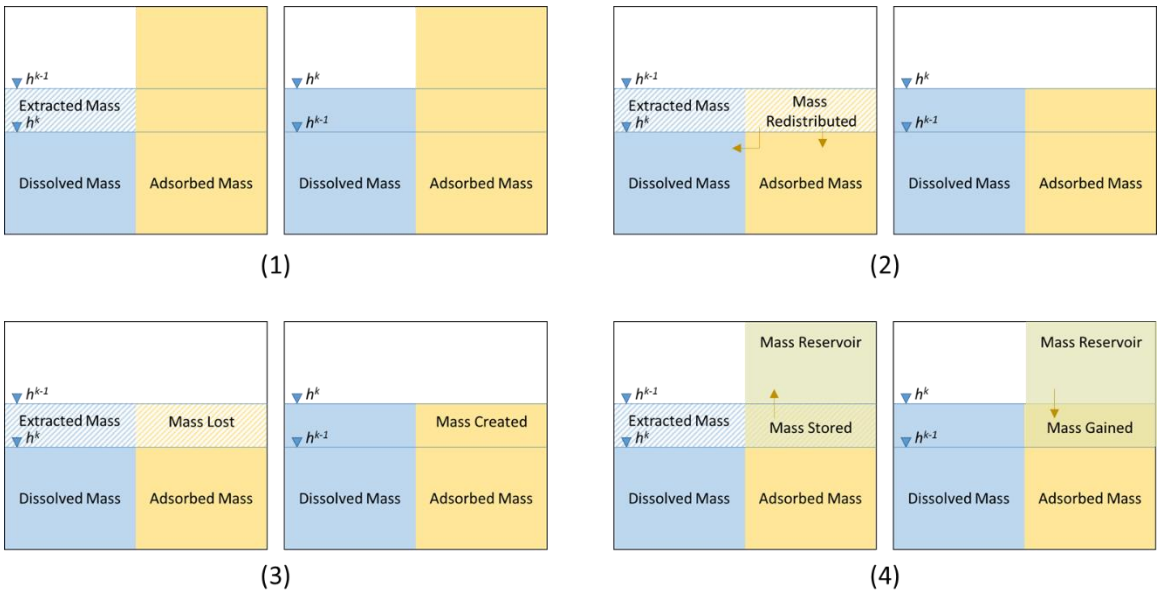


Figure 2.2 – Schematic illustrating alternatives for solving adsorbed mass storage: (1) Alternative 1 stores sorbed mass in full cell thickness, retardation factor changes with water content; (2) Alternative 2 conserves and redistributes the mass from the desaturated region of the cell among the dissolved and solid phases within the saturated region of the cell as calculated at the end of the transport step ($\Delta h = h^k - h^{k-1}$); (3) Alternative 3 removes or creates mass, depending upon the respective $\Delta h$ during the transport step; and (4) Alternative 4 implements a solid-phase mass reservoir that allows mass within the $\Delta h$ region of the grid cell to be stored and recaptured from the reservoir as the water table rises and falls.

#### 2.1.4.2 Alternative 2

This alternative assumes that the sorbed concentration resides only within the saturated portion of the model cell. To conserve mass in transient flow conditions, when the head falls in a groundwater system by $\Delta h$, the sorbed mass within the $\Delta h$ portion of the cell is redistributed among the dissolved and sorbed phases within the saturated volume of the cell as calculated at the end of the transport step. Conversely, when the head rises within a time-step by $\Delta h$, the total mass, dissolved and sorbed, from the saturated portion before the head rise is redistributed over the new saturated volume into both the dissolved and adsorbed phases. Figure 2.2 (2) shows a schematic for this alternative.

Since only the saturated portion of the model cell is considered, equation 2.13 needs to be rewritten to include the saturation term as shown below.

$$\frac{\Delta(M_s)}{\Delta t} = \frac{(S\rho_b K_d C)^k - (S\rho_b K_d C)^{k-1}}{\Delta t} \quad (2.16)$$

where, $S$ is the dimensionless saturation. In MODFLOW and MT3D, saturation in unconfined flow conditions can be calculated as the fraction of the model cell that is saturated. For confined conditions, $S$ equals 1 and equation 2.16 reduces to equation 2.13. Solving equation 2.16 further:

$$\frac{\Delta(M_s)}{\Delta t} = \rho_b K_d \frac{S^k C^k - S^{k-1} C^{k-1}}{\Delta t} = \rho_b K_d \frac{S^k C^k - C^{k-1}(S^k - \Delta S)}{\Delta t} = \rho_b K_d S^k \frac{\Delta C}{\Delta t} + \rho_b K_d C^{k-1} \frac{\Delta S}{\Delta t} \quad (2.17)$$

where, $\Delta S$ is the change in saturation over the transport time-step calculated as $S^k - S^{k-1}$. Saturation can be expressed in terms of water content $\theta$ and porosity $\theta_s$ using the relation $S = \theta/\theta_s$. Equation 2.17 expresses the change in total mass over time for alternative 2 by using the described relationship between saturation and water content and by adding equations 2.7 and 2.15.

$$\frac{\Delta M}{\Delta t} = \frac{\Delta M_d}{\Delta t} + \frac{\Delta M_s}{\Delta t} = \theta^k \left(1 + \frac{\rho_b K_d}{\theta_s}\right) \frac{\Delta C}{\Delta t} + C^{k-1} \left(1 + \frac{\rho_b K_d}{\theta_s}\right) \frac{\Delta \theta}{\Delta t} = \theta^k R \frac{\Delta C}{\Delta t} + C^{k-1} R \frac{\Delta \theta}{\Delta t} \quad (2.18)$$

Note that the retardation factor, $R$, calculated in equation 2.18 is constant since it uses porosity, which does not change with time.

Figure 2.3 shows the change in concentration and total mass in the model cell. The numerical solution presented in equation 2.18 redistributes the adsorbed mass from the saturated portion of the model cell in the previous transport time-step level ($k$-1) to the current transport time-step level ($k$). Note that the mass remaining in the system at the end of the two-day extraction period is 18,662 g/m3, which is less than a value of 20,000 g/m3 as calculated by alternative 1. The reduction in concentration and mass as compared to alternative 1 is a result of

the redistribution of the sorbed mass at each transport time-step, which increases the dissolved concentration and ultimately results in increased mass extraction by the pumping well.

While this alternative approach conserves mass, it is apparent that the concentration variation, although theoretically correct, is not plausible in reality. This alternative demonstrates that the scaling of mass calculated in the sorbed phase with the saturation of a model cell leads to mass conservation but seemingly implausible concentrations.

#### 2.1.4.3 Alternative 3

This alternative assumes that the sorbed mass only resides within the saturated portion of the model cell, similar to the approach described in the previous alternative, but with the following variation. In this alternative, the sorbed mass residing within the dewatered portion of the cell is unavailable to the saturated portion of that model grid cell and is therefore 'lost' from the system. When the head in the model cell increases, owing to the instantaneous equilibrium assumption, a 'gain' in the sorbed mass is assumed. The 'loss' and 'gain' of sorbed mass resulting from the use of alternative 3 is accounted for as a source/sink term in the numerical solution. Figure 2.2 (3) shows a schematic for this alternative.

The numerical solution for this approach uses equation 2.18 together with an additional term $M_{loss/gain}$. This term helps conserve mass from the perspective of the numerical simulation. The $M_{loss/gain}$ term is a way to account for the lost or gained mass as a result of transient flows and is defined in equation 2.19.

$$M_{loss/gain} = \rho_b K_d C^* \frac{\Delta S}{\Delta t} = C^* \frac{\Delta \theta}{\Delta t}(R-1) \tag{2.19}$$

where, $C^*$ is the concentration associated with the loss or gain. $C^*$ is equal to $C^{k-1}$ when $\Delta\theta$ is negative, i.e. in case of falling head and is equal to $C^k$ when $\Delta\theta$ is positive, i.e. in case of rising

head. The $M_{loss/gain}$ term is added to the right-hand-side of equation 2.18 to compute the change in total mass. MT3DMS, in effect, uses a similar approach as is used by alternative 3 except that it simulates the 'loss' and 'gain' of sorbed mass, but does not track or report the loss/gain.

Figure 2.3 shows the resulting concentration and mass change under the alternative 3 formulation. Note that at the end of the first two days of pumping, only 12,500 g of mass was remaining in the groundwater system. Of the 12,500 g that was removed from the system, 5,000 g (of dissolved mass) was extracted out via the pumping well and 7,500 g (of sorbed mass) was 'lost' as a sink to the term $Q_{loss/gain}$ with the lowering of head. Similarly, with increasing head sorbed mass was created. The resulting concentration at the end of injection period was 76.9 $g/m^3$.

The mass that is lost could be thought of as the mass that physically resides in the portion of the soil column that was desaturated during pumping. The gain in mass could be thought of as the mass that is gained back from the portion of the grid block that was previously desaturated as the water table rises. This alternative is not without its drawbacks. If the soil into which the water table is rising is 'clean', this alternative approach will create mass, that would be unreasonable. The gain of mass with re-saturation is arbitrary and depends on the dissolved concentration at the time that re-saturation occurs.

#### 2.1.4.4 Alternative 4

Alternative 4 is an extension to Alternative 3. The mass that is lost to the sorbed portion of the model cell is stored as a 'reservoir' and is reintroduced into the system as the water table in a model cell rises. The advantage of this alternative (over alternative 3) is that the reintroduced mass is not arbitrary and has some physical basis of how much sorbed mass exists in the system at the time water table rises. Figure 2.2 (4) shows a schematic for this alternative.

Alternative 4 adds the term $M_{sorb}$ to equation 2.18. For falling head, the additional term is similar to equation 2.19 used in Alternative 3, with the only difference being that the calculated term is saved in memory to account for the mass that is stored in the 'reservoir'. This stored mass is used for mass calculations and to calculate the amount of mass that is reintroduced into the system as a source when the water table rises. Equations 2.20 and 2.21 define the $M_{sorb}$ term for falling and rising head respectively.

$$M_{sorb} = C^{k-1}\frac{\Delta\theta}{\Delta t}(R-1) \tag{2.20}$$

$$M_{sorb} = M_{stor} \times f \tag{2.21}$$

where, $M_{stor}$ is the total mass stored in the unsaturated zone of a partially saturated model cell per unit volume of the porous media [M/L$^3$], and $f$ is the fraction of the unsaturated zone that gets re-saturated over a time-step.

Figure 2.3 shows that the total mass calculated in the model cell is conserved without losing mass during extraction or creating mass during injection, similar to alternative 1. Concentration at 2.5 days, immediately after injection starts, is very similar to alternative 3 but by the end of 4 days the final concentration using alternative 4 is calculated at 80 g/m$^3$, which is the same result obtained using alternative 1. Alternatives 1 and 4 generate similar results because the sorbed mass is stored over the entire cell thickness. However, alternative 1 is capable of generating unrealistically high retardation factors leading to incorrect solutions in multi-cell simulations that are more complex than this illustrative example.

In one particular situation, alternative 4 will lead to underestimation of sorbed concentration. If sorbed mass is present only within a small portion of a model cell and water level change is expected only within that small portion of the model cell, then the storage of

sorbed mass with alternative 4 over the entire thickness of the unsaturated zone within the model cell will lead to underestimation of sorbed concentration because the sorbed mass within the ‘reservoir’ will be ‘smeared’ over the entire unsaturated zone. In such a situation, alternative 3 may be a better option to use if a drastic variation in dissolved concentration is not expected.

For most ’real-world’ circumstances, Alternative 4 is the recommended alternative. This approach conserves mass and provides a reasonable and practical approximation for solving adsorption and desorption processes.

Clearly, all alternatives presented here have their advantages and drawbacks as discussed above. These alternatives are presented to demonstrate the use of various assumptions in solving the change in adsorbed mass within unconfined systems and the use of appropriate alternatives will depend on the situation that it is being modeled. Finer vertical discretization will help lower the impact of the above approximations. These alternatives provide the basis to achieve a numerical solution within the confines of modeling codes like MT3DMS that solve only the saturated groundwater system.

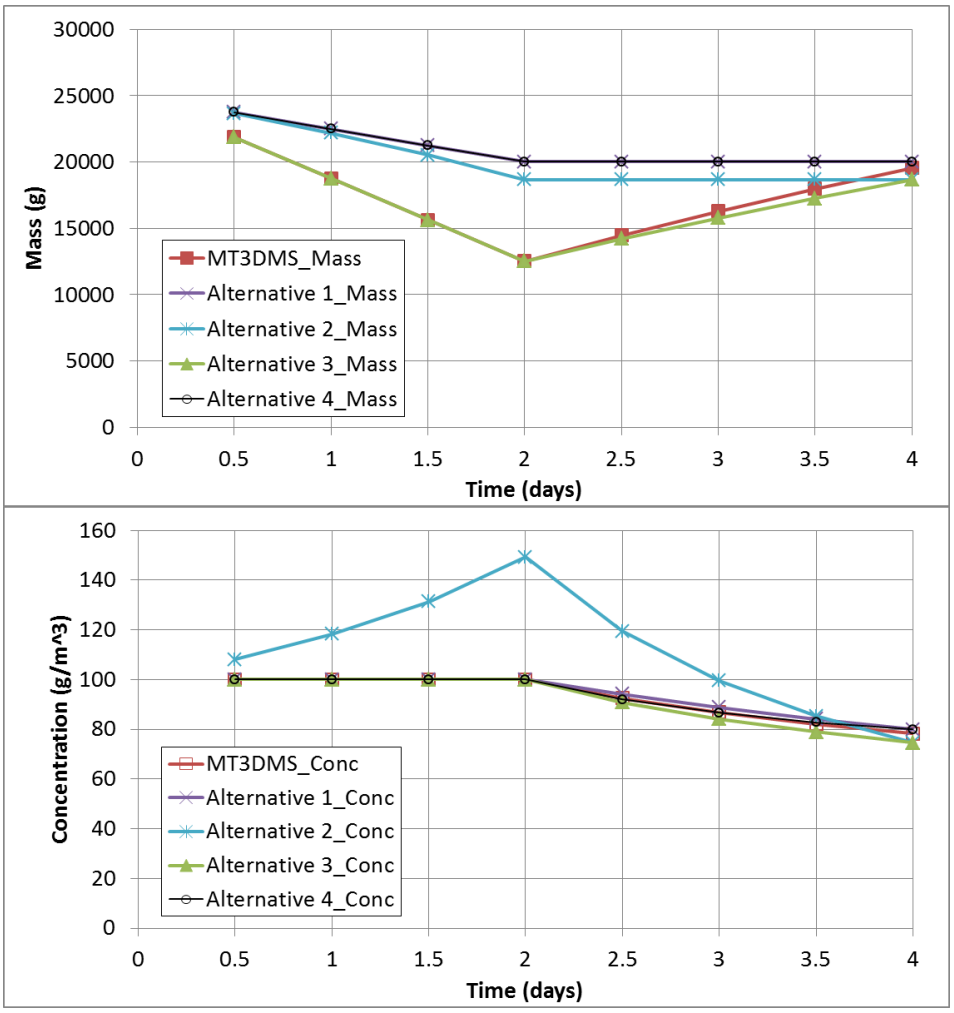


Figure 2.3 – Change in concentration for a non-conservative solute in transient flow

### 2.1.5 Discussion of Related Issues

The calculations presented above are based on the assumption that the flow volumes are balanced within a model cell, i.e. the difference between the inflow and outflow equals change in storage of water. For unconfined conditions, the flow model uses specific yield for calculating the change in storage. The storage formulation for solute transport presented above will lead to errors if the porosity used for transport calculations is different than the specific yield used in the flow calculations. Using a porosity value less than specific yield is physically implausible. Porosity values greater than specific yield, where necessary, will need special treatment for the

volume of water that exists is the difference between the porosity and the specific yield space as is shown by Panday and Huyakorn (2008, equation 26). That aspect of the transport formulation is beyond the scope of this work. However, it should be noted that any transport formulation, including the formulations presented in this work, will lead to meaningful answers only when specific yield is equal to porosity.

Analogous to the above discussed flow imbalance resulting from the possibility of specific yield being smaller than porosity, we acknowledge that there is an inherent flow imbalance in case of dual porosity problems. For unconfined conditions, if the flow model is solved only for a single porosity but the accompanying transport model is simulated as a dual porosity problem, then that will lead to another type of flow imbalance. As an example, consider a MODFLOW and MT3DMS simulation that solves only the saturated portion of the groundwater system; the flow model MODFLOW calculates a head solution based on the change in stored water that is based on the specific yield. MT3DMS solves only the saturated portion of the aquifer and therefore a change in head also results in a change in immobile water content thereby creating a flow imbalance that fails to account for the water gain/loss within the immobile portion of the aquifer. However, the errors arising from the imbalance in the immobile domain can be minimized by: (1) using a small value for immobile porosity; (2) controlling the flow time-step size so that the head value does not change drastically from one flow time-step to the other; (3) using a constant volume of immobile water within the immobile domain similar to the formulation implemented in the UZF1 package, as presented in this work as alternative 1; or (4) by using a dual porosity flow model that would maintain flow balance within the flow model.

### 2.1.6 Summary of Storage Formulation

We present the details of a mass conservative numerical solution that introduces an additional term in the convective form of the transport equation. The derived numerical solutions show that the use of concentration from the previous transport time-step, $C^{k-1}$, provides a more accurate solution as compared to using $C^{k}$. It is also shown that the use of smaller time-steps reduces the difference between the results obtained by $C^{k-1}$ and $C^{k}$. In flow solutions that use coarser time-steps as compared to the finer transport time-steps, for accuracy of mass calculations, it is important to use the interpolated volume of water at transport time-steps.

When calculating changes in sorbed mass for a non-conservative solute in transient flows, four alternative numerical solutions are presented. Alternative 1 uses the entire model cell thickness to calculate change in sorbed mass. Although it conserves mass, it is not robust. The retardation factor may drastically increase for very low water content slowing down the movement of a plume. This alternative is suitable for vadose zone flow and transport simulations. Alternatives 2, 3, and 4, use only the saturated portion of the model cell and are tailored to MT3DMS's saturated-only approach. All three approaches use a constant retardation factor calculated using the porosity and conserve mass. Alternative 2 redistributes mass from the saturated portion of the previous time-step to the saturated portion of the current time-step. This instantaneous redistribution of mass may generate implausible concentrations. Alternative 3 allows the mass in the sorbed portion to be lost or created to account for sorbed mass in the desaturated or newly saturated portion of the model cell. This alternative creates mass arbitrarily based on the dissolved phase concentration at the time water level rises. Alternative 4 is similar to alternative 3 but stores and tracks the mass stored in the unsaturated portion of a partially saturated model cell. Rewetting of a cell introduces the stored mass back into the groundwater

system and has some physical basis of desorption. Although each alternative has some drawbacks and requires careful consideration depending on the nature of the problem being modeled, alternative 4 is the recommended alternative for most perceived situations.

All the numerical solutions examined in this work will provide meaningful results if and only if the flow balance is maintained within a cell, irrespective of whether the divergence or the convective form of the transport equation is used. In order to ensure that flows are balanced in unconfined flow conditions, the specific yield used in the flow model must be set equal to the porosity value used in the transport model. This work also acknowledges the errors due to flow imbalances that occur when dual porosity transport is simulated with a single porosity flow model.

Finally, to alleviate the errors introduced in the transport solution in transient flow problems, one or all of the following steps can be implemented to improve the overall accuracy of the solution:

- Use finer temporal discretization within the flow model to minimize the change in head in one flow time-step. This can be achieved by using small time-steps, especially at the beginning of a stress period when the rise or fall of head due to stresses is most severe;
- Use the same time-stepping in flow and transport simulations, inasmuch is feasible;
- Use finer vertical discretization to track sorbed mass within the system for transient flow conditions; and,
- For non-conservative transport simulations, use a variably saturated modeling code; especially if saturated flow models fail to achieve the modeling objectives.

## 2.2 Other Novel Features Implemented in the New MT3D-USGS Code

Following are the list of new features that were implemented into the new open source public domain code MT3D-USGS (Bedekar et al, 2016b):

- A new capability was added to simulate solute transport in two important MODFLOW surface water packages including the lake (LAK) and stream flow routing (SFR) packages. A flexible space and time weighting scheme was implemented for solving stream transport (Bedekar et al, 2013).

- The original version of the MT3DMS code works well with MODFLOW, a widely used finite-difference groundwater flow simulator. All MODFLOW versions through MODFLOW-2005 had a limitation in handling the non-linearity of the unconfined flow equation. Newton-Raphson (N-R) formulation in combination with upstream weighting, and numerical techniques like backtracking and under-relaxation provides an efficient, stable, and robust solution to the non-linear unconfined flow equation. As part of this effort, a new N-R linearization scheme was implemented in MODFLOW-2000 (Harbaugh et al, 2000) and USGS implemented it in MODFLOW-2005 (Niswonger et al, 2011). Details of this implementation and comparison of these codes with earlier codes was published in a research paper (Bedekar et al, 2012a).

  With the introduction of the N-R formulation to MODFLOW, it became essential to handle 'dry' but active model cells in MT3DMS. MT3DMS was designed to work with MODFLOW which would deactivate a model cell that became dry, i.e. head in that cell falls below the bottom elevation of the model cell. The N-R formulation with upstream weighting allows water to flow through dry cells. If not handled properly, MT3DMS stops any flow to dry cells resulting in mass accumulation in the cell upstream of a dry cell creating anomalous

concentrations. Code was added in MT3DMS to handle this situation so that a mass accounting approach conserves mass entering and leaving dry model cells and avoids incorrect concentration calculation (Bedekar and Tonkin, 2011).

- A new package called the Contaminant Treatment System (CTS) package was added to simulate mass movement via above ground pump-and-treat systems with various contaminant treatment options. This capability was added to support pump-and-treat operations at the DOE Hanford Site (Bedekar et al, 2011).
- A number of chemical reaction options were added to MT3DMS, similar to and verified against, some of the capabilities available in RT3D (Clement, 1997): (1) Instantaneous reaction between two species (similar to the capability available in BIOPLUME: US EPA, 1998); (2) MONOD kinetics (Monod, 1949); (3) First-order parent-daughter chain reaction (Clement, 1997); and (4) Kinetic reaction between multiple electron donors and acceptors (Clement, 1997; Lu et al, 1999).

# Chapter 3 – Impact of Local Groundwater Flow Model Errors on Transport and Development of an Improved Numerical Solution

A groundwater flow model is typically used to provide the flow field for conducting groundwater solute transport simulations. The advection term of the mass conserved formulation for groundwater transport assumes that the flow field is perfectly balanced and that all water flowing into a numerical grid cell is exactly balanced by outflows after accounting for sources/sinks or internal storage. However, in many complicated regional or site-scale models, there may be localized flow balance errors that may be difficult to eliminate through tighter flow convergence tolerances due to simulation time constraints or numerical limits on convergence tolerances. Thus, if water is erroneously gained or lost within a grid cell during the flow computation, the solutes within it will also be numerically affected in the associated transport simulation. Transport solutions neglect this error in groundwater flow as the transport equations that are solved assume no error in flow. This flow imbalance error can however have consequences on the transport solution ranging from unnoticeable errors in the resulting concentrations to spurious oscillations that can grow in time and hinder further solution. An approach has been suggested here to explicitly handle these flow imbalances during mass conserved advective transport computations. These errors are reported in the corresponding transport mass balance output as corrections that are needed to handle errors originating in the flow solution. Example problems are provided to explain the concepts and demonstrate the impacts.

## 3.1 Background

Numerical simulations of groundwater transport are typically conducted for evaluation of migration and remediation of solutes in groundwater. A desirable solution scheme therefore

should conserve mass, avoid spurious oscillations and minimize numerical dispersion errors. Mass conservative transport schemes (Bedekar et al. 2016a) are preferred in many situations because solute amounts are important to an investigation and loss or gain of substantial quantities of mass due to numerical reasons is not an acceptable outcome. Mass conservative advection transport schemes use the flow of water from one numerical cell to its neighbor to carry solutes with it, while the convective form of the transport equation uses an average cell velocity and therefore need not conserve solute mass (Saaltink et al. 2004). For transport simulations in a transient flow field, mass conservation errors may also arise from the change in fluid storage, as noted by Goode (1992). Popular groundwater transport modeling codes such as MT3D (Zheng and Wang, 1999; Bedekar et al. 2016) include convective as well as mass conservative schemes for solving the transport equations to provide options most appropriate to the simulation objectives.

Transport simulations are based on the premise that the flow model is balanced for each discrete cell throughout the simulation domain. However, numerical flow solutions can contain mass balance errors that could lead to severe consequences in the transport solution such as unrealistic buildup of solute mass and associated concentrations in a cell with excess inflow. In practical applications, these errors largely go unnoticed since complex groundwater solute distributions and other processes (storage, dispersion, adsorption, decay or simulation time scales) may mask the numerical impacts.

Ideally, these flow errors should be reduced by using tighter convergence tolerances for the flow solution. However, that may not be possible or practicable throughout the domain of large simulations with hundreds of thousands of cells. A recent publication (Svyatskiy and Lipnikov, 2017) discusses the issue of flow balance errors on the transport solution in variably saturated

porous media. Their approach adjusted the saturation term to account for non-convergence of the nonlinear flow equations such that flow and storage compensate for the error. The methodology presented here, instead, is to trap these flow balance errors and include them as a storage-like term in the computation of advective solute transport such that they do not cause non-physical (often unnoticed) errors in solute concentration computations. The associated error in solute mass resulting from errors in the flow solution is also computed at the cell level in this approach, thus allowing further investigation of the error as compared to solute mass movement due to the simulated physical transport processes. Example problems including 1-D and 2-D flow help to understand the concepts and demonstrate the impacts.

### 3.2 Advection Term of the Transport Equation

Mass balance for water flow dictates that flow into a cell plus sources within that cell equals flow out of the cell plus the change in storage. However, this may not be achieved to a sufficient degree at all cells in a simulation domain if the flow equation convergence was not adequate, causing localized mass balance errors. This error in the flow solution can be written as:

$$e = I - O - S + Q_{in} \tag{3.1}$$

where $e$ is the error in any cell of the simulation, $I$ is the rate of inflow from neighboring model cells, $O$ is the rate of outflow to neighboring model cells, $S$ is the storage change calculated as change in volume over time ($\Delta V/ \Delta t$), and $Q_{in}$ is a source term (with a negative sign for sinks). All terms in equation 3.1 have dimensions of $L^3/T$. When the error, $e$, is zero, the flow equation is perfectly balanced; neglecting storage and sources/sinks for the moment, inflow then equals outflow. In this case, even if the cell were to be fully dry (just passing the water through the cell), the concentration within the cell will be that of the inflowing water, which then flows

out at the same concentration. However, if inflow is in excess of outflow, for example, then water containing solutes would enter the domain in larger quantities than would flow out, causing concentrations within the cell to erroneously increase. The error is present even when solute storage and source/sinks are included in a model though it may be muted and not apparent in the results.

The advection of solute into a numerically discretized cell may be expressed simply (for the sake of clarity) using an upstream weighted formulation whereby the concentration of the upstream node is transmitted into the cell. For an implicit upstream weighted scheme, the advective flux of solute from a cell to an adjacent cell is computed by inserting the inflow value of a cell into the discretized coefficient matrix at the upstream location. Thus, all outflow from a cell is summed into the diagonal term (the cell itself is upstream for outflow faces) while all inflows into the cell are applied to the appropriate off-diagonal location of the row representing the cell. Sources of water are multiplied by the source concentration and applied on the right-hand-side matrix, while sinks of water are added to the diagonal term to allow for solutes to move out of the domain due to advection. Storage of water and associated solutes will add terms to both the diagonal of the coefficient matrix as well as the right-hand-side vector for transient flow solutions. Thus, the advective flux matrix is diagonally dominant if there is no balance error in the flow computations.

The suggested methodology is to acknowledge existence of the error, remove the flow imbalance amount from the transport solution, and quantify the impact of that error on transport mass balance. For an implicit, upstream weighted scheme, the flow errors can be removed from the transport solution by evaluating the term "*e"* of equation 3.1 and adding that amount to the diagonal of the transport matrix. Effectively, a positive flow error is dissipated as a sink and a

negative flow error is balanced by smaller outflow amounts thus solving the solute transport equations with a mass conserved representation of flow thus providing a stable concentration solution. The resulting transport solution error is obtained by multiplying the resulting concentration field by the flow error (the term "*e"*) at each cell location. In this manner, the error can then be examined in comparison to actual mass migration due to the solute transport processes at all numerical cells or in the global mass balance terms.

The methodology suggested here is applicable to other spatial discretization schemes (mid-point weighting or mass conserved Total Variation Diminishing schemes) and temporal discretization approaches (explicit, Crank-Nicholson, or other higher-order schemes). The upstream-weighted, implicit formulation was discussed above as a convenient demonstration of the approach. Also, inflows are not adjusted in the proposed solution because the outflows can be balanced in a lump-sum manner through the matrix diagonal term while inflows may need individual apportioning which adds subjectivity and complexity.

The methodology has been implemented into an implicit fully-upstream weighted finite-difference transport simulator that runs within the groundwater flow model, MODFLOW (Harbaugh, 2005). During back-calculation of fluid flows and storages after solving the flow equation, the flow error at each cell was also computed in MODFLOW. After the advection matrix associated with transport was filled during the solute transport routines, the error amount was added to the diagonal term of the matrix to account for local flow imbalances. After solution of the transport equation, the associated solute mass error was back-calculated for each cell and reported on a cell-by-cell basis in addition to the total model-wide mass balance output.

## 3.3 Example Problems

Two example problems are provided to demonstrate behavior of an advective transport solution subject to errors in the flow-field. The first example is a synthetic simulation where the flow-field was deliberately tweaked to create a controlled error, to facilitate examination of the behavior of the transport solution with and without correcting for the flow balance error. The second example is a 2-D model demonstrating the impact of flow imbalance due to insufficient closure tolerance of the flow solution. Results of the advective transport with and without correcting for the error are presented.

### 3.3.1 1-D Example Problem Demonstrating Impact of Unbalanced Flow-Field

A simple 1-dimensional (1-D) example problem is presented to demonstrate the concepts that are discussed (Figure 3.1). The domain is discretized into 2 layers, 2 rows and 100 columns with a cell spacing of $\Delta x = 10$ m, $\Delta y = 10$ m, and $\Delta z = 5$ m. A hydraulic head gradient of 1 m/m is applied, dropping by 10 meters (m) between adjacent cells with a horizontal flow of 500 cubic meters per day (cmd). For a transport porosity of 1, the flow velocity is 10 m/d. Therefore, use of a time-step size of 1 day for the transport simulation gives a Courant number of 1. The transport simulation was run for 300 1-day time-steps for a total simulation time of 300 days. The transport setup is such that the initial concentration in the domain is 1, and the inflow concentration of water at the left edge is also 1. Thus, the transport solution is trivial and should be equal to 1 throughout the domain at all time steps.

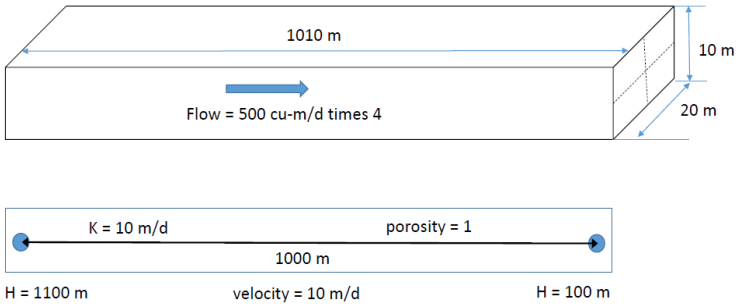


Figure 3.1 – 1-D Flow and Transport Example Problem Setup and Details. (Reproduced from Panday, Bedekar, Langevin, 2017a).

The initial transport solution for this setup gave a concentration of 1, as expected, for all time-steps; this is simulation number 1 in Table 3.1 which lists the simulations performed for this example problem. Next, the flow field was perturbed to cause a local flow imbalance by changing the head internally within MODFLOW, in column 51 for all rows and layers by an equal amount before the flow budgets were computed. For the balanced flow field, the head values at columns 50, 51 and 52 were 610, 600 and 590 respectively, giving a flow of 500 cmd inflow from column 50 to column 51, and a 500 cmd outflow from column 51 to column 52. When the head at column 51 was manually reduced by 2 m, the flow becomes imbalanced with an inflow from column 50 of 600 cmd and an outflow to column 52 of 400 cmd. Note that there is also a flow imbalance in cells 50 and 52 because the corresponding inflows and outflows from column 49 and to column 53 are 500 cmd. Table 3.1 shows the relationship between the head change and flow imbalance for this example. Solute transport was then simulated with this imbalanced flow field to note the impact without any corrections applied to acknowledge this flow imbalance. Figure 3.2 shows the effect of the flow imbalance on the horizontal concentration profile in the domain, for the second and third simulations in Table 3.1 where the head at cell 51 was perturbed by -2 and +2 m, respectively. The plot is for steady-state transport conditions, which was achieved at roughly 100 days of the 300-day simulation period. It is noted

that an oscillation occurs at columns 49 and 50 (at distances of 490 and 500 m respectively). The oscillation is opposite when head was raised, compared to when head was lowered. Figure 3.3 shows the effect of a larger flow imbalance with a head change of +8 m. The oscillation is noted to be larger for this case than in Figure 3.2. Also, the oscillation at columns 49 and 50 grew through time and was propagated in the downstream direction for earlier times before stabilizing. Figure 3.4 shows the effect of an even larger flow imbalance with a head change of +11 m. Note that for this case, the head in the cells at column 51 is larger than for the adjacent columns 50 and 52 and therefore there is only outflow from column 51. Steady-state conditions were not achieved for this case, and concentrations at column 50 grew throughout the simulation.

Table 3.1 – Head Change and Flux Imbalances for Numerical Cell 51 in Example 1

| Run No. | Head Change | Head | Inflow from column 50 | Outflow to column 52 |
|---|---|---|---|---|
| 1 | 0 | 610 | 500 | 500 |
| 2 | -2 | 608 | 600 | 400 |
| 3 | 2 | 612 | 400 | 600 |
| 4 | 8 | 618 | 100 | 900 |
| 5 | 11 | 621 | -50 | 1050 |

The simulation cases for this example problem are extreme but clearly demonstrate the impact of various flow imbalances. Similar flow imbalance conditions can occur locally in complex site simulations and their impacts often go unnoticed unless concentrations reach extreme values that are obvious to the modeler or cause the simulation to fail.

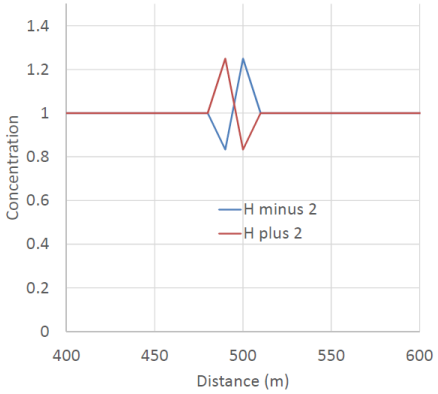


Figure 3.2 – Concentration Profile for Run Numbers 2 and 3 of Table 3.1. (Reproduced from Panday, Bedekar, Langevin, 2017a).

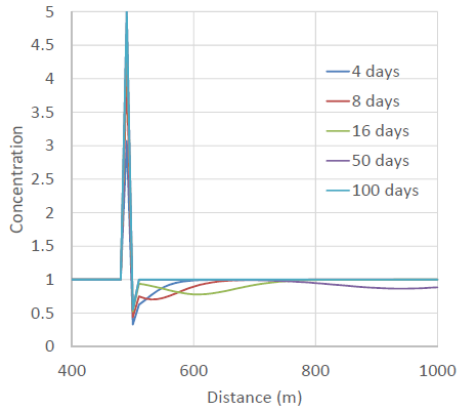


Figure 3.3 – Concentration Profile for Run Numbers 4 of Table 3.1. (Reproduced from Panday, Bedekar, Langevin, 2017a).

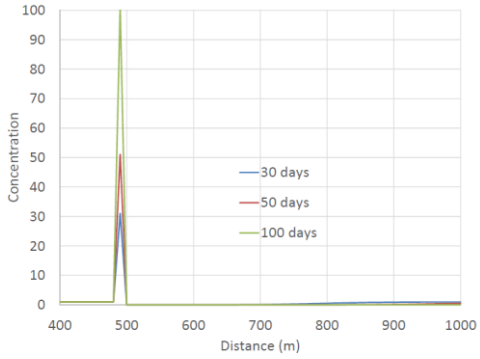


Figure 3.4 – Concentration Profile for Run Numbers 5 of Table 3.1. (Reproduced from Panday, Bedekar, Langevin, 2017a).

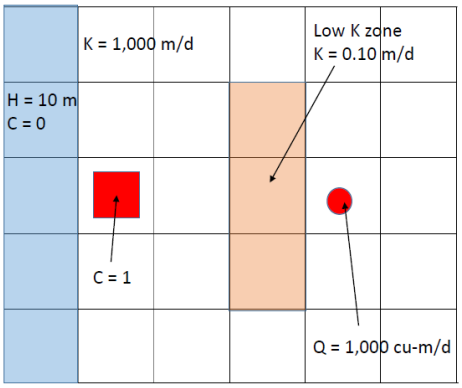


Figure 3.5 – 2-D Flow and Transport Example Problem Setup and Details. (Reproduced from Panday, Bedekar, Langevin, 2017a).

When the above correction discussed in this paper was applied, there was no oscillation in any of the simulations, and the concentrations remained at 1 throughout the domain, for the duration of the simulations. There were, however, localized mass balance errors associated with the transport solution, which did not show up in the global mass balance summary because they cancel each other. This can also occur in complex situations further masking the errors.

### 3.3.2 Example 2 – 2D Steady-State Flow and Transport with Heterogeneity

A simple 2-dimensional example problem is provided here to demonstrate the kind of errors that can be generated in simulating advective transport, due to imbalance in the flow solution. Figure 3.5 shows the problem setup. The domain consists of 1 layer, 5 rows and 6 columns of cells with x- and y-spacing of 10 m and a hydraulic conductivity of 1,000 m/day and includes a low conductivity obstruction of 0.1 m/day where the bottom elevation is raised by 10 feet. A constant head boundary is prescribed along the left edge, and an extraction well pumps at 1,000 cmd behind the obstruction. The concentration at the prescribed head boundary is zero, and a specified concentration equal to 1 is placed in front of the low conductivity obstruction. The simulation was run with a head tolerance of 0.001 m for a flow solution without mass balance errors, and of 0.1 m for a solution that included flow imbalance conditions.

Figure 3.6 shows the simulated concentration distribution under steady-state conditions for the solution without mass balance errors, Figure 3.7 shows the simulated concentration distribution for the solution with flow imbalance, and Figure 3.8 shows the error in the transport solution that results from flow imbalance (difference between the two solutions). The solution with flow imbalance was obviously in error; the symmetry of the problem was not maintained, and simulated concentrations were larger than the maximum prescribed concentration of unity with errors as large as 15% of the maximum concentration. However, with the correction applied, the concentrations however look similar to those of Figure 3.6 without the oscillation. Also, the impact was isolated and quantified as shown in Figures 3.9 and 3.10. Figure 3.9 shows the cell-by-cell flow balance error for the solution with loose flow convergence, and Figure 3.10 shows the associated error in solute mass. Understanding the distribution of errors in a domain is useful in deciding the quality of a simulation with regards to the simulation objectives. Also, these localized errors did not translate to global mass balance errors for flow or transport that were noted in the output listing file.

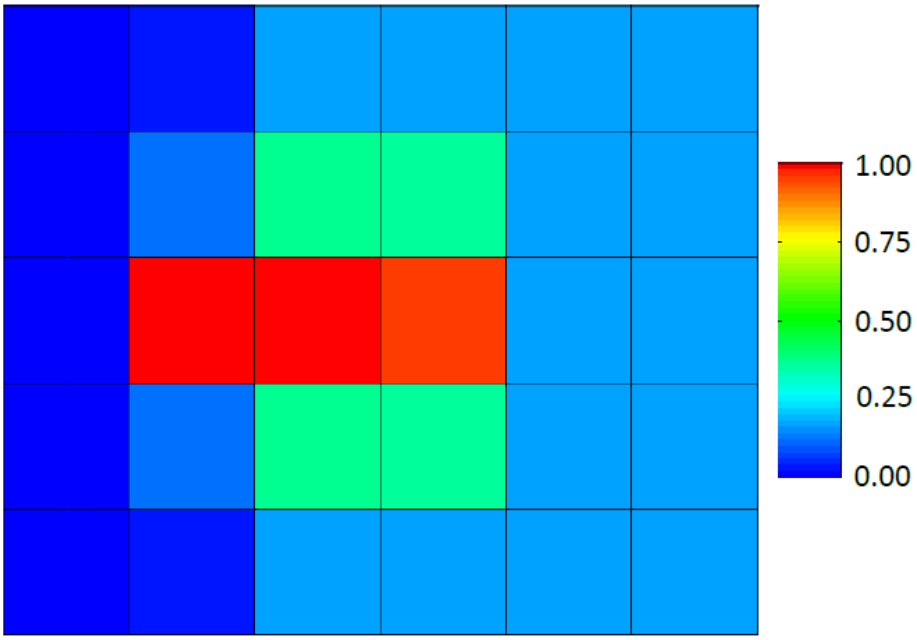


Figure 3.6 – Simulated Concentration Distribution of Converged Solution. (Reproduced from Panday, Bedekar, Langevin, 2017a).

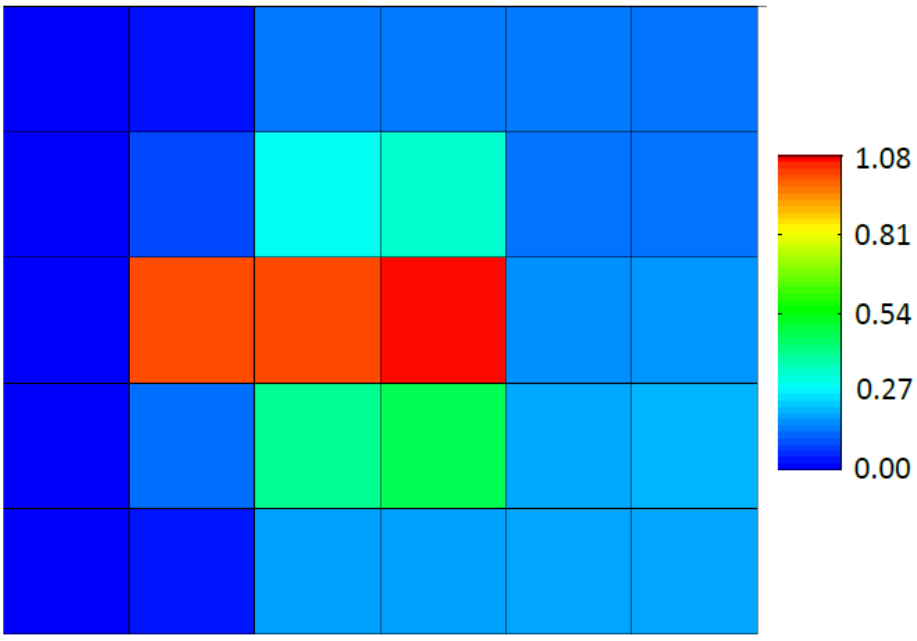


Figure 3.7 – Simulated Concentration Distribution of Solution with Flow Imbalance. (Reproduced from Panday, Bedekar, Langevin, 2017a).

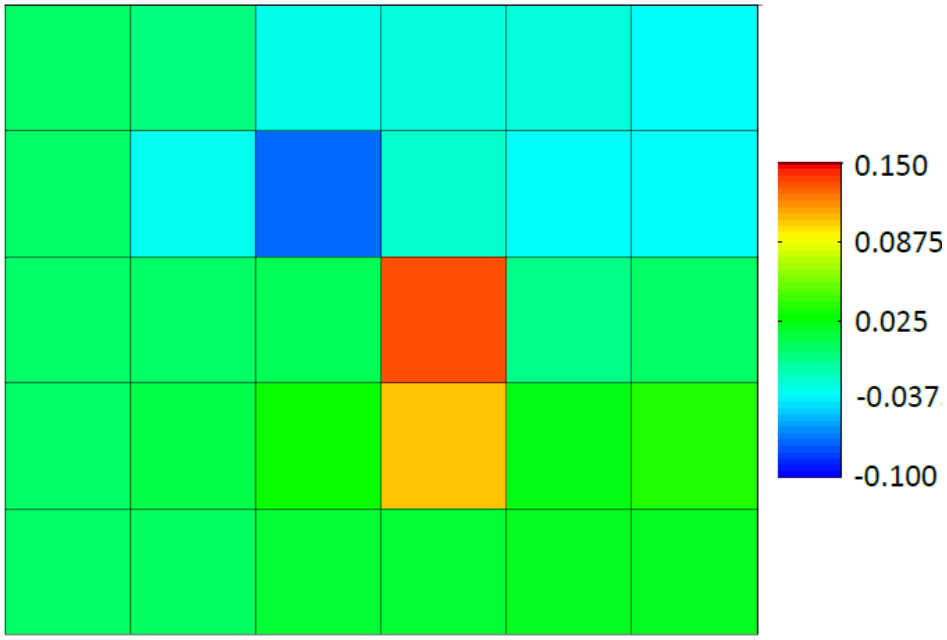


Figure 3.8 – Error in Concentrations due to Flow Imbalance. (Reproduced from Panday, Bedekar, Langevin, 2017a).

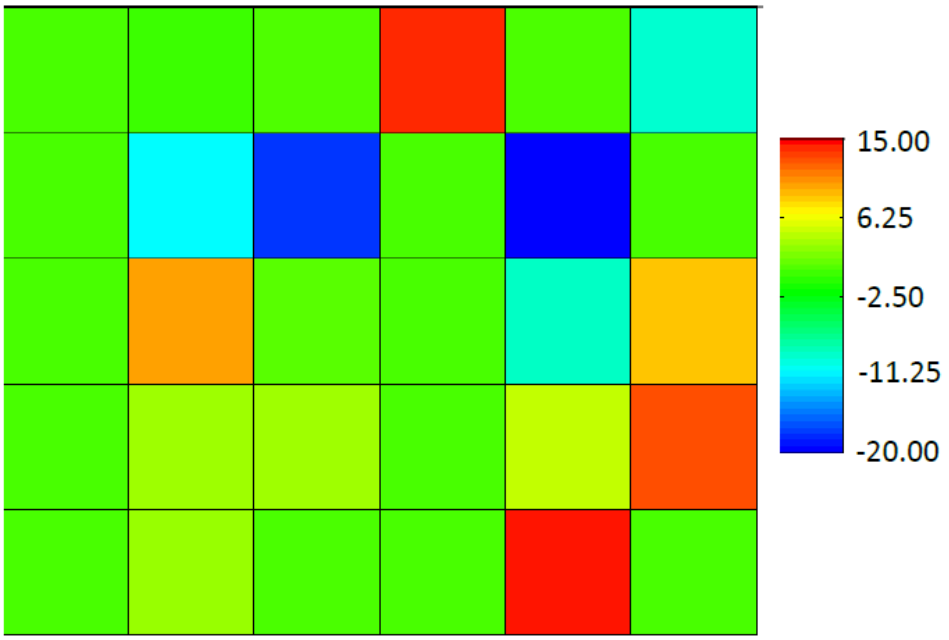


Figure 3.9 – Flow Balance Error for Solution with Flow Imbalance. (Reproduced from Panday, Bedekar, Langevin, 2017a).

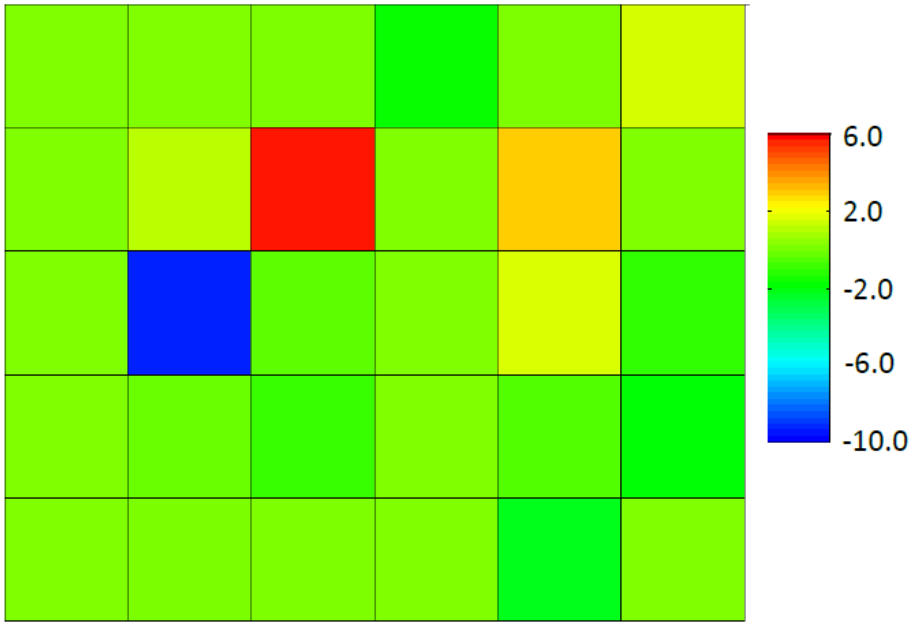


Figure 3.10 – Transport Mass Balance Error for Solution with Flow Imbalance. (Reproduced from Panday, Bedekar, Langevin, 2017a).

## 3.4 Summary

Errors in the flow-field used by a mass conserved solute transport formulation can translate into errors in solute concentration. A methodology is presented to capture and quantify these errors. Although the examples presented were largely exaggerated, they demonstrate the issue. Experience has shown that similar circumstances are often created in complex real-world modeling problems with large heterogeneities and complex stratigraphy. The correction to the solute transport formulation proposed here provides a practical solution enabling stable concentration solutions and isolating associated mass errors.

# Chapter 4 – Benchmarking Axisymmetric Modeling Methods in MODFLOW-USG

Axisymmetric groundwater models are used for simulating radially symmetric conditions. Groundwater simulators built specifically to model axisymmetric conditions are most commonly used for simulating aquifer tests. Although some numerical models capable of simulating flow and solute transport that are developed in the cartesian coordinate system framework offer flexibility to simulate axisymmetric conditions, most of the numerical groundwater models, such as the MODFLOW family of codes, are based on structured grids in which axisymmetric flows cannot be directly simulated. Researchers in the past have provided methods to manipulate aquifer properties to mimic axisymmetric conditions. This study presents a methodology that takes advantage of the unstructured grids of MODFLOW-USG to simulate axisymmetric models within the MODFLOW framework. To develop axisymmetric models, the intercell interface area arrays of MODFLOW-USG were calculated to accurately represent coaxial cylindrical model cells. Three examples are presented to demonstrate the application of MODFLOW-USG for axisymmetric modeling: a pumping well with delayed yield effects, a vadose zone flow model simulating an infiltration basin, and a density-dependent saltwater intrusion problem for a circular island. Results were verified against analytical solutions and published numerical codes.

## 4.1 Background

Groundwater models simulating cylindrical flow domains that are symmetric around the axis of the modeled domain are referred by several names including axisymmetric (axially symmetric) models, radial flow models, cylindrical models, R-Z models, or R-Theta models. Groundwater flow equations for axisymmetric models are written using cylindrical polar coordinates (r, $\theta$, z) and are solved for radial flow within a cylindrical domain.

Axisymmetric models are suitable for idealized situations in which the impact of stresses on the groundwater system is radially symmetric. Analytical models for aquifer flow like the Theis solution are classic examples of radial flow systems. Some numerical models are developed to exclusively simulate axisymmetric flow in a pumping well. Mansour et al (2007) present an axisymmetric finite-difference flow model capable of solving heterogenous aquifer under confined or unconfined conditions designed to simulate pumping tests.

Fully three-dimensional models can be developed to solve radially symmetric problems, but axisymmetric models offer an advantage in efficiency and accuracy as fully three-dimensional models are sometimes impractical to simulate if near-well and far-well processes are to be evaluated. In fully three-dimensional models grid refinement can lead to a large number of model cells, which in turn can substantially increase the simulation run time. Axisymmetric models essentially reduce a three-dimensional problem to two-dimensions resulting in fewer model cells and hence, improve efficiency. In contrast with three-dimensional models, depending on the need for accuracy, high degree of grid refinement in the radial and vertical direction can be afforded in axisymmetric models reducing discretization issues associated with three-dimensional numerical models.

Idealized conditions of axisymmetric models, however, are rarely encountered in the field scale applications of groundwater models. Therefore, most of the groundwater flow and transport simulators are based on the cartesian coordinate system to enable the development of three-dimensional models. Some groundwater models offer an option to simulate groundwater flow conditions in an “axisymmetric mode”. Examples of such numerical modeling codes include the proprietary codes MODFLOW-SURFACT (HydroGeoLogic, 1998; Panday and Huyakorn, 2008) and FEFLOW (Diersch, 2002).

One of the most widely used groundwater flow codes is MODFLOW and its derivatives commonly called the MODFLOW family of codes. Most MODFLOW and related codes that are available in the public domain cannot model axisymmetric problems. Researchers have proposed various ways to circumvent the lack of axisymmetric modeling option in MODFLOW. Reilly and Harbaugh (1993) created a program called RADMOD, a preprocessor to create MODFLOW input files. RADMOD creates MODFLOW input files by manipulating cell-to-cell conductance values. That approach, however, makes the application of RADMOD limited to confined aquifers due to a-priori conductance calculations. The generalized finite-difference package used by RADMOD was supported in the early versions of MODFLOW but was not supported by MODFLOW-2000 and later versions. Samani et al (2004) developed relationships between cylindrical coordinate system and cartesian coordinate system and a scaling methodology to convert between the two systems. The conversion was referred to as the log scaling method (LSM) and LSM was incorporated into MODFLOW-2000 source code to be able to simulate axisymmetric models. Langevin (2008) proposed a methodology to adapt MODFLOW to axisymmetric modeling without the need to modify the source code of MODFLOW. Langevin (2008) presented a strategy to modify input parameters, in particular, horizontal and vertical hydraulic conductivity, specific storage, and porosity. The parameter manipulation methodology acts as a surrogate to represent increased flow area in model cells with increased radial distance. Logarithmic weighting of interblock transmissivity (option available in MODFLOW) was used and Langevin (2008) showed the importance of logarithmic weighting against harmonic weighting for simulating axisymmetric models. Both confined and unconfined flow could be simulated with this approach. With the approach proposed by Langevin (2008) lateral heterogeneity could not be represented in the model, only layered heterogeneity could be

represented; this is not, however, a serious limitation because lateral heterogeneity in an axisymmetric model would represent circular bands of heterogeneity that is typically not evaluated. Louwyck et al (2014) presented an approach very similar to Langevin (2008), and additionally, had the capability to incorporate radial heterogeneity in the axisymmetric model. This was achieved by manipulating aquifer parameters values and setting width and length for all model cells equal to unity and using harmonic mean.

The current study presents another methodology to simulate axisymmetric models by taking advantage of unstructured grids of MODFLOW-USG (Panday et al, 2017; Panday, 2017). Unstructured grids offer the flexibility of designing model grid cells of any shape. Taking advantage of the grid flexibility, MODFLOW-USG models can be fed appropriate intercell area values for a cross sectional model to simulate axisymmetric conditions as detailed in the next section. Three examples are then presented to verify and demonstrate the applicability of MODFLOW-USG for simulating axisymmetric conditions, including: (1) a pumping well; (2) vadose zone flow; and (3) saltwater intrusion on a circular island. The latest version in the MODFLOW family of codes, MODFLOW 6 (Langevin et al, 2017), offers unstructured grid functionality akin to MODFLOW-USG. Therefore, the methods described below can also be applied to MODFLOW 6 for developing axisymmetric models.

## 4.2 Methods

MODFLOW-USG is a finite volume unstructured grid code that does not impose any restrictions on the shape of individual model cells. The shape of individual model cells is not explicitly defined in the input files but is mathematically represented with user-defined intercell connectivities, distances and interface areas. Thus, an axisymmetric model can be conceptualized using coaxial cylindrical model cells. A schematic of such a model grid is shown in Figure 4.1.

The associated grid cells can be represented as cylinders (at the axis of rotation) and donuts (or rings) within the unstructured discretization framework of MODFLOW-USG, implemented in the unstructured discretization (DISU) input file, also known as the DISU package of MODFLOW-USG. As noted in Figure 4.1, this grid is generated as a cross-section containing several columns or layers of cells which are rotated about the vertical z-axis.

Radial discretization was assumed the same in all model layers, i.e., model cells were assumed to be stacked across all layers. MODFLOW-USG imposes no restrictions on the stacking of model cells, however, model cells were stacked in the examples presented below for simplicity. The total number of model cells (NODES) in the axisymmetric models was calculated as the number of model cells in the radial direction in each layer (NCOL) multiplied by the number of model layers (NLAY). The radial distance between model cells ($\Delta r$) may vary or held constant depending on the modeling requirements, though typically a finer discretization is applied nearer to the vertical z-axis for better resolution about the point of interest. Similarly, the vertical distance between model cells ($\Delta z$) can potentially vary, but a uniform thickness was used for all layers in the examples presented below.

Coaxial cylindrical cells were defined by means of two area input arrays in the model, the AREA and the FAHL arrays as required by the DISU package of MODFLOW-USG. The AREA array contains the horizontal area of model cells and the FAHL array contains the area of the interface between two connected cells. Note that the AREA array entry for a cell is the same as its vertical connection area entry within the FAHL array. The AREA input was calculated as the horizontal area of a model cell. The horizontal area for the model cell representing column j, can be calculated as shown in equation 4.1.

$$AREA_j = \pi\left(r_j^2 - r_{j-1}^2\right) \quad (4.1)$$

where, $r_j$ and $r_{j-1}$ are the distances of the outer cell boundaries of columns j and j-1, respectively, as shown in Figure 4.1. Equation 4.1 essentially calculates the area of concentric rings by subtracting the area of the concentric circle formed by the inner edge of a model cell in column j, from the area of the concentric circle formed by the outer edge of a model cell in column j.

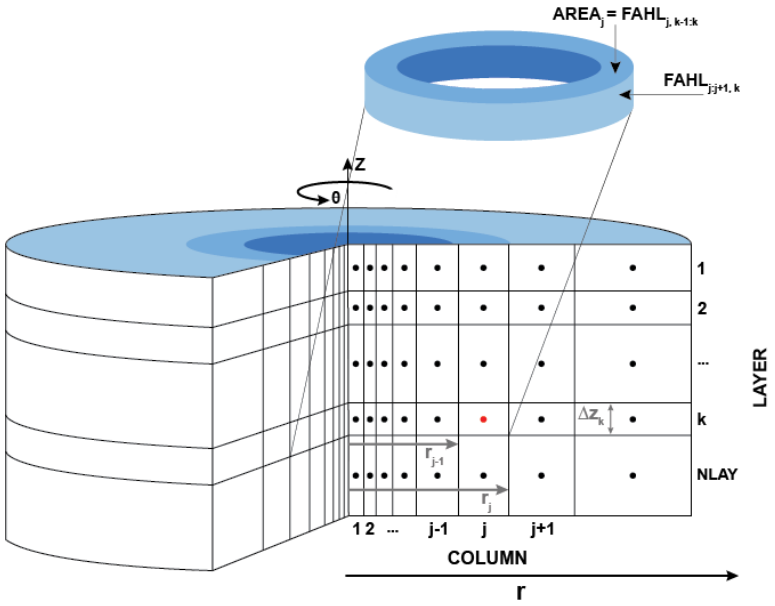


Figure 4.1 – Schematic showing conceptual grid design for an axisymmetric model using MODFLOW-USG. Refer to equations 4.1 to 4.3 for an explanation of terms AREA, FAHL, rj-I, rj, and $\Delta z_k$.

Two area calculations were needed to represent cell interface areas in the FAHL array of the DISU package: (1) cell interface area calculated in the radial direction as shown in equation 4.2; and (2) cell interface area in the vertical direction as shown in equation 4.3. Note that the calculation in equation 4.3 is the same as equation 4.1 as both the calculations essentially represent horizontal area of a model cell.

$$FAHL_{j:j+1,k} = 2\,\pi\, r_j \Delta z_k \quad (4.2)$$

$$FAHL_{j,k-1:k} = \pi\left(r_j^2 - r_{j-1}^2\right) \quad (4.3)$$

where, $\Delta z_k$ is the model cell spacing in the vertical direction. The calculations detailed above for the AREA and FAHL arrays of MODFLOW-USG's DISU package are the only calculations needed to create axisymmetric models with MODFLOW-USG. A pre-processing program was developed to write the DISU file of MODFLOW-USG by reading user-defined NLAY, NCOL, and horizontal and vertical cell spacing. Detailed input instructions for the DISU file and other input files are available in the documentation of MODFLOW-USG.

With this methodology of creating axisymmetric models, the simulator MODFLOW-USG can be used as-is, i.e., no code modifications are needed to the program. A priori calculations of model parameters are also not needed. In fact, once the model domain is appropriately discretized using the methodology discussed above, heterogeneity may be introduced and changed as needed without the need to recalculate any surrogate parameters needed by other methodologies proposed in the past.

The methodology presented here can be extended to make more complex radial sections (pie shaped grids) in a model, as the model requirements may be, by manipulating the area calculations and defining intercell connections appropriately. This study, however, only discusses the application of MODFLOW-USG to create axisymmetric models.

## 4.3 Example Problems

### 4.3.1 Pumping Well

A pumping well was simulated in an unconfined aquifer system with delayed yield response as the first example. An analytical solution provided by Neuman (1974) forms the basis of this simulation. MODFLOW-USG was used to create an axisymmetric model to simulate the

drawdown caused by a pumping well. Results of the MODFLOW-USG axisymmetric model were compared to the analytical solution provided by Neuman (1974). The analytical solution was solved using the software AQTESOLV. A fully three-dimensional model was also developed using MODFLOW-USG and drawdown results from the three-dimensional model were compared to the axisymmetric model to assess the impact of representing a three-dimensional numerical discretization with a radially symmetric discretization.

The example simulated a partially penetrating pumping well with a pumping rate of 113.27 $m^3$/day (4,000 $ft^3$/day) in an unconfined aquifer. The aquifer was assumed homogeneous and isotropic. The initial saturated thickness was set to 15.24 m (50 ft) with a hydraulic conductivity of 6.096 m/day (20 ft/day), specific yield of 0.1, and specific storage of $3.281 \times 10^{-5}$ $m^{-1}$ ($10^{-5}$ $ft^{-1}$). The pumping well was assumed to be screened within the bottom 3.048 m (10 ft) of the 15.24 m (50 ft) thick unconfined aquifer.

The axisymmetric numerical model was discretized vertically into 25 layers (NLAY = 25) with each layer 0.6096 m (2 ft) thick. Horizontal discretization varied from 0.0762 m to 152.4 m (0.25 to 500 ft), with the smallest grid spacing assigned near the pumping well and increased grid spacing assigned away from the well. The axisymmetric model was discretized into 22 model cells in the radial direction (NCOL = 22) in each model layer with the total radial distance from the pumping well equal to 609.6 m (2,000 ft). A prescribed flux boundary representing the pumping well was imposed on the vertical set of model cell representing the center of the radially symmetric model. Well boundary was imposed on model layers 21 through 25 representing the bottom 3.048 m (10 ft) of the aquifer. No-flow boundary was assumed on the lateral, top, and bottom boundaries.

For the fully three-dimensional numerical model, vertical and horizontal grid spacing was set the same as the axisymmetric model. The three-dimensional model was discretized into 25 layers, 43 rows, and 43 columns, with the total model domain extent of 1219.2 m (4,000 ft) in both the x- and y-directions and 15.24 m (50 ft) in the vertical z-direction. Well boundary was implemented at the center of the model domain, i.e., row number 22 and column number 22. Akin to the axisymmetric model, well boundary was imposed from model layers 6 through 20.

Transient drawdown was recorded at the top, middle, and bottom of the 15.24 m thick aquifer at a distance of 12.192 m (40 ft) from the pumping well. Dimensionless drawdown, $s_D$ and dimensionless time, $t_y$ were calculated as shown in equations 4.4 and 4.5 (Neuman, 1974):

$$s_D = \frac{4\pi T s}{Q} \tag{4.4}$$

$$t_y = \frac{Tt}{S_y r^2} \tag{4.5}$$

where, T is the transmissivity of the aquifer [$L^2$/T]; s is the drawdown [L]; Q is the pumping rate [$L^3$/T]; t is the elapsed time [T]; $S_y$ is the specific yield [-]; and r is the radial distance [L].

Results obtained from the MODFLOW-USG axisymmetric model were compared to the analytical solution and the MODFLOW-USG three-dimensional model as shown in Figure 4.2. As seen in Figure 4.2, drawdown results show good agreement between the axisymmetric numerical model, and the analytical and three-dimensional models. Excellent agreement between the model results in all cases signifies that axisymmetric models can be appropriately simulated using MODFLOW-USG with the approach presented here.

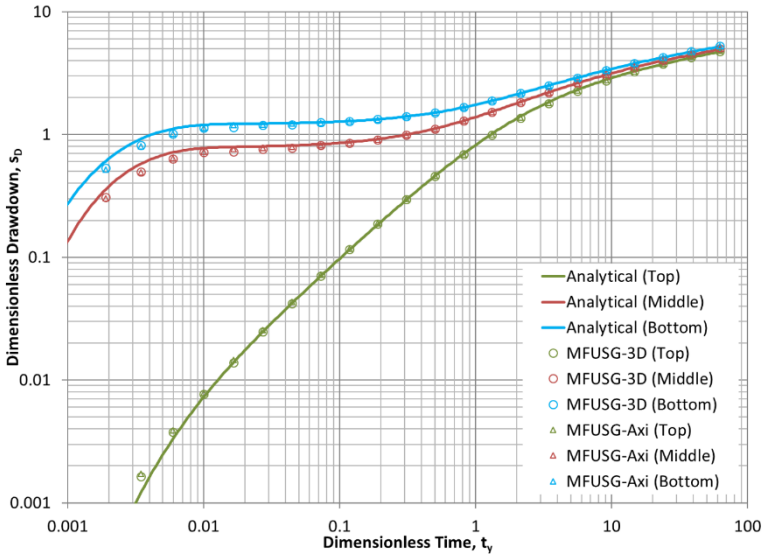


Figure 4.2 – Drawdown for a pumping test comparing MODFLOW-USG axisymmetric model (MFUSG-Axi) results shown as triangles with analytical solution shown as lines and MODFLOW-USG three-dimensional model (MFUSG-3D) results shown as circles.

### 4.3.2 Vadose Zone Flow

The second example simulates the saturation profile underneath an infiltration basin as a result of water seeping through a thick vadose zone. The vadose zone considered in this example is a sandy aquifer with a lower conductivity confining unit in the middle. A circular infiltration basin is considered that infiltrates water at a rate that is higher than the vertical conductivity of the confining unit. This condition creates a subsurface mound on top of the confining unit underneath the infiltration basin. The mound of water spreads horizontally over the confining unit until the point that the infiltration rate at the extreme edge of the mound is as small as the conductivity of the confining unit. The formation of a subsurface mound and the study of the extent of its spread presents an ideal scenario for an axisymmetric model. The system was simulated with two models, both using MODFLOW-USG, as documented in Panday (2017), an extension of the initial release of MODFLOW-USG that enables vadose zone simulations. The first model was an axisymmetric model, and the second model was a three-dimensional model explicitly representing a circular shaped infiltration basin.

The total vadose zone thickness was assumed 27 m and the confining unit was assumed 0.5 m thick at a depth of 13 m. For both models, the aquifer was vertically discretized into 54 layers with a uniform thickness of 0.5 m. 51 radial coaxial model cells were simulated in each model layer with horizontal spacing varying from 0.5 m to 200 m in the radial direction. Grid discretization from the axisymmetric model was mirrored to create the three-dimensional model with 102 rows and 102 columns with the infiltration basin at the center of the model domain. The radius of the circular infiltration basin was assumed to be 20 m. The infiltration basin was represented by the first 40 radial model cells representing the center of the axisymmetric model domain and by a circular footprint of 5,008 cells for the three-dimensional model. An infiltration rate of 0.31 m/day was used for the infiltration basin and zero recharge was assumed outside of the basin footprint. Table 4.1 shows all the vadose zone parameters used in the model. The bottom model layer was assigned a prescribed head boundary of zero representing the water table layer. Vertical lateral model cells were assigned no-flow boundary.

The axisymmetric and the three-dimensional models described above were simulated using the version of MODFLOW-USG documented in Panday (2017). Steady-state saturation profiles comparing the two models is shown in Figure 4.3. It is clear that results from the two models are in close agreement. As seen in Figure 4.3, the confining layer restricts the flow from the infiltration basin creating a mound over the confining unit underneath the basin. As a result of the mounding, water spreads over a larger area beyond the infiltration boundary. This model structure was used during the design of a real-world infiltration basin to assess the spatial extent of the impact of infiltration basin and to evaluate the infiltration capacity of the basin to limit the mounding below land surface. The three-dimensional example was prepared for a single

simulation to demonstrate applicability of an axisymmetric model, while the axisymmetric model was used in the project.

Table 4.1 – Parameters used for vadose zone models

| Parameter | Aquifer | Confining Layer |
|---|---|---|
| Horizontal hydraulic conductivity | 35.25 m/day | 0.008 m/day |
| Vertical hydraulic conductivity | 3.525 m/day | 0.008 m/day |
| Specific storage | $1.0 \times 10^{-4}$ $m^{-1}$ | |
| Specific yield | 0.27 | |
| van Genuchten α | 8.3 $m^{-1}$ | |
| van Genuchten β | 1.35 | |
| Brooks Corey parameter, n | 8.8 | |
| Residual saturation | 0.013 | |

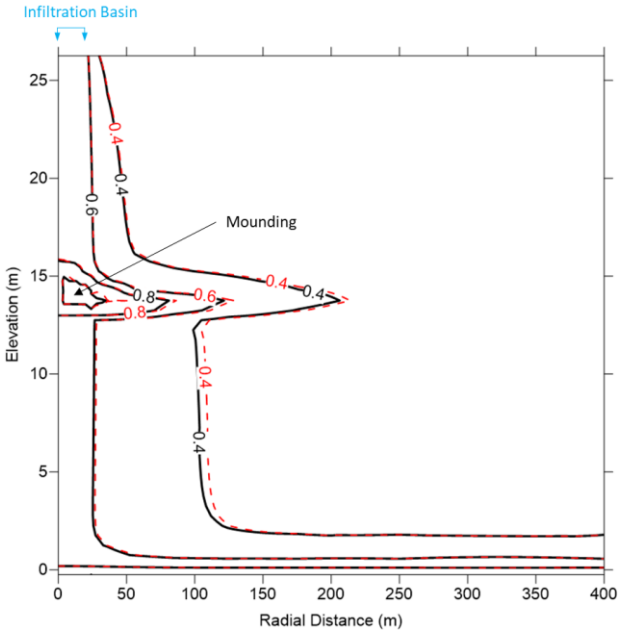


Figure 4.3 – Comparison of steady-state saturation contours for an infiltration basin simulated using an axisymmetric model (black solid lines) and a three-dimensional model (red dashed lines). Both models were simulated using MODFLOW-USG documented in Panday (2017) that enables vadose zone simulations. A 0.5 ft thick confining unit was simulated within the vadose zone at an elevation of 13.5 m resulting in subsurface mounding underneath the infiltration basin within the vadose zone resulting in perched conditions farther away from the infiltration basin boundary.

### 4.3.3 Saltwater Intrusion

Saltwater intrusion on a circular island is presented as the third example. An axisymmetric model was developed using MODFLOW-USG to simulate the radially symmetric flow conditions on a circular island surrounded by seawater on all sides with recharge applied on top. Results from the axisymmetric model were compared to an analytical solution provided by Fetter (1972). Axisymmetric model results obtained using MODFLOW-USG were also compared to two SEAWAT models (Langevin et al, 2007): (1) a three-dimensional model spanning the entire circular island; and (2) an axisymmetric version of the SEAWAT model developed by manipulating input parameters as described by Langevin (2008). The three-dimensional SEAWAT model provided run time estimates to assess the efficiency of axisymmetric models and the axisymmetric version of SEAWAT was useful in comparing saltwater intrusion results obtained using the approach described by Langevin (2008), in which surrogate input parameters were used to mimic axisymmetric flow equations, and the approach described in this study.

An island 1 km in diameter was considered for this example with a hydraulic conductivity of 10 m/day. The island aquifer was assumed 35 m thick. A recharge boundary was applied on the island at a recharge rate of 0.635 m/year. Saltwater and freshwater densities were assumed 1,025 kg/m$^3$ and 1,000 kg/m$^3$, respectively. Saltwater total dissolved solids (TDS) concentration and freshwater TDS concentration were assumed 35 g/L and 0 g/L, respectively. Given the densities and concentrations used in the model, the rate of change of density with respect to concentration ($\partial\rho/\partial C$) was set to 0.7143. Porosity of 0.1 and longitudinal and vertical dispersivity values of $10^{-4}$ m were assumed.

The axisymmetric numerical model was developed using the BCT package of MODFLOW-USG documented in Panday (2017) with the approach discussed in the preceding

section. The model was discretized vertically into 70 layers with a uniform spacing of 0.5 m, and horizontally into 101 coaxial cylindrical model cells in the radial direction with a uniform spacing of 5 m between adjacent model cells. The horizontal extent of the axisymmetric model represents the 500 m radius of the circular island with the inner-most model cell representing the center of the island and the outer-most model cell representing the saltwater boundary. The saltwater boundary was represented as prescribed hydraulic head and prescribed concentration boundary, with values of 0 m and 35 g/L, respectively. Steady-state saltwater-freshwater interface were compared to the analytical solution presented by Fetter (1972).

A three-dimensional model was created to generate saltwater-freshwater interface for the circular island using SEAWAT. A uniform square grid representing the entire circular island was generated with 202 rows and columns with a uniform spacing of 5 m. A circular prescribed head and concentration boundary was implemented to represent seawater surrounding the circular island and the model cells that fall outside of the circular boundary were deactivated. Steady-state saltwater-freshwater interface generated by the three-dimensional model was compared with the axisymmetric model.

An axisymmetric version of the SEAWAT model was also developed using the same grid structure and dimensions as used by the MODFLOW-USG axisymmetric model. For the SEAWAT axisymmetric model, horizontal and vertical hydraulic conductivity, specific storage, specific yield, and porosity input arrays were manipulated to account for radial flow as detailed by Langevin (2008). In addition to the aquifer parameters, areal recharge was manipulated to simulate axisymmetric conditions within the three-dimensional framework of SEAWAT.

Figure 4.4 shows the saltwater-freshwater interface obtained by the MODFLOW-USG axisymmetric model and its comparison to the analytical solution and the three-dimensional as

well as axisymmetric SEAWAT models. All model results show good agreement. The plotted results for the numerical models show a concentration value of 8.75 g/L (a normalized concentration of 0.25). Note that the analytical solution assumes a sharp interface and therefore, the numerical models were run with the total variation diminishing (TVD) solution scheme. It was noted that SEAWAT uses a third-order TVD scheme which results in lesser dispersion as compared to the second-order TVD scheme used by MODFLOW-USG. A comparison of SEAWAT and MODFLOW-USG results using the upstream-weighted finite difference scheme for the transport equation gave identical results, but with even more numerical dispersion than the TVD schemes. The run times for the fully three-dimensional model was in the order of days while the run time of both the axisymmetric models was in the order of minutes, the difference could be attributed to the difference in the number of model cells.

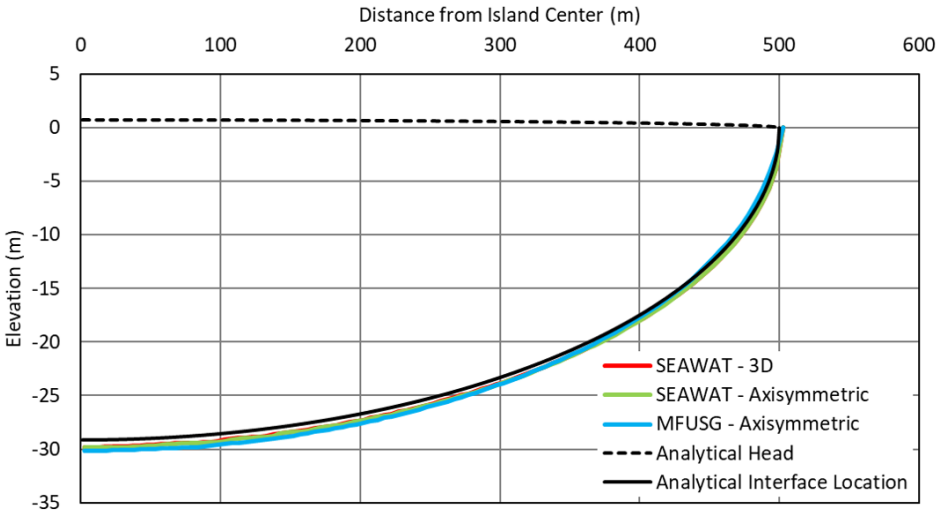


Figure 4.4 – Saltwater-freshwater interface for a circular island with recharge boundary.

## 4.4 Summary

This work presents a natural approach towards unstructured grids of MODFLOW-USG to develop axisymmetric models. The axisymmetric model development in MODFLOW-USG rests on designing the model discretization as coaxial cylindrical model cells. Thus, the framework for creating axisymmetric models is based on providing appropriate area calculations for the cylindrical model grid structure. Changing the source code or manipulating parameter values is not needed for developing axisymmetric models with MODFLOW-USG. Three examples were presented: a pumping well in an unconfined aquifer with delayed yield; infiltration pond impacts within vadose zone containing a confining layer; and, saltwater intrusion on a circular island. The examples presented here demonstrate the use and development of axisymmetric models using MODFLOW-USG for a variety of practical applications.

# Chapter 5 – Understanding the Impacts of Lake Formation on Water Resources of Low-lying Islands

Low-lying islands are vulnerable to climate change effects due to the risk of inundation as sea level rises. Islands will undergo aquifer salinization and increased water levels will expose the water table to evaporation. Interior topographic lows may form lakes exacerbating the loss of water via evaporation. Here hydrological models were utilized, based on islands in the Bahamian archipelago, to demonstrate that on islands with negative water budgets, evaporation following lake inundation can cause more than twice the loss of fresh groundwater resources relative to an equivalent amount of coastal inundation.

## 5.1 Background

Sea level rise poses poorly quantified risks to freshwater resources of nearly 50 million citizens of Small Island Developing States (SIDS) (Nurse et al., 2014). Many small islands have average elevations near sea level, particularly barrier islands (Masterson et al., 2013) and islands composed of carbonate bedrock (Vacher and Quinn, 2004). Sea level rise can shrink freshwater resources directly, through aquifer salinization and reduced groundwater catchment size following coastal inundation and, indirectly, through the dynamics of freshwater lenses (Ketabchi et al., 2014). These dynamics are governed by the Ghyben-Herzberg principle (Figure 5.1a), which states that, at equilibrium, the elevation of the water table above sea level (h) and the depth of the interface of fresh and saline groundwater (z) at the same location are related by

$$z = \left(\frac{\rho_f}{\rho_s - \rho_f}\right) h \tag{5.1}$$

and $\rho_f$ and $\rho_s$ are the densities of fresh and saline groundwater, respectively (Vacher, 1988). With typical densities of fresh and marine salt water ($\rho_f$ and $\rho_s$ = 1000 and 1025 kg/m3, respectively), the thickness of the freshwater lens is approximately 40 times the elevation of the water table above sea level (Vacher, 1988). The thickness of the freshwater lens is thus sensitive to changes in water table elevation (h) by a factor of 40 to 1. Modest reductions in water table elevation relative to sea level, such as those occurring from coastal inundation and reduced island area, can therefore result in substantial reduction in the volume of freshwater lenses (Ketabchi et al., 2014) (Figure 5.1a).

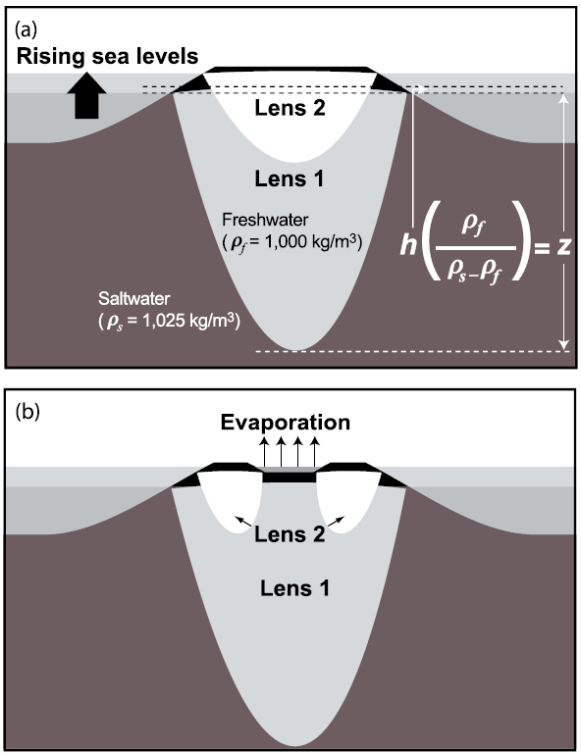


Figure 5.1 – (a) Lens-shaped bodies of fresh water exist on ocean islands due to the difference in density between fresh and saline water (e.g., equation (5.1)). Sea level rise reduces island width and lowers water table elevation relative to sea level as the cumulative resistance to groundwater flow decreases. The freshwater lens thickness decreases by a factor of 40× that of the lowering of the water table. (b) Sea level rise elevates the water table relative to the island surface which can raise the water table and flood closed inland depressions to form lakes. These lakes evaporate fresh water from their surface, may allow upconing of salt water similar to withdrawal from wells, and can segment previously continuous freshwater lenses into separate lenses. These segmented lenses have groundwater flow paths that drain toward both the coast and the lake, further lowering water table elevations and enhancing the thinning of the lens (Figures 5.2a and 5.2c). (Reproduced from Gulley et al, 2016).

Inundation by rising sea level has been widely considered to mostly threaten only low-lying coastal areas (Dasgupta et al., 2009); however, closed inland depressions with elevations below future sea levels, common to many barrier islands (Masterson et al., 2013), atolls (Ayers and Vacher, 1986; Woodroffe, 2008), and other carbonate islands (Martin and Gulley, 2010), are also prone to inundation (Figure 5.1b). Such inundation would be similar to a switch from a recharge-limited to topography-limited coastal groundwater system (Michael et al., 2013). Some depressions experience transient flooding when water tables are elevated by heavy rainfall, astronomically controlled high tides (Yamano et al., 2007; Woodroffe, 2008; Masterson et al., 2013; Rotzoll and Fletcher, 2013) and regional increases in sea level associated with intradecadal climate oscillations and shifts in oceanic currents (Sallenger et al., 2012).

Permanent flooding of depressions in response to future eustatic sea level rise has been overlooked in previous assessments of impacts to water resources (Dasgupta et al., 2009; Nurse et al., 2014). The importance of this formation is clear from shallow lakes and other surface water features that formed on carbonate islands and platforms around the world when Holocene sea level rise elevated water tables into surface depressions (Martin and Gulley, 2010; Gulley et al., 2014). These lakes expose freshwater lenses to continuous evaporation with impacts that should depend on the balance of rainfall and evaporation (Vacher and Wallis, 1992). In arid regions where evaporation can exceed annual rainfall, such as the southern Bahamian archipelago, evaporation from modern lakes has led to upconing of saline groundwater, lake, and aquifer salinization and even complete segmentation of freshwater lenses (e.g., Figure 5.1b) (Vacher and Wallis, 1992). To date, however, no studies have evaluated how freshwater lenses will respond as rising sea levels and water tables form new lakes on islands in arid regions. Consequently, we use numerical simulations in this study to explore how various lake formation

scenarios alter freshwater lens volumes on a generic strip island using aquifer and climate parameters from the Bahamian archipelago. These simulations improve understanding of how paleofreshwater lenses responded to lake formation during the Holocene and how projected sea level rise may impact modern low-lying island water resources.

The Bahamian archipelago consists of carbonate islands with similar aquifer compositions that extend 1000 km across a latitudinal water balance gradient, making it an ideal test case for understanding how lake formation may impact freshwater lenses. With positive water balances, freshwater lenses are continuous, and lakes contain freshwater (Cant and Weech, 1986). Freshwater lenses also occur on islands with negative water balances, but lakes range from brackish to hypersaline, causing authigenic mineral precipitation (calcite and halite) (Cant and Weech, 1986). These saline lakes tend to separate island freshwater lenses into separate, smaller lenses (Figure 5.1b) (Cant and Weech, 1986; Vacher and Wallis, 1992).

The persistence of freshwater lenses on islands with negative water budgets [e.g., Cant and Weech, 1986] may seem counterintuitive. Lenses are able to form in spite of the negative annual water budget because rainfall exceeds potential evaporation some months of the year [Vacher and Wallis, 1992] and because some recharge occurs along vadose fast flow routes that are dissolved in the carbonate bedrock [Jocson et al., 2002]. The persistence of freshwater lenses on modern islands with negative water budgets suggests that once recharge reaches the lens, carbonate bedrock protects it from intense evapotranspiration and the full, annual potential evapotranspiration rate is not realized. Where lakes expose water tables, however, there is no barrier to evaporative stresses and the full annual potential evaporation can be realized.

Our models presented here expand on classic studies of carbonate strip island hydrogeology [Vacher, 1988] and interactions of lakes with freshwater lenses [Wallis et al.,

1991; Vacher and Wallis, 1992] by considering how freshwater lenses change in response to lake formation expected from sea level rise.

## 5.2 Methods

All simulations assumed steady state conditions and were conducted with SEAWAT [Guo and Langevin, 2002] using hydrological properties and meteorological variables that have been employed in analytical models of Bahamian strip islands [Vacher, 1988; Vacher and Bengtsson, 1989; Wallis et al., 1991; Vacher and Wallis, 1992]. The base model of a 1000m wide strip island consists of 2m wide and 1m high cells with 500 and 200 cells in the lateral and vertical directions, respectively. Model parameters include aquifer hydraulic conductivity, porosity, and dispersivity of 50 m/day, 30%, and 1m, respectively [Vacher and Mylroie, 2002; Holding and Allen, 2015]. Fluid properties include freshwater density, seawater density, and seawater salinity concentrations of 1000 kg/m$^3$, 1025 kg/m$^3$, and 35 kg/m$^3$, respectively. We use total dissolved solids (TDS) concentrations of $\leqslant$ 0.5 kg/m$^3$ to distinguish between potable freshwater from non-potable seawater and to represent the boundary of the fresh water lens.

SEAWAT currently lacks the capability of directly simulating lakes. We thus simulate lakes as depressions by increasing the porosity to 100% and the hydraulic conductivity by a factor of 4 in a selected set of top cells of the model grid, so that the lake depths are 1m, similar to Bahamian lakes [Teeter, 1995]. This modeling approach allows water and solutes to be transported by groundwater flow into cells representing lakes, allows for approximately completely mixed conditions in the lake cells, and allows water to be discharged from lakes by evaporation. However, these conditions do not allow salinities to exceed seawater concentrations through evaporation as observed in some Bahamian lakes. The impact of hypersaline lakes is the subject of future studies.

Scenario 1 serves as a reference for all subsequent models by establishing the thickness of a freshwater lens on a 1000m wide lake-free island with an annual recharge of 20 cm/yr, although Precipitation minus Evapotranspiration (P-ET) is negative in the central Bahamian archipelago. Recharge averages 20 cm/yr as determined using Cl concentrations in rainfall as a conservative tracer of ET [Wallis et al., 1991]. To maximize intermodel comparability and because actual recharge rates are poorly constrained across the Bahamas [Whitaker and Smart, 2004], we keep land surface effective recharge the same in all models. For scenario 2, we simulate loss of potable water solely from coastal inundation by reducing the island width by 100m without forming lakes (e.g., Figure 5.1a). While the model results are applicable to any relative rise in sea level that reduces island width by an equivalent amount, for our island topography, the relative rise in sea level was 0.4 m, a threshold that is predicted to be crossed this century [DeConto and Pollard, 2016].

For scenario 3, we simulate impacts of a 100m wide lake forming in the center of the island (e.g., Figure 5.1b). Our specific model grid and island slope reflect a relative rise in sea level of 1m, which is also a plausible rise in sea level by the end of the century [DeConto and Pollard, 2016]. Our models are, however, applicable to any sea level rise that results in flooding of inland depressions that are at lower elevations than future sea level. Land surface areas receive 20 cm/yr of effective recharge, but lake areas have an effective lake evaporation of 50 cm/yr. The effective land surface recharge and lake evaporation rates are thus similar to Long, Cat, Exuma, and San Salvador islands.

Because lake positions with respect to island coastlines and widths are variable across the Bahamian Archipelago, subsequent simulations examined impacts of lake widths, lake position relative to island centers, and lake evaporation rate. Effective lake evaporation was changed from

10 cm/yr (similar to southern Abaco) to 60 cm/yr (similar to Crooked Island and Long Island) as a proxy for climate. We simulated lake expansion with sea level rise in increments of 0.1 m; the initial lake had a 100m base width, lake side slopes of 0.004 m/m, and evaporation of 50 cm/yr. To simulate impact of lake position on lens volumes, we migrated a 100m wide lake from the island center to within 100m of the coast and used a lake evaporation rate of 50 cm/yr. We normalize the changes in lens depth by dividing by the lens depth for an island with no lake and thus report the results as fraction changes in the lens depth.

### 5.3 Results and Discussion

In simulation 1, a 1000m wide island with no lake has a maximum potable freshwater lens thickness of ~0.7, with a brackish zone extending down to approximately 1.0 dimensionless depth (Figure 5.2a). These dimensionless depths correspond to absolute depths of 8 to 11m for a 1000m wide island and are similar to Eleuthera, Exuma, and Long islands, which have similar widths and have average maximum lens thickness of 10.2 m, 11.8 m, and 6.2 m, respectively [Cant and Weech, 1986]. Coastal inundation that reduces the island width by 10% (scenario 2; Figure 5.1a) decreases the maximum dimensionless lens thickness by 21% (Figure 5.2b). In contrast, when 10% of the island is inundated by formation of a central lake (scenario 3; Figure 5.1b), the freshwater lens splits into two and reduces maximum lens thickness by 47% (Figure 5.2c). Despite equivalent amounts of inundation, reduction in lens thickness is greater when inundation occurs by elevation of water tables into a central depression than through direct coastal inundation by rising seas (Figure 5.2d).

Freshwater lens thicknesses depend on lake widths, locations of lakes relative to island centers, and evaporation rates. Expansion of a lake in the center of an island (Figure 5.3a) from 0.1 to 0.2 of the island width shrinks freshwater lenses from 53% to 12% relative to the lens

volume on a lake-free island. Lake position reduces lens volume from 81% for lakes near an island's coast to 53% for lakes in the center of the island (Figure 5.3b). Increasing evaporation rates from 10 cm/yr to 60 cm/yr decreases freshwater lens volumes from 87% to 49% of the volume of a freshwater lens on a lake-free island (Figure 5.3c).

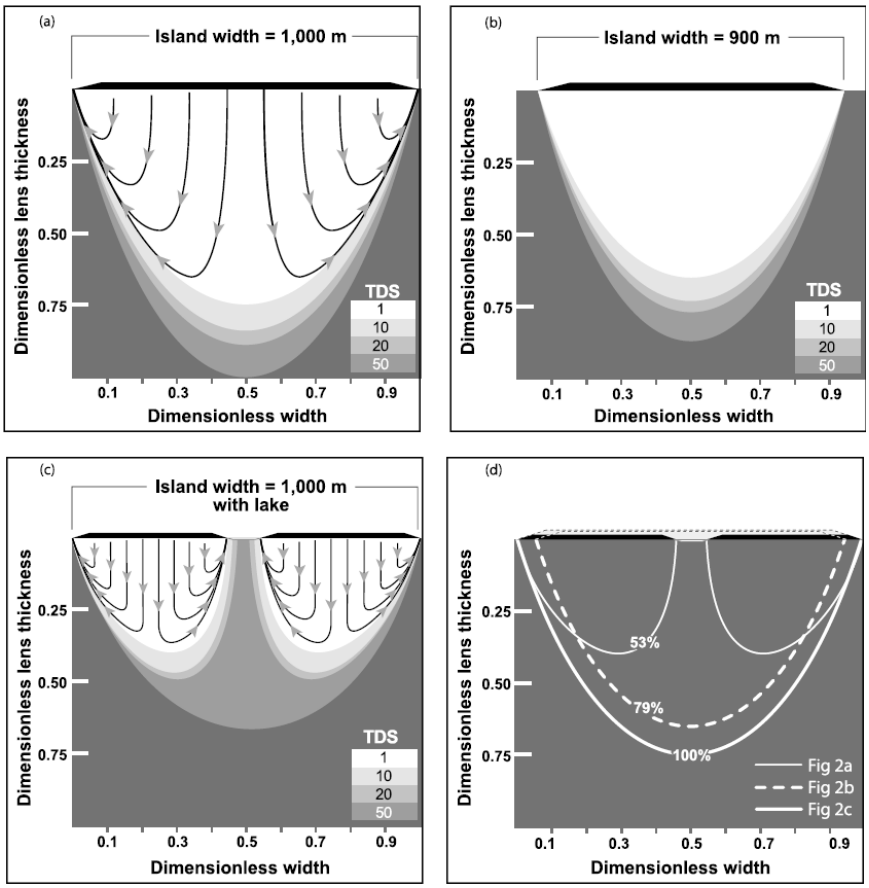


Figure 5.2 – (a, b) Comparison of magnitudes of freshwater lens thinning due to a 100m reduction in island width from sea level rise (scenario 1) relative to (c) formation of a 100m wide lake (scenario 2). TDS concentrations are normalized to maximum potable water concentrations (0.5 kg/m3). Lateral distance is normalized to island width distances (1000 m). Vertical distance is normalized to the maximum depth of the seawater (TDS = 35 kg/m3 or dimensionless TDS = 50) contour for the nonlake case (11 m). Model parameters (recharge, hydraulic conductivity) are identical for each simulation and are described in Methods. Baseline scenario for all following estimates of lens volume that shows the thickness of and groundwater flow path directions in a lens formed in a 1000m wide island without lakes (Figure 5.2a). Thickness of a lens in an island where sea level rise reduced island width to 900 m. Flow paths in this situation would mimic those in Figure 5.2a (Figure 5.2b). Groundwater flow paths and thicknesses of two freshwater lenses that remain after sea level rise elevated the water table into a depression to form a 100m wide lake (Figure 5.2c). (d) Comparison of the portions of freshwater lenses that contain potable water (defined as less than or equal to 0.5 kg/m3 total dissolved solids) in scenarios 1 and 2 and the percentage reduction relative to the base case shown in Figure 5.2a. (Reproduced from Gulley et al, 2016).

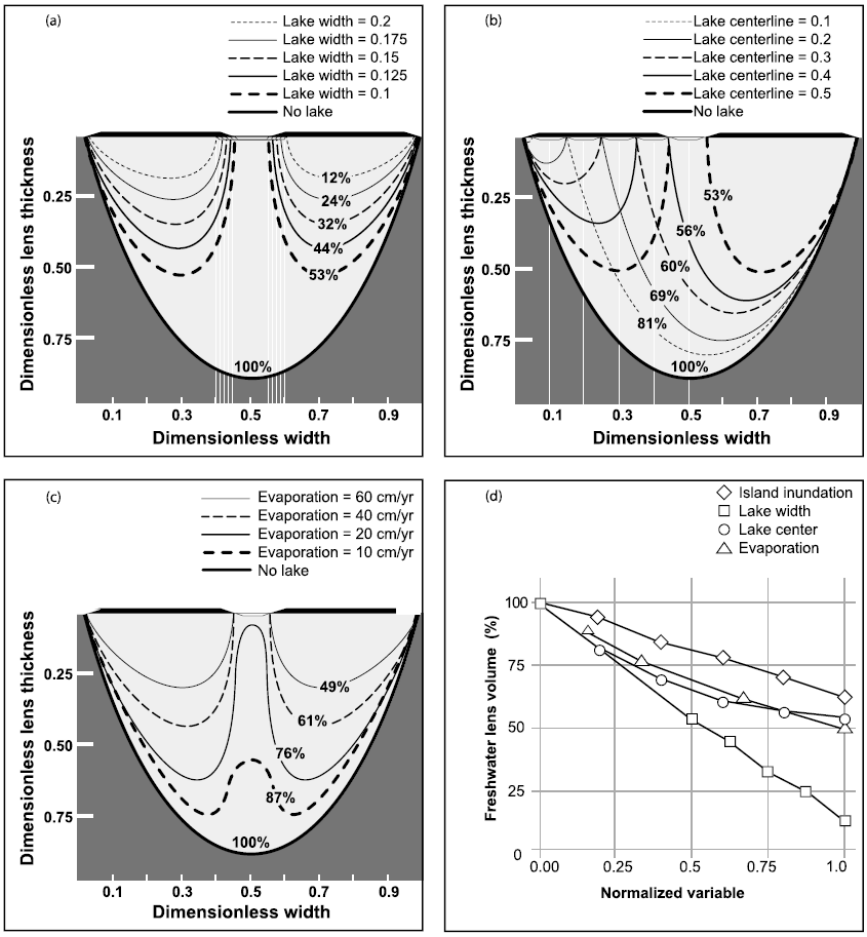


Figure 5.3 – Comparison of different sea level rise and lake formation scenarios on lens thicknesses. Only portions of the lens that contain potable water are shown. Lateral distance is normalized to island width distances (1000 m). Vertical distance is normalized to the maximum depth of the seawater (TDS = 35 kg/m3 or dimensionless TDS = 50) contour for the nonlake case (11 m). The percentage values show the change in volume of the new lens relative to a 1000m wide island with no lake (i.e., Figure 5.2a). (a) Lake width expansion from 0.1 to 0.2 at 0.025 increments, normalized to island width (1000 m). (b) Position of a 100m wide lake with respect to the island center. Lake positions are indicated for each case, normalized to island width (1000 m). (c) Increasing evaporation rates from 10 cm/yr to 60 cm/yr in a 100m wide lake in the center of the island. (d) Comparison of the relative impacts of each sea level rise scenarios in Figures 5.3a–5.3c, as well as island inundation by coastal flooding (e.g., Figures 5.2a and 5.2c), on lens thickness. All changes to lens thickness are in reference to the base case scenario of a 1000m wide island with no lake and are expressed as a percentage of lens thickness for that base case. Island inundation, lake width, lake center, and evaporation rate are normalized to maximum values (800 m, 200 m, 500 m, and 60 cm/yr, respectively). (Reproduced from Gulley et al, 2016).

Figure 5.3d summarizes the changes in freshwater lens volume as a function of variations in lake properties and sea level rise. The reduction of freshwater lens volumes is approximately

linear with evapotranspiration, lake width, and magnitude of coastal inundation but is curvilinear as lake positions approach the coast (Figure 5.3d). Increased lake widths decrease freshwater lens thicknesses by approximately 2.3 times that of coastal inundation for a given unit sea level rise. In contrast, increasing the magnitude of evaporation from a lake that is 0.1 times the island width results in about 16% more thinning than coastal inundation alone.

These simulations show that in dry climates such as the Bahamian Archipelago, the presence of lakes, their position on the island, and most importantly lake width reduce groundwater resources more than coastal inundation (Figure 5.3). While coastal inundation reduces land area available to recharge and shortens groundwater flow paths, forming lakes reduces water resources by acting as large diameter wells that discharge groundwater to the atmosphere through evaporation. Lake evaporation locally lowers the water table relative to sea level, raises the base of the fresh water lens, and reorganizes groundwater flow paths (Figures 5.2a and 5.2c). Prior to lake formation (Figure 5.2a) groundwater flow paths radiate toward the coast from a central potentiometric high. Lowering of the lake elevations by evaporation reorients some groundwater flow paths toward the lake (Figure 5.2c). Lakes forming in the center of an island tend to have greater impacts on lens thinning than coastal inundation because the length of the flow path (and recharge) controls the maximum elevation of the water table above sea level, which controls lens thickness. In contrast, where lakes form close to the coast, one side of the island maintains a larger, continuous water table that has longer groundwater flow paths and higher water table elevations. Consequently, impacts to overall lens thickness decrease as the lake approaches the coast (Figure 5.3b).

Lakes also exacerbate groundwater resource loss resulting from locally changing climatic conditions that would result in higher effective lake evaporation rates. Models of increased lake

evaporation from 0.5 to 3 times the aquifer recharge (10 to 60 cm/yr) reduced lens thicknesses from 87% to 49% of the lake-free island (Figure 5.3c). Carbonate islands in the Caribbean, most of which have lakes, are expected to have drying conditions in the coming century [Taylor et al., 2013], indicating impacts from lakes should be considered in future water resources assessments. In contrast, islands that have positive annual water budgets would have steady state freshwater lenses that look like the no lake scenarios (e.g., Figures 5.1a and 5.1b). Evaporation of such lakes during dry seasons or droughts, however, could result in seasonal depletion of water resources, but transient simulations, which require code development, are needed to address this issue.

Ultimately, predictions of how groundwater resources on individual islands will respond to sea level rise require high-resolution topographic and water table elevation data. These data would allow estimates of when and where lakes would form, and how large they would be given various sea level rise scenarios. Nonetheless, models presented here suggest that lake formation and growth should be included in assessments modification of groundwater resources with sea level rise and provide methodology for such assessments.

## 5.4 Conclusions

While direct inundation of island coastal areas is a well-recognized threat of sea level rise, lakes can form where sea level rise elevates water tables above low points in surface topography. Consequently, lake formation may increase areas of islands that can flood in response to sea level rise. On islands with negative water budgets, lake formation will reduce groundwater resource availability relative to islands that have topography that is not conducive to lake formation. Lakes formed within low-lying islands, in which evaporation exceeds precipitation, act like withdrawal wells and substantially reduce groundwater resources.

## Chapter 6 – Investigation of Transient Freshwater Storage in Island Aquifers

Fresh groundwater in an island aquifer is an extremely important resource that is highly vulnerable to variations in natural weather cycles and climate change effects. On small islands, precipitation creates subsurface freshwater lenses that float on top of coalesced saltwater that has intruded from the surrounding seawater. The volume and shape of these highly vulnerable freshwater lenses depend on the size and shape of the island, underlying geology, and the rate and duration of groundwater recharge. This study focuses on the transient changes in freshwater storage volume within these lenses. We completed a sand tank experiment to visualize an evolving freshwater lens that undergoes a dry and a wet cycle resulting in forming a shrinking and an expanding lens. The physical experiments provided a data set to develop a robust numerical model that can more rigorously simulate different types of evolving transient freshwater lenses. Our laboratory data along with past literature information have indicated that shrinking of the freshwater volume occurred at a slower rate relative to an expanding freshwater lens. This aspect of a rather rapid freshwater volume recovery was investigated further using the numerical model by imposing cyclic recharge patterns to study the impacts of shortened recharge periods on freshwater storage in island aquifers. The results show that a sustainable dynamic equilibrium condition can be achieved within a few cycles of periodic recharge. Unsustainable conditions were only encountered at extremely short recharge periods. The model was then extended to simulate a freshwater lens in Dauphin Island, Alabama, to assess changes in freshwater storage under realistic wet and dry cycles. The experimental data together with the modeling results presented in this study provide a better understanding of transient changes in freshwater storage patterns in small islands.

## 6.1 Background

According to estimates by the United Nations, the Small Island Developing States (SIDS) have a combined population of about 65 million (UN-OHRLLS, 2015). Most of these islands have a limited amount of surface storage potential to capture freshwater and therefore groundwater aquifers are critical water resources in these islands. On several of these islands, streams and lakes are simply non-existent, hence the local groundwater has to be optimally used to support the needs of local communities, agriculture, and also to support the local tourism industry that could be a major source of income for these tropical islands (Custodio and Bruggeman, 1987; Díaz Arenas and Febrillet Huertas, 1986).

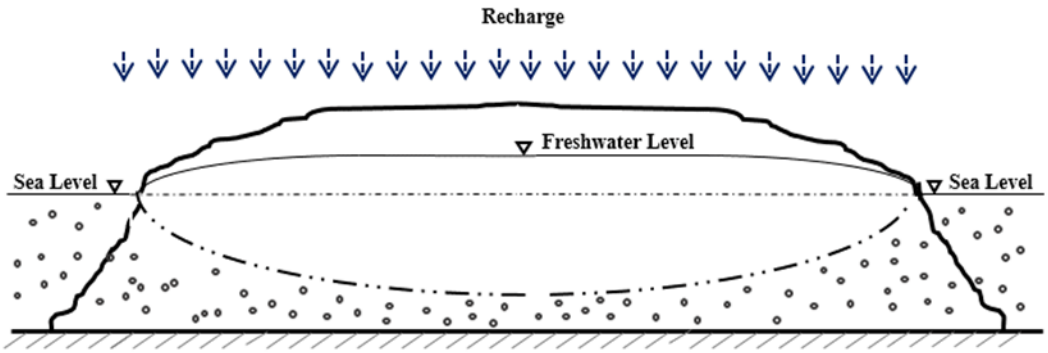


Figure 6.1 – Schematic of a freshwater lens in a strip island.

Freshwater recharge entering into a typical strip island aquifer will float over the intruded dense saltwater, forming a lens (see Figure 6.1). The extent of this freshwater lens will depend on the geology, recharge, and the shape and size of the island. Changes in precipitation patterns due to climate change effects and sea level rise can adversely impact the size and shape of the freshwater lens which, in many cases, could be the only source of potable water in small islands (Falkland and Custodio, 1991). Therefore, understanding the transient behavior of these

freshwater lenses is vital for optimally managing the limited amount of fresh groundwater available in these islands.

Since the mid-1960s, due to industrialization and rapid population growth, freshwater in small islands has been depleted and hence small island aquifers have become the focus of several theoretical and field investigations. Researchers have presented analytical and semi-analytical solutions for predicting the location of saltwater-freshwater interface in coastal aquifers including islands (Henry, 1960; Henry, 1964; Fetter, 1972; Ketabchi et al., 2014). Numerical models have also been used by researchers to study freshwater lens beneath oceanic strip islands; for example, Anderson (1976) used a predictor-corrector technique to develop a finite difference model for predicting unsteady flow in a freshwater lens beneath an oceanic strip island; Underwood et al., (1992) analyzed a two-layer atoll island and concluded that mixing of freshwater and saltwater occurs primarily as a result of oscillating vertical flow due to tidal fluctuations. Other studies have focused on field observations on islands. Wheatcraft and Buddemeier (1981) collected field data in Enjebi Island located within Enewark Atoll; Ayers and Vacher (1986) presented a detailed hydrogeological study of a small island called Deke on Pingelap Atoll located within the Eastern Caroline Islands; Presley (2005) studied the effects of the 1998 drought on Majuro Atoll, Marshall Islands; and Duncan (2011) provided a vulnerability assessment of fourteen developing Pacific Island Countries. UN-OHRLLS (2015) investigated the vulnerability of various freshwater resources in small islands, particularly to changes in precipitation patterns and prolonged drought conditions and pointed out the importance of rainwater harvesting in developing sustainable water resources in island aquifers.

Researchers have also developed several physical and mathematical models to study the freshwater flow processes near a saltwater wedge in coastal aquifers (e.g., Chang and Clement,

2013; Chang, et al., 2011; Goswami and Clement, 2007; Gulley, et al., 2016; Michael, et al., 2005; Robinson, et al. 2007). However, almost all of these efforts involve a uniform freshwater flow system with a single saltwater wedge intruding from the coastal boundary. In recent years, studies have investigated freshwater lenses bounded by double wedges in idealized sand-tank models (Stoeckl and Houben, 2012; Stoeckl, et al., 2016). Stoeckl, et al., 2016 provided a benchmark analysis employing the Simpson and Clement (2003) coupled-uncoupled analysis to establish that double-wedge problems are highly worthy benchmark problems for testing density-coupled flow codes. Dose, et al. (2014) investigated the steady-state interface geometry of freshwater lenses in layered aquifers. Stoeckl, et al. (2015) investigated groundwater age stratification and travel times in a non-homogeneous island aquifer. Houben, et al. (2018) demonstrate using physical and numerical experiments, the influence of discrete and spatially distributed heterogeneity on forming unique distribution of saltwater interface.

Climate change effects can dramatically change the rainfall patterns worldwide, increasing the annual rainfall variability of many islands (Duncan, 2011; UN-OHRLLS, 2015). Furthermore, large-scale, ocean-atmospheric cyclical events such as El Niño and La Niña could force periodic dry and wet hydrological cycles. Extreme events, such as extended droughts, resulting from the coupling of these ocean-atmosphere cycles with climate change could potentially lead to extremely low recharge and even zero recharge during lengthy drought periods (Duncan, 2011; Falkland, 1992; UN-OHRLLS, 2015). For example, during the 1982-83 El Niño event rainfall in many parts of western Pacific was only 10-30% of the long-term average (Falkland, 1992). These extreme drought events could induce severe saltwater intrusion in island aquifers and this can adversely impact the highly vulnerable population living in these islands. The consequences of such extreme dry and wet cycles are difficult to predict. For

example, it is currently unclear whether rainfall events resulting from wet cycles would be able to fully reverse the adverse impacts of dry cycles and reestablish a productive freshwater lens.

In published literature, there have been a few studies that examine the temporal changes in the saltwater interface after a dry and wet recharge cycle. Chang and Clement (2013) studied the movement of saltwater wedge and identified the asymmetry in intruding and receding saltwater wedges after a dry and wet cycle. Stoeckl and Houben (2012) and Stoeckl, et al. (2016) examined the asymmetry between the time needed for the change in the height of saltwater interface during the development and depletion of the freshwater lens using both physical and numerical models. Lu and Werner (2013) used a numerical model to quantify the timescale associated with the saltwater wedge toe response in a confined aquifer system due to water level variations at the boundary and inland and developed empirical relations relating the changes in boundary head with toe locations. Abdoulhalik and Ahmed (2018) studied the transient motion of toe location of a single saltwater wedge using a physical tank model and simulated the data using a numerical model. The study examined the temporal response of saltwater interface using different hydraulic conductivity material and also using different boundary conditions.

All aforementioned studies have investigated the temporal changes in saltwater intrusion and retreating processes; however, none of the prior studies have quantified the changes in freshwater volume within islands or explored the temporal changes in freshwater storage patterns due to variations in recharge cycles. The objective of this study is to perform both qualitative and quantitative analyses of the temporal changes in the two-dimensional patterns of freshwater lens in strip islands, which are impacted by wet and dry recharge cycles. Both experimental and numerical modeling studies were completed to explore the temporal asymmetry between the freshwater lens depletion and lens formation under dry (no recharge) conditions and wet

(recharge) conditions, respectively. Additionally, in this study we investigated the impacts of cyclical weather patterns with extended drought periods on the freshwater availability in island aquifers. To extend the findings of the small-scale tank studies to field scale, and to assess the time scale of transient processes under real-world precipitation and aquifer properties, a field-scale numerical model was developed. The model was used to conduct a numerical modeling study for Dauphin Island, Alabama.

## 6.2 Methods

### 6.2.1 Laboratory Methods

Figure 6.2 shows the experimental sand tank model used in this study. The physical model was used to simulate the cross section of a strip island with ocean boundary at both sides. Freshwater input to the system was delivered through areal recharge, simulating the direct rainfall-induced recharge over the entire island aquifer. The dimension of the plexi-glass tank is: 50 cm × 28 cm × 2.5 cm. The overall thickness of the experimental aquifer is much smaller than its length and width, hence the tank can be conceptualized as a two-dimensional aquifer system.

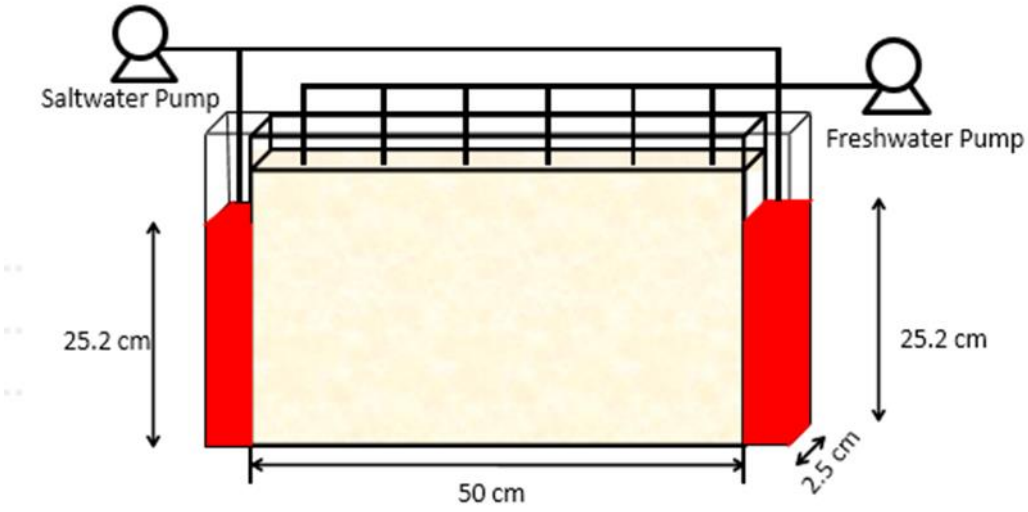


Figure 6.2 – Schematic of the laboratory setup.

As shown in the figure, the flow tank has three distinct sections: a right-hand seaside chamber, a central porous media chamber and a left-hand seaside chamber. Our past experience suggested that using sand in the tank led to a wider range in measured values of hydraulic conductivity. Therefore, the central section was first packed with uniform glass porous medium, i.e. glass beads of 1.1 mm diameter. Hydraulic conductivity was measured by creating a head gradient across the tank and measuring flow rate and head differences between the ends of the tank, for various flow rates. The porous medium was packed under water by submerging the entire tank within a large water container. Glass beads were added layer by layer and each layer was compacted manually before adding the next layer. Packing the tank under submerged conditions helped prevent air bubbles getting trapped within the system. Constant head boundary conditions were maintained at both left and right seaside boundaries by continuously pumping dense water, simulating seawater, into the two chambers. The head in these chambers were maintained at a fixed level and the excess volume of seawater was allowed to overflow through multiple 1 mm diameter holes drilled in the side plates of the tank. The experimental method used was identical to the approach discussed in Goswami and Clement (2007). During our experiments, the measured values of constant head in the two chambers were 25.2 cm and 25.5 cm, for the dry (no recharge) and wet (recharge) cycles, respectively.

The denser water representing seawater was colored red using a food-grade dye; our previous investigations have shown that the dye used did not adsorb to the glass porous medium used in this study (Chang and Clement, 2013; Goswami and Clement, 2007). The saltwater was prepared using non-iodized salt, and the food dye was added at a ratio of about 50 ml per 20 L of saltwater. The density of the saltwater was measured using the ASTM 11 H hydrometer, and the

measured density of the colored saltwater was 1.016 ± 0.001 g/ml. The measured density of freshwater was 0.999 ± 0.001.

To simulate areal recharge, a multi-head peristaltic pump (Masterflex Tygon E-3603 pump) was used to deliver flow at 6 injection points. Before using the pump, the pumping rate of individual heads were measured and at different speeds to ensure uniform pumping. The total amount of recharge distributed from the six recharge points was 252 ml/min. The total area over which the recharge was applied was 50 cm × 2.5 cm, making the recharge rate equal to 2.016 cm/min. The recharge tubes were placed on the top of a porous media chamber at distances of 4.2 cm, 12.5 cm, 20.8 cm, 29.1 cm, 37.4 cm and 45.7 cm away from the left boundary. A porous cotton cloth was placed at the top of the porous media chamber to uniformly distribute the recharged water over the entire area of the aquifer. The experiments were recorded using a digital camera, and the pictures were later post-processed to map wedge locations and to calculate freshwater lens volumes.

The first set of experiments were conducted under uniform areal recharge conditions (2.016 cm/min) to simulate an initial steady-state wedge. Later, two different dry and wet stress periods were applied to the sand tank system to induce transient conditions. The dry stress period started at 0 minutes and lasted for 45 minutes; during this period, the areal recharge was turned off to allow the red-colored denser saltwater to intrude into the sand tank from both sides, allowing us to record the shrinking phase of the freshwater lens under dry conditions. After 45 minutes, the wet stress period was started by turning on the areal recharge (recharge flow was maintained at 2.016 cm/min) and system was allowed to evolve for another 45 minutes, allowing us to record the redevelopment phase of the freshwater lens under wet recharge conditions.

### 6.2.2 Modeling Methods

SEAWAT (Langevin, et al., 2008), a three-dimensional variable-density groundwater flow and transport simulation code, was used to develop a numerical model for this study. To simulate the two-dimensional flow tank experiment, the numerical model was discretized into 50 layers, 1 row, and 102 columns to represent the tank with dimensions 25 cm in height and 50 cm in width. The two model columns at both ends were used for specifying lateral boundary conditions. Layers and columns were discretized with 0.5 cm grid spacing, with the exception of model layer 1, the top layer, that represents the water table layer. The top layer was assigned a thickness of 2.5 cm to accommodate the changes in phreatic surface levels and simulate unconfined flow conditions.

An average uniform hydraulic conductivity value of 1,050 m/day, which was measured in the laboratory, was assigned to the entire model domain. The confined storage coefficient was assumed to be negligible and was set to a very low value of 10-7. Porosity value was set to be equal to 0.39, which was the average measured value-. The left and right boundaries of the model were imposed as prescribed head and prescribed concentration boundaries. A uniform recharge boundary was imposed at the top, and the bottom face of the model was simulated as a no flow boundary. The densities of freshwater and saltwater were set to 999 and 1,016 kg/m3, respectively. Assuming a concentration of 35 kg/m3 for the red-colored denser seawater (which is close to the actual seawater concentration), the slope of the linear equation of state that relates of density and concentration ($\partial\rho/\partial C$) was estimated to be 0.4857. Note, in SEAWAT any arbitrary concentration value can be assumed provided an appropriate density slope value is calculated and used to simulate consistent scaled concentration results.

Temporal discretization included three stress periods: (1) the initial period to simulate the initial-steady-state conditions with constant recharge; (2) a transient forty-five minutes period without recharge (zero recharge to simulate dry conditions); and (3) a transient period with uniform recharge (to simulate wet conditions). For the three stress periods, prescribed head values at the lateral boundaries were set at 25.5 cm, 25.2 cm, and 25.5 cm, respectively; and recharge was set at 2.016 cm/min for the first and third stress period and zero for the second stress period. For numerical stability, flow and transport were tightly coupled with equal flow and transport time-step sizes, set at 0.54 seconds. SEAWAT uses a generalized conjugate gradient solver to solve the linear system of equations for dispersion, sources, and sinks, and the total variation diminishing (TVD) scheme was used as the advection solution scheme which calculates the time-step size honoring the Courant number (Cr) constraint of Cr <= 1. The numerical model was later extended to simulate the impacts of cyclical wet-dry conditions on the experimental system. In addition, we also present a real-world case study that simulated a freshwater lens in Dauphin Island, Alabama to assess realistic timescales of freshwater volume change. The model parameters used in this case study are discussed in detail in the case study section.

## 6.3 Results and Discussion

### 6.3.1 Steady-State Experimental Conditions

Figure 6.3a shows the symmetric salt wedges obtained under steady-state conditions. To obtain these steady-state profiles, the aquifer was originally filled with freshwater and then forced with saltwater boundary conditions; this was accomplished by replacing the freshwater in the left and right reservoirs with seawater by pumping the excess amount of saltwater. The saltwater head at the two boundaries were maintained at a constant level, and the recharge from

the top remained zero. These conditions allowed red-colored saltwater to rapidly intrude from both sides into this recharge-free freshwater aquifer. After about 10 minutes of intrusion, the recharge pumps were turned on to maintain a constant flow rate of 2.016 cm/min, which was uniformly distributed over the top of the aquifer. The recharged system was allowed to evolve for about an hour to reach the steady state condition shown in Fig 6.3a. These wedge profiles were set as the base case initial condition in this experimental study. At this steady state condition, the freshwater recharge supplied from the top fully balanced the saltwater forced from the boundaries forming two symmetric wedges.

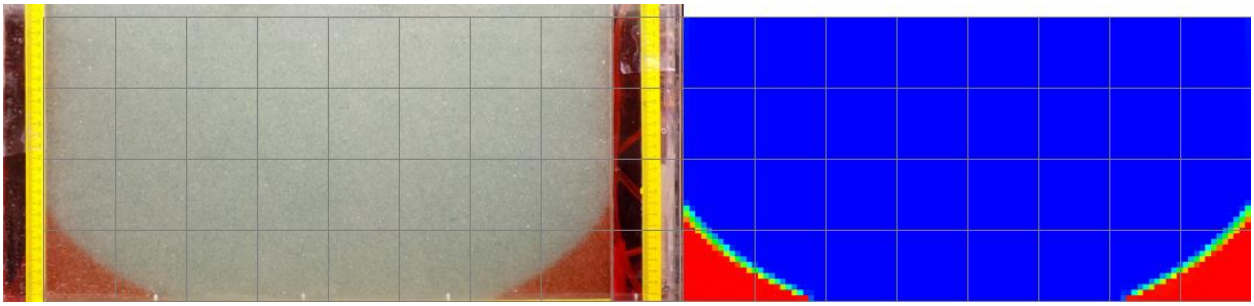

(a) (b)

Figure 6.3 – Steady-state saltwater profile (red represents saltwater): (a) laboratory observation; and (b) simulated results.

Figure 6.3b shows the steady-state conditions simulated using the SEAWAT model. The model was developed using the measured experimental parameters and it was run for a long time starting with a freshwater state as the initial condition. Figure 6.3b shows the model simulated steady-state profile. In the model, the top layer was simulated as an unconfined layer and all other internal lower layers were assumed as confined layers. The model was run in a predictive mode using low longitudinal and transverse dispersivity values of 0.01 and 0.001 cm, respectively. These values are similar to the values used in other experimental studies to simulate similar type of sharp saltwater wedges (Abarca and Clement, 2009; Chang and Clement, 2012; Goswami and Clement, 2007). Preliminary sensitivity simulations completed

using higher dispersivity values indicated that use of larger dispersivity values induced more dispersion than what was observed in the system. Larger dispersivity values in the simulations resulted in a more vertical saltwater wedge during saltwater intrusion. Comparison of Figure 6.3a and Figure 6.3b results indicate excellent agreement between the experimental data and numerical results.

### 6.3.2 Transient Experimental Conditions

The steady state system discussed above was used as the initial condition to simulate two distinct transient flow conditions involving dry and wet recharge cycles. In order to simulate transient conditions, we first instantaneously shut the recharge pump to simulate a dry cycle. The no-recharge condition was allowed to evolve for 45 mins to simulate a dry period. Transient salt wedge profiles observed after 5, 10, 15, 25, 35 and 45 minutes are shown in the left panel of Figure 6.4. As shown in Figure 6.4a, in the initial steady system the recharge flow minimizes saltwater intrusion effects and the wedges intruded only to about 10.4 cm from both saltwater boundaries. Figure 6.4b shows that once the recharge was stopped, the wedges started to rapidly intrude into the system from both sides and the toe of the wedge reached about 18.75 cm from the lateral boundary after 5 minutes of transport. After about 11 to 12 minutes of transport the two wedges started to coalesce close to the center of the tank, and Figure 6.4c shows the fully merged wedge observed after 15 minutes. It is interesting to note that after coalescing, the wedges formed a “V shaped” profile with the lowest point located at about 6.25 cm from the bottom of the tank. With time, the wedge developed a “U-shaped” profile and the low point started to lift and was located at about 14, 18.5, and 20.3 cm from the bottom of the tank at 25, 35 and 45 minutes, respectively (see Figures 6.4d, 6.4e and 6.4f). Note the true steady-state pattern for this no recharge condition will be a flat profile, and our preliminary experiments

showed that it will take about 2 hours to approach this flat steady state condition where the saltwater will fully intrude and replace the entire freshwater. However, in this experiment, we only maintained the zero-recharge condition for 45 mins.

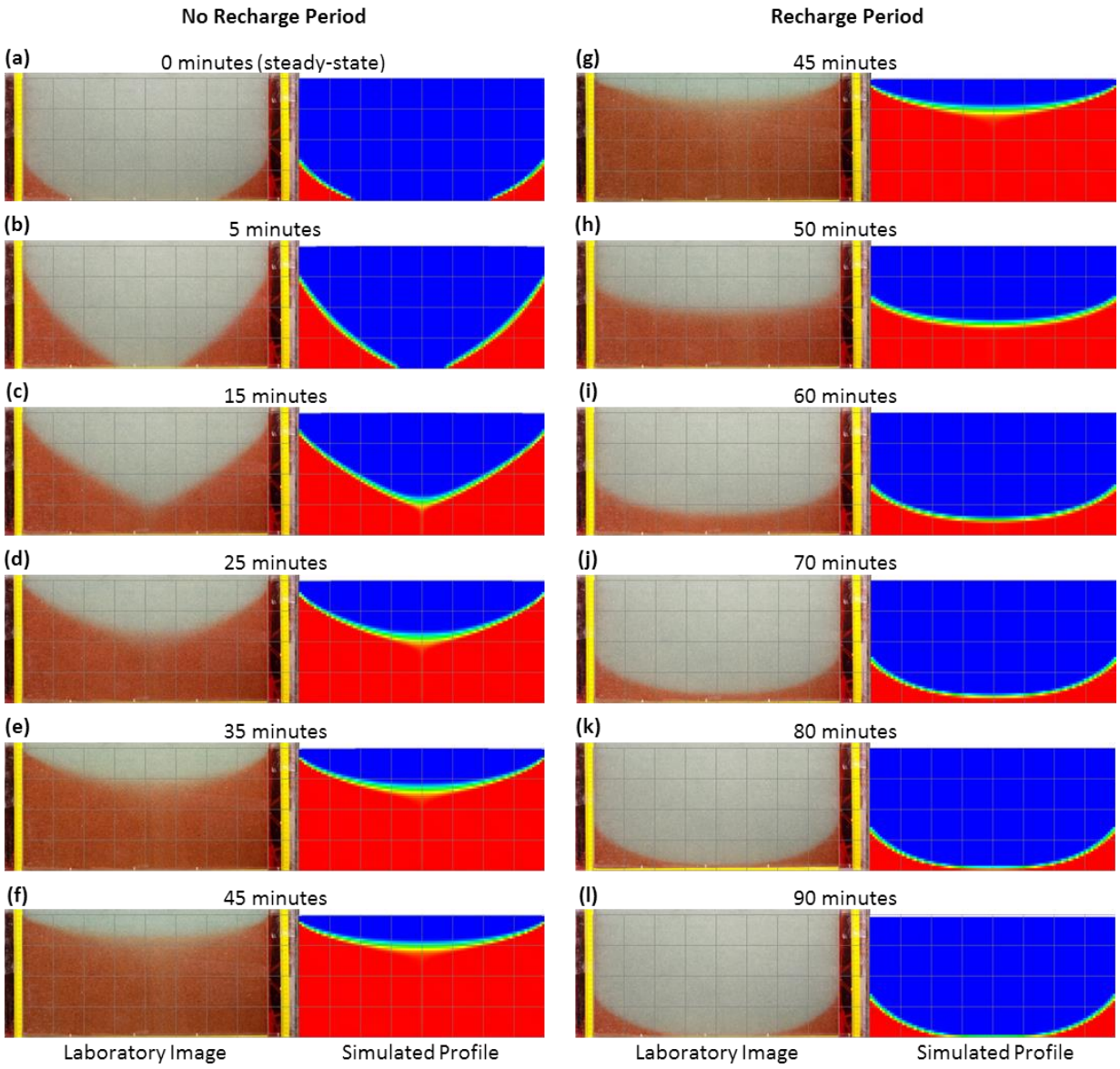


Figure 6.4 – Comparison of saltwater profiles observed in the experimental tank with model simulated results. The left side panels show data for 5 minutes to 45 minutes that represent transport under no recharge (dry) conditions during which the denser saltwater intruded into the system. The right-side panels show data from 45 minutes to 90 minutes that represent transport under recharge (wet) conditions during which the recharged freshwater displaced the saltwater out of the system.

To simulate the wet cycle, we turned on the recharge pump and supplied a uniform recharge at a rate of 2.016 cm/min, which was identical to the recharge used to simulate the base-case, steady-state wedge. The recharged water infiltrated into the aquifer and reestablished the freshwater lens by forcing the saltwater wedge to recede back toward the left and right seaside boundaries. The figures presented in the right panel of Figure 6.4 show the transient movement of the receding wedge. Interestingly, the intruding and receding wedges have very different patterns. One of the major differences was that the intruding wedge initially formed a V-shaped profile that later evolved into a U-shaped profile; whereas, the receding wedge always had an elongated U-shaped profile. In the past, research studies have primarily focused on the toe location of the saltwater wedge. However, in our dry and wet cycle comparison analysis we integrated the area above the wedge to quantify the total amount of freshwater storage in the system to define the state of the system. The volume of water stored at any given time was then used to compare the differences in the overall shapes of intruding and receding saltwater wedges.

Figure 6.4h shows the location of the receding wedge after receiving 5 minutes of recharge. The experimental data show that the system formed an elongated U-shaped wedge and the lower-most point of this wedge was located at about 12.3 cm from the bottom of the aquifer. Figures 6.4i, 6.4j, and 6.4k show the wedge profiles observed after 15, 25, and 35 minutes of recharge (or 60, 70, and 80 total minutes), and the low points of the wedges were located about 4.2, 1.8 and 0.7 cm from the bottom of the tank for the three cases, respectively. Figure 6.4l shows that after 45 mins of recharge (or total experimental time of 90 minutes) the wedges were totally disconnected and the toes of the two disconnected wedges were located approximately 13.5 cm from the boundary (note the true steady-state location is about 10.4 cm).

The SEAWAT code was used to simulate this dataset and the model simulated profiles of the intruding and receding wedges are also shown in Figure 6.4. These figures show that the model was able to closely reproduce the experimental observations. These results indicate that this stable-wedge problem has three states involving distinctly different types of salt wedge patterns including the traditional exponentially-decaying wedge, a V-shaped intruding wedge, and a U-shaped receding wedge. These data provide a unique set of transient wedge profiles which can be useful for testing density-coupled flow models that involve stable interfaces (i.e., dense water at the bottom).

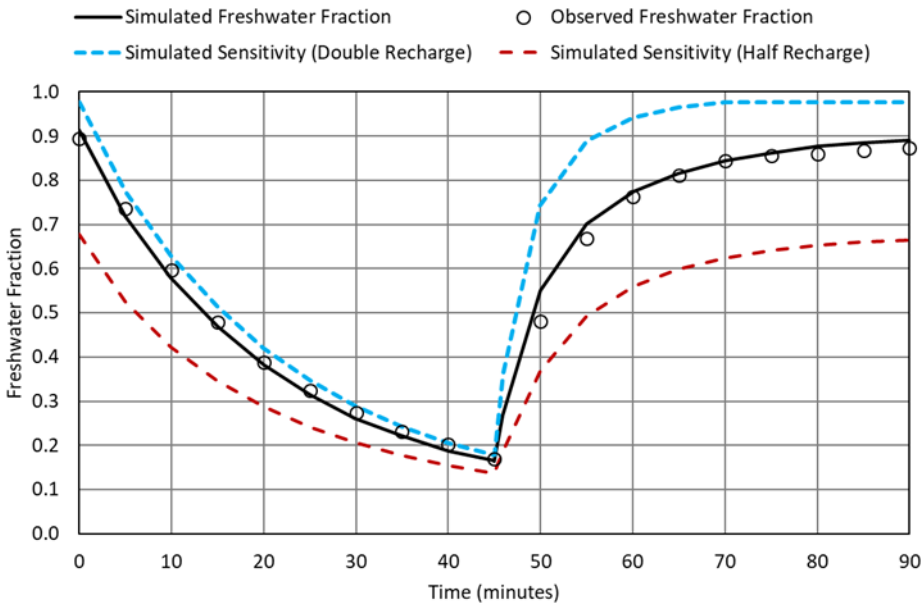


Figure 6.5 – Time series plot showing changes in freshwater storage. Note the storage volume is reported as a fraction of the total tank volume.

To quantify the changes in freshwater storage patterns, the amount of freshwater in the tank experiments was computed by post processing the digital images to estimate the area above the wedge. The simulated freshwater fractions were delineated using a threshold of a normalized concentration of 0.25. The changes in the amount of freshwater stored within the system estimated for different times are summarized in Figure 6.5. A good agreement is seen in

simulated and observed changes in freshwater fractions. Figure 6.5 also shows the sensitivity of freshwater fraction changes to recharge rate. The freshwater recovery is most sensitive to the recharge rate, and it is seen that the rate of recovery increases with the increase in the recharge intensity. The asymmetry observed between depletion and recovery cycles is enhanced with a higher recharge rate. For the base simulation, the figure shows that during both dry and wet cycles, the greatest change in the freshwater volume occurred during the inception of the transient period (this can also be seen in Figure 6.4). As time progressed, the rate of change of net freshwater storage decreased considerably. Figure 6.6 shows the absolute rate of change of freshwater storage observed during the dry and wet stress periods. For visual comparison, both the rate of decrease and increase in freshwater volume is plotted as the absolute value on the positive y-axis. These rates were calculated as the change in the freshwater fraction over time interval divided by the length of time interval over which the change occurred. When we compared these rates of storage change data for both dry and wet cycles during the first 10 minutes, the rate of change is high for the expanding freshwater lens which was accumulating water under receding saltwater wedge conditions during the wet period. Our estimations show that during the dry period, the freshwater fraction decreased by 33% (of the total storage) within 10 minutes; on the other hand, during the wet period, the storage increased to about 53% within 10 minutes. At the beginning of the wet period the recovery rate was almost double as compared to the depletion rate at the onset of the dry period. However, after the initial surge in freshwater storage, the rate of change slowed down as the freshwater forced the intruded saltwater to split into two separate wedges.

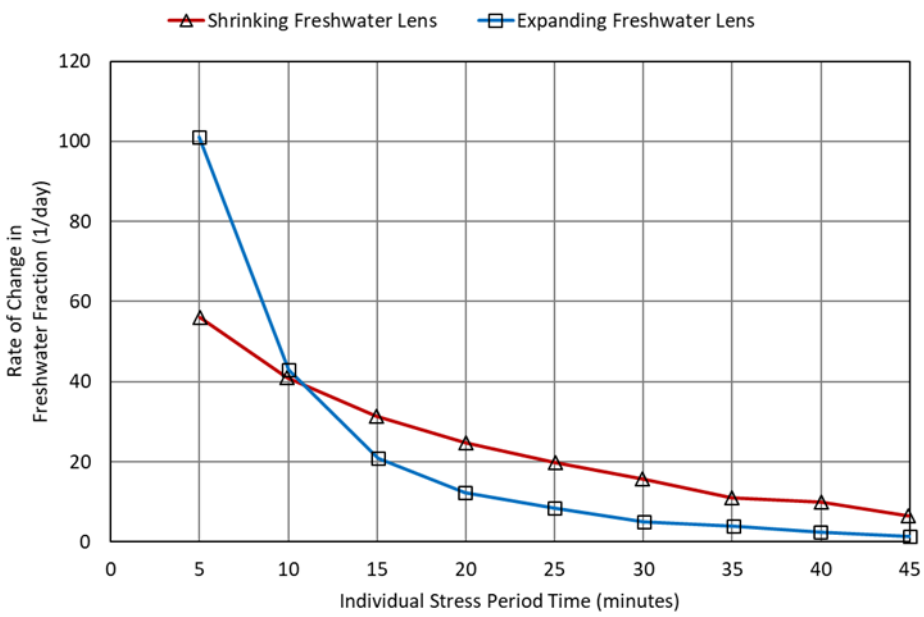


Figure 6.6 – Rate of change of freshwater fraction within the shrinking and expanding freshwater lenses. Note the x-axis represents individual stress period (dry or wet cycle) time.

Chang and Clement (2012) discuss potential reasons for the observed asymmetry between intruding and receding wedges. Based on their findings one can postulate that the asymmetry observed in the time-scale of shrinking and expanding freshwater lens can be attributed to the velocity variations occurring within the saltwater wedge during intruding and receding conditions. During intrusion (or shrinking freshwater lens conditions), saltwater flow from the lateral boundary is moving inward within the saltwater wedge, which will be opposite to the outward freshwater flow occurring within the lens. The freshwater flow will eventually exit through the lateral boundary within a narrow area close to the top of the tank. On the contrary, during recession (or expanding freshwater lens conditions), both freshwater and saltwater flows will align to move towards the lateral boundary and the entire lateral boundary area will be available for outflow; these processes facilitate the saltwater recession to occur at a much higher rate as compared to intrusion.

The results imply that the freshwater volume stored within a strip island will recover and accumulate water rather rapidly during the initial phase of a rainfall event, when compared to the freshwater volume lost during the initial phase of a drought event. Overall, these results show a unique emerging pattern where natural systems can potentially manage water storage rather efficiently. The findings observed in the laboratory-scale experiments were extended to a field-scale investigation using a numerical modeling study a realistic system in Dauphin Island, Alabama. The field-scale investigation uses real-world spatial domain, precipitation data, and aquifer parameters to observe expected time-scale in asymmetric transient processes and these results are discussed in Section 3.4.

### 6.3.3 Understanding Freshwater Sustainability under Variable Recharge Conditions

The observations made in the experimental study where the freshwater lens recovery process was found to be relatively faster than depletion led us to conduct further numerical simulations for the experimental system for cyclic wet-dry conditions. Cyclic wet-dry conditions were simulated using multiple stress periods. Steady-state conditions were simulated under constant recharge conditions as the first stress period. Dry conditions were invoked by implementing zero-recharge in even numbered stress periods, and recharge was implemented in subsequent odd numbered stress periods to represent wet conditions. One cycle of wet-dry conditions, therefore, comprised of two consecutive stress periods, one without recharge followed by one with recharge. Six such wet-dry cycles were simulated. The dimensions of the numerical model used for these simulations were the same as the sand tank model. The duration representing dry conditions in all simulations was set to a constant time of 25 minutes. However, the duration of wet periods was allowed to vary in different simulations. Note that the recharge rate was the same in all simulations, only the duration was varied.

For the first simulation, the recharge period was set to ten minutes, which resulted in a wet-dry cycle which was 35 minutes long comprising of a 25-minute dry period followed by 10 minutes of wet recharge period. Six such cycles were employed in all these simulation experiments. For the second simulation, the duration of wet period was reduced to 5 minutes and a dry period was set to 25 minutes; therefore, the duration of each cycle in the second simulation was 30 minutes. In subsequent simulations the recharge period was reduced to 2 minutes, 1 minute, and 0.1 minute. The last simulation with a wet period duration of 0.1 minute was considered as an extreme case of recharge period.

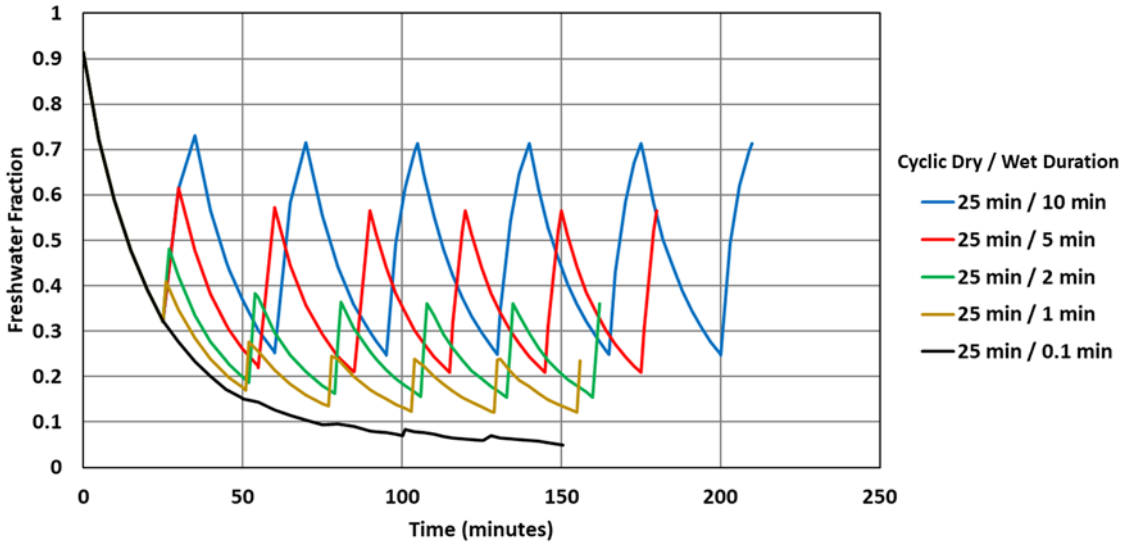


Figure 6.7 – Time series plot showing changes in freshwater storage for cyclic wet-dry simulations. Each simulation considers six cycles of wet and dry periods. A cycle comprises of a 25-minute dry period and varying duration of wet periods from one simulation to the other. The total time of each simulation varies depending on the duration of its wet period.

Figure 6.7 shows the time-series plots for all five cyclical wet-dry scenarios. The results show that the freshwater volumes decrease from one simulation to the other as the duration of wet period was decreased. Within every simulation experiment (which consisted for six cycles), a dynamic equilibrium was achieved after about three wet-dry cycles; i.e., the freshwater volume roughly changed by the same amount after three cycles. The only exception to that is the extreme

case of a recharge duration of one-tenth of a minute; in this case, the freshwater volume continued to decrease after every cycle.

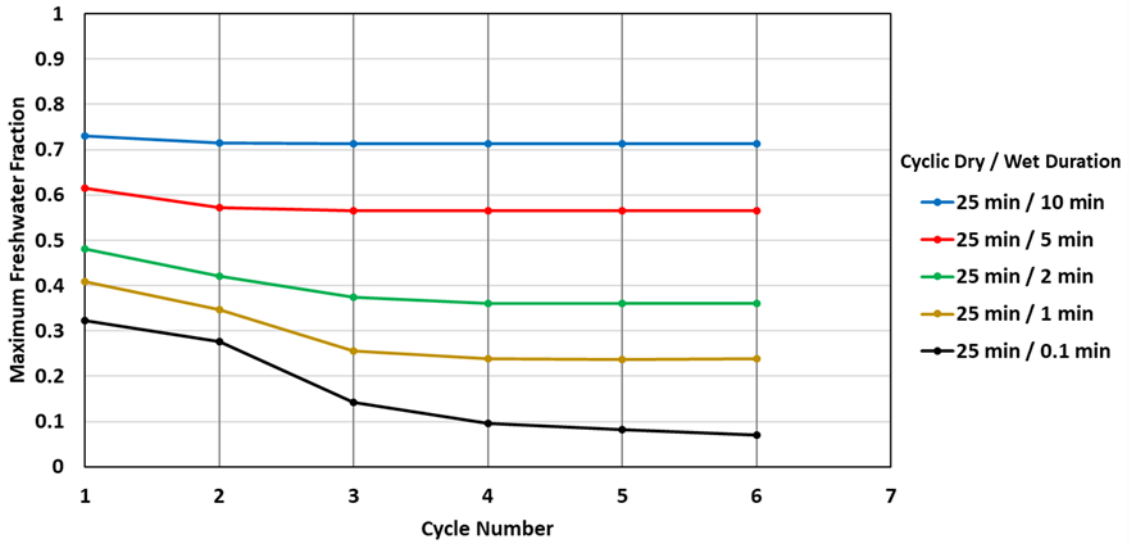


Figure 6.8 – Time series plot showing maximum freshwater storage within each wet-dry cycle. Six cycles were simulated for each simulation. The total duration of each simulation is different and is based on the duration of the wet period for that simulation.

Figure 6.8 shows the cyclic change in the maximum freshwater achieved at the end of each wet-dry cycle. The shape of the curve for each simulation stabilizes within a few wet-dry cycles indicating that a dynamic equilibrium is achieved, but with different freshwater volumes. The higher the duration of recharge, the higher is the freshwater volume achieved at the dynamic equilibrium condition. For example, with a 25-minute dry and a 10-minute wet cycle, the maximum freshwater volume fraction under dynamic equilibrium is found to be 0.71. Note the freshwater volume fraction indicates the fraction of system that is occupied by freshwater. For a simulation with recharge period as low as 1-minute and with a dry period of 25 minutes, the maximum freshwater fraction is 0.24 at dynamic equilibrium. As seen in Figures 6.7 and 6.8, a sustained freshwater volume level was attained for simulations in which recharge occurred as briefly as for 1-minute after a 25-minute dry period. Only when the recharge duration was

shortened to a tenth of a minute (with a 25-minute dry period) the freshwater lens became unsustainable. The result show that the freshwater recharge accumulated even during short recharge cycles can help sustain freshwater storage during extended dry periods.

### 6.3.4 Case Study for Dauphin Island, Alabama

A field-scale study was completed to assess the real-world implication of the observations made in this experimental study. Dauphin Island located at the southwest end of Alabama in the US was selected for this example. The western end of the island, which has an elongated strip of land of approximately 20 km long with an average width of approximately 400 m, was used as the model domain. This island region is ideally suited for simulating conditions on an infinite strip island. A cross-sectional model of the strip of land was created to assess changes in freshwater lens volumes. Parameterization of the field model was based on a modeling study of Dauphin Island presented by Chang, et al. (2016). The 400 m width of the strip was discretized into 160 model cells using a 2.5 m horizontal discretization. The depth of the model was selected as 21 m, the top hydrogeologic unit being 13 m thick representing Holocene Sand underlain by a 7 m thick clay unit (Chang, et al., 2016). The model grid was discretized vertically into 42 layers with a uniform vertical spacing of 0.5 m.

Real-world field conditions and rainfall data were used to simulate the freshwater lens in Dauphin Island, Alabama, to illustrate the differences in the rate of decrease and the rate of increase in freshwater volumes. Precipitation data was obtained for Mobile Regional Airport, Alabama available from NOAA's National Climatic Data Center (NCDC). Monthly calculated precipitation rates used for generating transient groundwater recharge for the model is shown in Figure 6.9. Net groundwater recharge was set at 5% of the precipitation amount. The figure shows a large monthly variation in precipitation values. On a larger timescale there was an

extended drought period between 2010 and the first half of 2011, which occurred in between two relatively wet years of 2009 and 2012 (see inset plot in Figure 6.9). Other site parameters were taken from the calibrated model parameters presented in a previously published study (Chang, et al., 2016), and the data are summarized in Table 6.1. The objective of this field scale simulation was to test whether the laboratory-scale observations made were applicable for field-scale conditions. Specifically, to test whether the freshwater recharge rapidly accumulated during the short recharge cycles will be able to sustain freshwater storage during extended dry periods. A transient model was simulated for the period of 2007-2013. To isolate the impacts of recharge on the freshwater volumes, only recharge was varied on a monthly basis during the transient period. All other boundary conditions were held constant. Initial conditions were set as steady-state conditions with average 2007-2013 recharge.

Table 6.1 – Model parameters used for Dauphin Island simulation (reproduced from Chang et al, 2010)

| Parameter | Sandy Upper Unit | Clay Lower Unit |
|---|---|---|
| Horizontal hydraulic conductivity | 13.7 m/day | $2.6 \times 10^{-7}$ m/day |
| Vertical hydraulic conductivity | 0.45 m/day | $2.6 \times 10^{-7}$ m/day |
| Specific storage | $3.3 \times 10^{-4}$ $m^{-1}$ | $3.3 \times 10^{-3}$ $m^{-1}$ |
| Longitudinal dispersivity | 0.0001 m | |
| Transverse dispersivity | 0.00001 m | |
| Saltwater concentration | 35 $kg/m^3$ | |
| Saltwater density | 1,025 $kg/m^3$ | |
| Freshwater density | 1,000 $kg/m^3$ | |
| Density slope | 0.714 | |
| Porosity | 0.3 | |

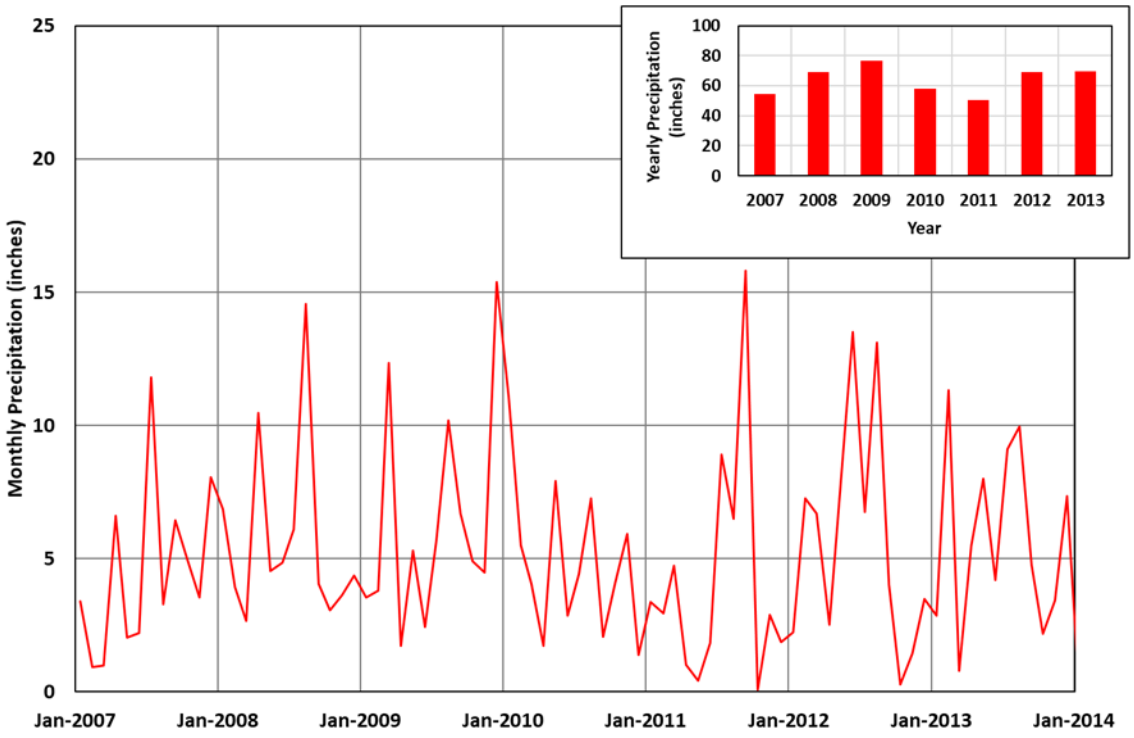


Figure 6.9 – Precipitation data from Mobile Regional Airport, Alabama used for Dauphin Island model. Monthly precipitation is shown as a time-series plot and the inset shows yearly precipitation.

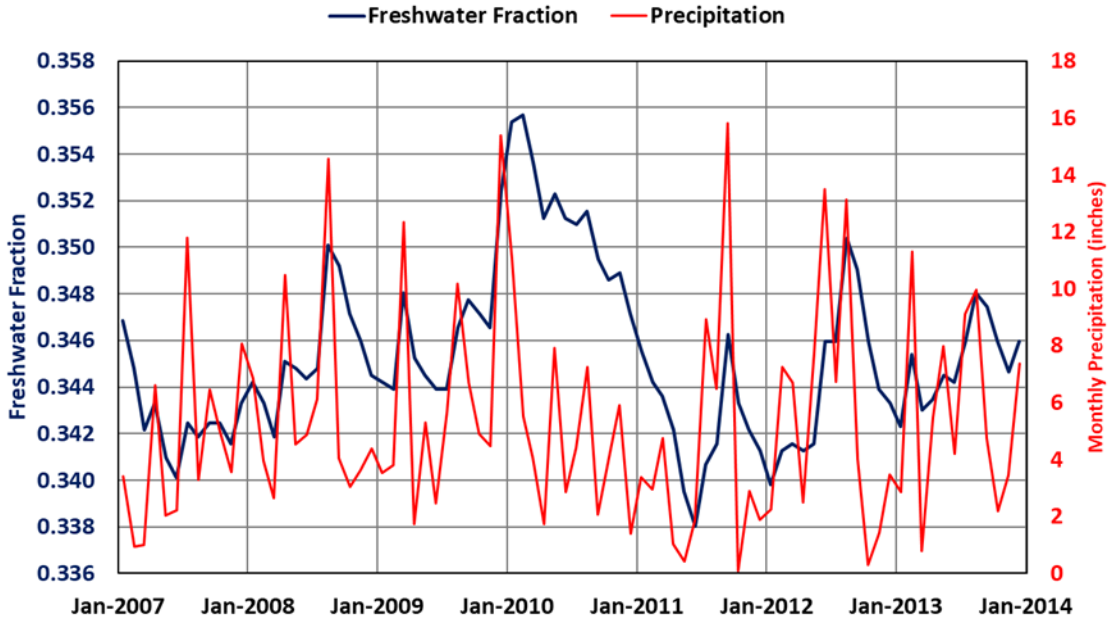


Figure 6.10 – Change in freshwater fraction for Dauphin Island model. Freshwater fraction is the volume of freshwater divided by the total volume of cross-section model. Precipitation is also plotted for comparison between change in precipitation and the induced change in freshwater volume fraction in the model.

Figure 6.10 shows the monthly variation in freshwater volume fraction predicted by the model. The relative changes in freshwater volume largely follow the variation in recharge applied to the model. Freshwater volume increases with increased recharge and vice versa. The results show that increase in recharge causes the freshwater to increase within the same month. Decrease in recharge however, shows a delayed response in freshwater lens depletion; the recession limb of the freshwater lens took several months to manifest on the decrease in freshwater volumes during dry cycles. This pattern can be observed in almost all the events in which recharge drops but it is most prominent during the extended dry cycle beginning in 2010 and lasting through the middle of 2011. During this period, the decrease in freshwater volume is not as drastic as the decrease in recharge conditions. Intermittent increase in recharge even by a small amount of rain in 2010 helped slow down the decrease in freshwater lens volume through the entire year. On the other hand, a large increase in 2009, 2011, and 2012 recharge is reflected by an almost instantaneous increase in freshwater volume. While the absolute change in freshwater volume may not be significant, it is interesting to note that, like the laboratory-scale results, these field-scale simulations also show a delayed pattern of freshwater lens depletion relative to the freshwater lens formation.

The real-world example simulated here qualitatively demonstrates the delayed response of freshwater volume depletion over several months due to the decrease in recharge and an almost instantaneous recovery of freshwater volume resulting from increased recharge. These observations highlight the importance of managing groundwater replenishment from even short rainfall events after or during an extended dry period. Efforts to capture recharge from these short rainfall events are consequential to better manage freshwater storage in island aquifers.

## 6.4 Conclusions

A laboratory experiment was conducted to study the patterns of a shrinking and expanding freshwater lens in an infinite strip island. The laboratory data were simulated using a numerical model developed using SEAWAT. The modeled results closely matched the experimental data. The data show asymmetry in the time scales of the shrinking and expanding freshwater lens. It was also observed that the initial period of stress causes the highest change in freshwater volume storage (both loss and gain) and the rate of change of freshwater storage rapidly decreases with the passage of time. Interestingly, the freshwater lens expansion (or accumulation of freshwater) during the early period of the wet cycle occurred at a greater rate when compared to the freshwater lens shrinkage (or loss of freshwater) rate during the dry cycle. These results show that natural systems could support an efficient non-linear feedback mechanism that has an emerging property where the groundwater system loses water slowly during a dry cycle, but it can recover fast by gaining water rather rapidly during a wet cycle. This non-linear feedback mechanism and its implication on faster freshwater recovery greatly emphasizes the importance of implementing careful recharge management strategies to maximize freshwater storage in small island aquifers. Our experimental data as well as model simulation results show that even short duration rainfall events can greatly enhance the freshwater availability within small islands.

# Chapter 7 – DRT3D: A Variable-Density Reactive Transport Simulator

Density-dependent flow and transport in the subsurface has been studied for more than a hundred years. In the past few decades, several experimental and modeling benchmark analyses have been presented by researchers for examining density-dependent solute transport. Independently, reactive transport has been studied by means of laboratory experiments, numerical simulations, and field investigations. Over the last two decades few studies have considered density-dependent flow and reactive transport working interactively. This study presents a first-of-its-kind benchmark for reactive transport involving dense plumes. Numerical modeling was conducted to simulate a two-dimensional sand tank, in anticipation of follow-up experiments, that would examine the reactions between two plumes that are subject to mixing enhanced due to density impacts. A new numerical code, DRT3D, was developed by implementing reactive simulation capabilities of RT3D into the density-dependent code SEAWAT. Preliminary verification suggests that the numerical implementation of DRT3D is correct, however, further validation is needed. The impetus for creating DRT3D code is to provide a simulation tool for designing and analyzing density enhanced mixing and reactions for improving the performance of in-situ remediation at contaminated sites.

## 7.1 Background

Density dependent flow and transport has been studied in great details for several decades. The studies have provided insights into several aspects of density dependent problems including coastal saltwater intrusion (e.g., Werner et al, 2013), upconing of saltwater interface due to pumping, water resources within small islands (e.g., Werner et al, 2017), transient movement of saltwater interface (e.g., Bedekar et al, 2019b), and unstable interfaces caused by denser plumes overlying lower density liquids (Elder, 1967). Density dependent flow and transport has been

investigated via laboratory experiments, field studies, simulation code development, and mathematical modeling.

Reactive transport in porous media is a challenging and complex field of study which has grabbed the attention of researchers for the past several decades. Past studies have provided a profound understanding of bio-geo-chemical processes of solute plumes within porous media and the topic continues to be the subject of much ongoing research (e.g., Parkhurst, 1995; Clement, 1997; Prommer et al, 2003; Poonoosamy et al, 2018). These studies have found their application in laboratory-scale experiments and field-scale groundwater remediation sites, and similar to density dependent studies, reactive transport has been researched via laboratory and field investigations, and further explored through simulation code development and modeling.

Density dependent transport and reactive transport processes have been widely studied, albeit independently. Both density dependent transport and reactive transport are complex physical and chemical processes, and the combination of these two topics is often times not necessary. Density dependent processes typically deal with total dissolved solids or chlorides, both considered conservative solutes, and therefore assumed to be free from reactions. On the other hand, contaminants such as heavy metals and organic compounds undergo equilibrium and kinetic chemical reactions without impacting the density of the solutes. Studying the combined effects of density and reactive transport, however, is needed in specific situations in which coupling is important as density impacts the flow field, flow field impacts mixing and reactions, and reactions impact concentrations that affect density, hence creating a highly non-linear problem. Examples include reactions in brines, precipitation/dissolution in costal aquifers, and geochemistry in saline mixing zones. A separate topic in which contaminants exhibit impacts of density on transport are non-aqueous phase liquids (NAPL). The light-NAPL (LNAPL) and

dense-NAPL (DNAPL) transport processes interact between multiple phases, i.e. water, solids, liquid (water) and an immiscible NAPL phase and are studied as multi-phase transport processes. This study focuses on solute transport processes that consider density dependent reactive transport processes only within the water phase.

Over the last twenty years, there have been limited research publications that have studied density dependent and reactive transport processes in conjunction. Zhang et al (1998) presented a two-dimensional multispecies reactive transport code to simulate flow and transport with kinetic adsorption for variable-density flow. The study simulated transport of bromide (non-reactive) and lithium (reactive) tracer test performed in a sand and gravel aquifer at Cape Cod, Massachusetts. A separation of the two plumes was observed due to slowing of lithium plume due to kinetic adsorption. Freedman and Ibaraki (2002) developed a three-dimensional numerical model that coupled chemical reactions and density-dependent flow and transport. The developed code was called density-dependent and reactive mass transport (DART) model, a combination of a variable density flow and transport model MITSU3D (Ibaraki, 1998), combined with reaction code GIMRT (Steefel and Yabusaki, 1996). Reactions included equilibrium reactions between aqueous species, kinetic reactions between aqueous and solid phases, and full coupling of porosity and permeability changes due to precipitation and dissolution. Freedman and Ibaraki (2002) used a fully coupled, fully implicit, upstream weighted approach to solve density and reactions and presented a series of simulations to examine coupled density and reactions to demonstrate the effect of buoyancy driven flows on instability development and solute transport.

Christensen et al (2002) developed a three-dimensional code PHASTD by coupling a reactive transport code PHREEQC (Parkhurst, 1995) and a heat and solute transport code HST3D (Kipp, 1997). Operator splitting approach was used to solve reactive processes, and

density effects were solved iteratively between flow and multicomponent transport. Christensen et al (2002) developed a three-dimensional flow and biogeochemical transport model for a landfill site, Trandum landfill, in Norway to study the effects of dense leachate plume on secondary redox reactions generated from degradation of organic compounds. The density variation due to changes in mass fraction was described as a linear relation with local density impacted by mineral precipitation and dissolution reactions for each component considered in the simulation. Movement of plume was considered with and without density to study the impacts of considering density with reactions and it was noted that density impacted the distribution of redox species and the redox buffering by iron and manganese hydroxides.

Mao et al (2006) developed a code to simulate density impacts with reactive transport and developed a model to simulate a tank experiment in which saltwater intrusion was accompanied by cation exchange. Density-dependent flow and transport code SEAWAT (Guo and Langevin, 2002; Langevin et al, 2007) and a reactive transport code PHREEQC (Parkhurst, 1995) were combined to create PHWAT. SEAWAT is a combination of a flow simulator MODFLOW (Harbaugh et al. 2000) and solute transport simulator MT3D (Zheng and Wang, 1999). Operator splitting approach was used to solve PHWAT. Experimental data based on a column study from Appelo et al (1990) and Appelo (1994) were used to validate reactive transport. The purpose of the study was to assess the impact of density and reactions on movement of plume. Mao et al (2006) presented governing equations for groundwater flow with variable density, multicomponent transport with reactions, and coupling between flow and transport, and equilibrium and kinetic reactions during transport. Sand tank experiments for the study were provided by Panteleit (2004). Cation exchange was the primary reaction. Unstable plumes were observed in the tank and also simulated. It was concluded from the study that both reactive

transport and density had to be considered in numerical simulation to match observed experimental results.

Post and Prommer (2007) presented a numerical modeling study in which the Elder problem (Elder, 1967) was reformulated with multicomponent reactions. In the adapted Elder problem, the bottom boundary was changed from specified concentration boundary to no-flow boundary to prevent mass from leaving the bottom face via diffusion and the density of salt water at top was set to a lower density representing diluted seawater, while maintaining the Rayleigh number (Ra = 400) of the original Elder problem. This was achieved by changing the value of intrinsic permeability. Maintaining Ra was essential to let free convection occur; otherwise diffusion would dominate the system. Plume speed was maintained by maintaining Ra enabling comparison between simulations (Post and Prommer, 2007). In this study, only cation exchange and calcite equilibrium reactions were considered. The code used by Post and Prommer (2007) was a variable-density version of PHT3D (Prommer et al, 2003) in combination with SEAWAT using an operator split approach. Density calculations accounted for density contribution from individual ions and reactive and non-reactive simulations were performed for a range of densities. The study found that low density and high permeability simulations showed significant change in plume characteristics and the difference decreased with higher density. Post and Prommer (2007) concluded that reactions may not be considered for higher density problem like seawater intrusion with density contrast of 25 $kg/m^3$ (density of 1,025 $kg/m^3$) but reactions may be important to consider for leachate emanating from landfills in which density contrasts are lower, in the order of 0.7 to 1.5 $kg/m^3$ (1,000.7 to 1,001.5 $kg/m^3$). The study stated that no data in field or lab study existed to validate the models and field data and lab studies need to be

conducted to study the range of densities in which reactions together with densities play an important role and that the impact of different chemical reactions needed to be assessed.

Henderson et al (2009) conducted a modeling study to investigate spatial and temporal evolution of permanganate injections at a well characterized field site with DNAPL contamination in Connecticut, US. Density coupled with reactive transport was incorporated in MIN3P code (Mayer et al 2002). Governing equations included variably saturated flow, reactive transport, and permeability-porosity relationships in which decrease in aquifer porosity and permeability due to precipitation of minerals was considered. The numerical implementation included iterative flow and reactive transport with adaptive time-stepping, and explicit coupling option was also presented. Modeling was performed to evaluate the capability of code, assess sensitivity of model to parameters and processes, quantify system mass balance, and demonstrate and quantify the role of density on remediation efficiency. Field observation of spatial and temporal distribution of permanganate were compared to simulated distribution.

This study presents a simulation tool called DRT3D that combines the capabilities of SEAWAT and a reactive transport code RT3D (Clement 1997, 2003). DRT3D is a numerical code capable of simulating the combined effects of density and reactions. The variable-density reactive code was applied to develop a proof of concept for remediation design that takes advantage of density contrast of reactants and contaminated plumes to promote mixing and for solvents to reach less accessible sites contaminated within an aquifer. The following sections discuss the governing equation, code implementation, and code verification in detail.

## 7.2 Governing Equations

SEAWAT is a variable-density flow and transport simulator that couples the flow simulator MODFLOW (Harbaugh et al. 2000) and solute transport simulator MT3D (Zheng and

Wang, 1999). The governing equation for variable-density flow and transport used in SEAWAT is derived in Guo and Langevin (2002). The equation considers the flow equation including variable density that is dependent on the solute concentration. The governing equation used in SEAWAT is shown here (Guo and Langevin, 2002):

$$\frac{\partial}{\partial\alpha}\left(\rho K_{f\alpha}\left(\frac{\partial h_f}{\partial\alpha}+\frac{\rho-\rho_f}{\rho_f}\frac{\partial Z}{\partial\alpha}\right)\right)+\frac{\partial}{\partial\beta}\left(\rho K_{f\beta}\left(\frac{\partial h_f}{\partial\beta}+\frac{\rho-\rho_f}{\rho_f}\frac{\partial Z}{\partial\beta}\right)\right)+\frac{\partial}{\partial\gamma}\left(\rho K_{f\gamma}\left(\frac{\partial h_f}{\partial\gamma}+\frac{\rho-\rho_f}{\rho_f}\frac{\partial Z}{\partial\gamma}\right)\right)=$$
$$\rho S_f\frac{\partial h_f}{\partial t}+\theta E\frac{\partial C}{\partial t}-\rho_s q_s \qquad (7.1)$$

where, α, β, and γ and principal directions for flow that are orthogonal to each other; C is the solute concentration [M/L$^3$]; ρ is the density of saltwater [M/L$^3$] at a given concentration C; $\rho_f$ is the freshwater density (at zero concentration) [M/L$^3$]; $K_f$ is the freshwater hydraulic conductivity [L/T]; $h_f$ is the freshwater head [L]; Z is the elevation [L]; $S_f$ is the specific storage in terms of freshwater head [L$^{-1}$]; θ is the porosity [dimensionless]; E is the slope of the linear relationship between density and concentration, $\frac{\partial\rho}{\partial C}$ [dimensionless]; $\rho_s$ is the source/sink density [M/L$^3$]; and $q_s$ is the volumetric flow rate per unit volume representing sources/sinks [T$^{-1}$]. The term $\frac{\partial C}{\partial t}$ represents the change in concentration over time, which is described by the solute transport equation.

The following solute transport equation is solved by SEAWAT (Guo and Langevin, 2002):

$$\frac{\partial C}{\partial t}=\nabla\cdot(D\cdot\nabla\mathrm{C})-\nabla\cdot(vC)-\frac{q_s C_s}{\theta}+\sum_{k=1}^{N}R_k \qquad (7.2)$$

where, ∇ is the gradient operator $\frac{\partial}{\partial\alpha}+\frac{\partial}{\partial\beta}+\frac{\partial}{\partial\gamma}$; D is the hydrodynamic dispersion coefficient [L$^2$/T]; v is the fluid velocity [L/T]; $C_s$ is the concentration of source/sink [M/L$^3$]; and $R_k$ (k=1,…,N) is the rate of solute change due to production or decay in reaction k of N different reactions [M/(L$^3$T)].

SEAWAT provides an option to solve the flow equation and transport equation explicitly, i.e. flow solution followed by transport solution, or iteratively by solving flow and transport equations within a loop till the heads and concentrations converge within a numerical tolerance.

The left-hand-side term of equation 7.2 represents the change in concentration over time. The first term on the right-hand-side is the dispersion term, the second term represents the advection term, the third term represents sources/sinks; and the last term represents all possible reactions. The last term is of interest in this study. The reactions represented within SEAWAT were extended by incorporating RT3D reaction modules within SEAWAT. The implementation of RT3D modules is described in the next section.

## 7.3 Implementation

For DRT3D, RT3D reaction modules were integrated within the SEAWAT code. RT3D modules were implemented as a new package in SEAWAT, called RT3D-Reaction (RTR) package. To invoke RT3D reactions in DRT3D, the RTR package needs to be activated. With the RTR package active, all reaction modules of RT3D become available for use with the variable-density reactive code DRT3D.

In DRT3D, RT3D reactions are solved using the operator split approach. This is the same approach used by RT3D for the reactive transport simulations. With the operator split approach the following steps are performed sequentially to solve variable-density reactive transport with DRT3D for every time-step:

1. Flow and transport equations are formulated and solved using the SEAWAT code until convergence is achieved.

2. At the end of the flow and transport solution, reaction terms are assembled for each model cell forming an ordinary differential equation and solved to update concentrations.
3. Model budgets are calculated and reported. An additional budget term for reactions is included in the mass balance summary in the main output file.

## 7.4 Verification Examples

A synthetic numerical model was created to verify the development of DRT3D code. Figure 7.1 shows a schematic of the numerical model. The synthetic model was a cross-sectional two-dimensional rectangular domain 1,000 m in length and 100 m deep. Prescribed head was assigned as the left and the right boundary with a value of 110.5 m and 110 m, respectively. Recharge boundary at a rate of 0.0007 m/day was assigned as the top boundary to create vertical flow gradients to allow plumes to sink as the plumes are transported from left to right. Two solutes were released at the top. The first solute was released from 90 m to 200 m from the left boundary and the second solute was released from 290 m to 360 m from the left boundary. Both solutes were released with a concentration of 100 concentration units. The numerical model was discretized into 10 m × 10 m model cells. Flow was simulated as steady-state and transport model was simulated as a transient simulation for 25,000 days. Hydraulic conductivity for the system was set to 10 m/day and porosity was set to 0.1.

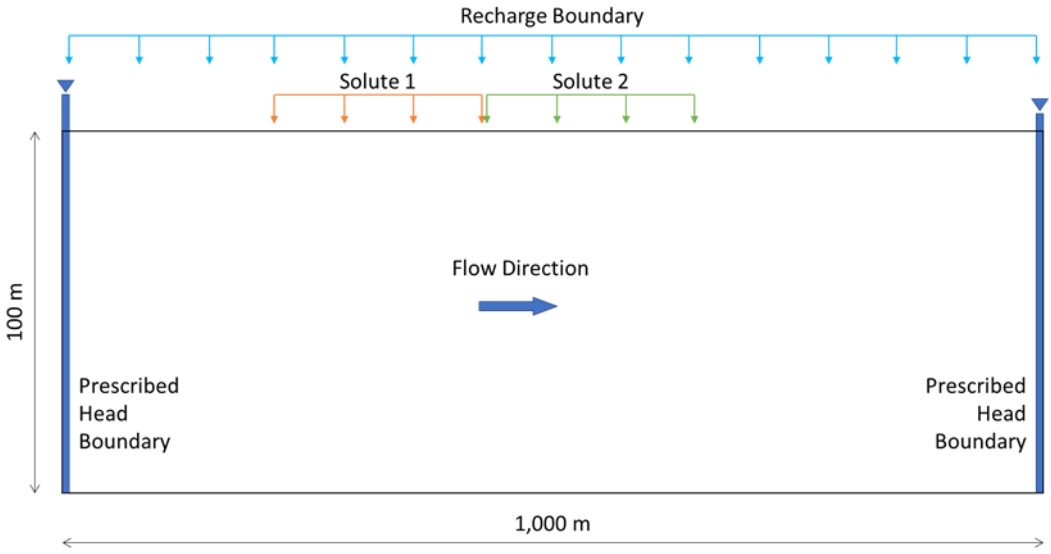


Figure 7.1 – Schematic showing key features of the numerical model used for preliminary DRT3D verification

The following simulations were performed for verification of the DRT3D code:

1. RT3D code – no reaction (essentially an MT3D simulation);
2. RT3D code – with reaction;
3. DRT3D code – no reaction, no density effects (to compare to the first model);
4. DRT3D code – with reaction, no density effects (to compare to the second model);
5. DRT3D code – with reaction, with density effects using $\partial\rho/\partial C$ = 0.1; and
6. DRT3D code – with reaction, with density effects using $\partial\rho/\partial C$ = 0.2.

The reaction considered in these simulations utilizes Module 5 of the RT3D code, which represents a double Monod model. The reaction module simulates the reaction between an elector donor and an electron acceptor mediated by actively growing bacteria cells living in both aqueous and soil phases (Clement, 1997). The term $R_k$ in equation 7.2 is defined by the equations as shown below.

Reaction for the electron donor is described by the following equation (Clement, 1997):

$$\frac{d[D]}{dt} = -\frac{\mu_m}{R_D}\left([X] + \frac{\rho_b \tilde{X}}{\theta}\right)\left(\frac{[D]}{K_D+[D]}\right)\left(\frac{[A]}{K_A+[A]}\right) \quad (7.3)$$

where, [D] is the electron donor concentration in the aqueous phase [M/L$^3$]; $\mu_m$ is the maximum specific growth rate of bacteria [1/T]; $R_D$ is the retardation coefficient of the electron donor [dimensionless]; [X] is the aqueous phase bacterial cell concentration [M/L$^3$]; $\rho_b$ is the bulk density of the soil matrix [M/L$^3$]; $\tilde{X}$ is the solid phase bacterial concentration [M/M]; $K_D$ is the half saturation constant for the electron donor [M/L$^3$]; [A] is the electron acceptor concentration in the aqueous phase [M/L$^3$]; and $K_A$ is the half saturation constant for the electron acceptor [M/L$^3$]. Reaction for the electron acceptor is given as follows (Clement, 1997):

$$\frac{d[A]}{dt} = -\frac{Y_{A/D}\mu_m}{R_A}\left([X] + \frac{\rho_b \tilde{X}}{\theta}\right)\left(\frac{[D]}{K_D+[D]}\right)\left(\frac{[A]}{K_A+[A]}\right) \quad (7.4)$$

where, $Y_{A/D}$ is the stoichiometric yield coefficient between the electron acceptor and electron donor [dimensionless]; and $R_A$ is the retardation coefficient of the electron acceptor [dimensionless]. The equation for the bacterial concentration in the aqueous phase is shown below (Clement, 1997):

$$\frac{d[X]}{dt} = -Y_{X/D}\mu_m\left([X] + \frac{\rho_b \tilde{X}}{\theta}\right)\left(\frac{[D]}{K_D+[D]}\right)\left(\frac{[A]}{K_A+[A]}\right) + \frac{K_{det}\rho_b \tilde{X}}{\theta} - K_{att}[X] - K_e[X] \quad (7.5)$$

where, $Y_{X/D}$ is the stoichiometric yield coefficient between the bacterial cells and electron donor [dimensionless]; $K_{det}$ is the bacterial detachment coefficient [1/T]; $K_{att}$ is the bacterial attachment coefficient [1/T]; and $K_e$ is the endogenous cell death rate [1/T]. The growth of the adsorbed bacterial concentration is given by the following equation (Clement, 1997):

$$\frac{d\tilde{X}}{dt} = \frac{K_{att}\theta[X]}{\rho_b} - K_{det}\tilde{X} + Y_{X/D}\mu_m\tilde{X}\left(\frac{[D]}{K_D+[D]}\right)\left(\frac{[A]}{K_A+[A]}\right) - K_e\tilde{X} \quad (7.6)$$

The electron donor, electron acceptor, bacterial cell concentration in the aqueous phase, and the bacterial concentration in the adsorbed phase are represented in the numerical DRT3D model as four solutes. The adsorbed phase concentration is represented as an immobile solute.

This first simulation was essentially an MT3D simulation. The two solute plumes were expected to travel without interfering with each other despite an overlap between the two plumes. An overlap between the two plumes is observed but the two plumes coexist in absence of any reactions. This simulation was created as a base case against which the subsequent simulations can be compared. Figure 7.2 shows the results from the first simulation.

The second simulation comprised of a reaction between the two solutes. The reaction in this example was Module 5 of RT3D, which is a double Monod model. Figure 7.3 shows the results for Simulation 2, run with RT3D with reaction. As seen in Figure 7.3, the extents of both solute plumes are attenuated because of reactions between the two plumes.

The next two simulations, Simulations 3 and 4 were performed using the new code DRT3D. These simulations are akin to the first two simulations that were simulated using RT3D. The main purpose of Simulations 3 and 4 was to ascertain that reactions were correctly implemented in DRT3D. Figures 7.4 and 7.5 show the results for Simulations 3 and 4, respectively. As seen in Figure 7.4, results for two conservative tracers show good agreement with Simulation 1 results. Both Simulation 1 (Figure 7.2) and Simulation 3 (Figure 7.4) model two conservative tracers and are essentially MT3D simulations. Simulation 2 (Figure 7.3) and Simulation 4 (Figure 7.5) both represent a double Monod model and produce similar plume distributions. This result demonstrates that the reaction module implemented in DRT3D is consistent with RT3D.

The next two simulations were performed to assess the impact of density on mixing and reactions between the two plumes. Solute 1 was simulated with freshwater density, which would not impact the plume movement, and Solute 2 was given a higher density which will promote the solute 2 plume to sink deeper. For Simulation 5 a value of 0.1 was assigned to the term E of equation 7.1, which defines the slope that represents the change in density with change in concentration ($\partial\rho/\partial C$). For Simulation 6, term E was assigned a value of 0.2.

Figures 7.6 and 7.7 show the results for Simulations 5 and 6, that consider reaction between the two plumes and consider a denser second solute that enhances sinking and mixing of the two plumes. Several important features are noted for Simulations 5 and 6. The sinking of the second solute creates instabilities in the system that are typical of sinking denser plumes resulting in an oscillating plume. Because of its density, the second plume sinks more, relative to the first (upstream) plume and enhances mixing. Mixing of the two plumes creates more contact between the two plumes which enhances reaction between the two plumes. Because of reaction, the leading edge of the first plume shows reduced concentration relative to previous simulations. Solute two is predominantly only seen near the source of the second solute as much of the transported concentration is consumed as it is involved in reactions with the first plume. As expected, a value for term E ($\partial\rho/\partial C$) shows less sinking in Figure 7.6 and higher slope between density and concentration shows more sinking, and hence smaller concentrations, in Figure 7.7.

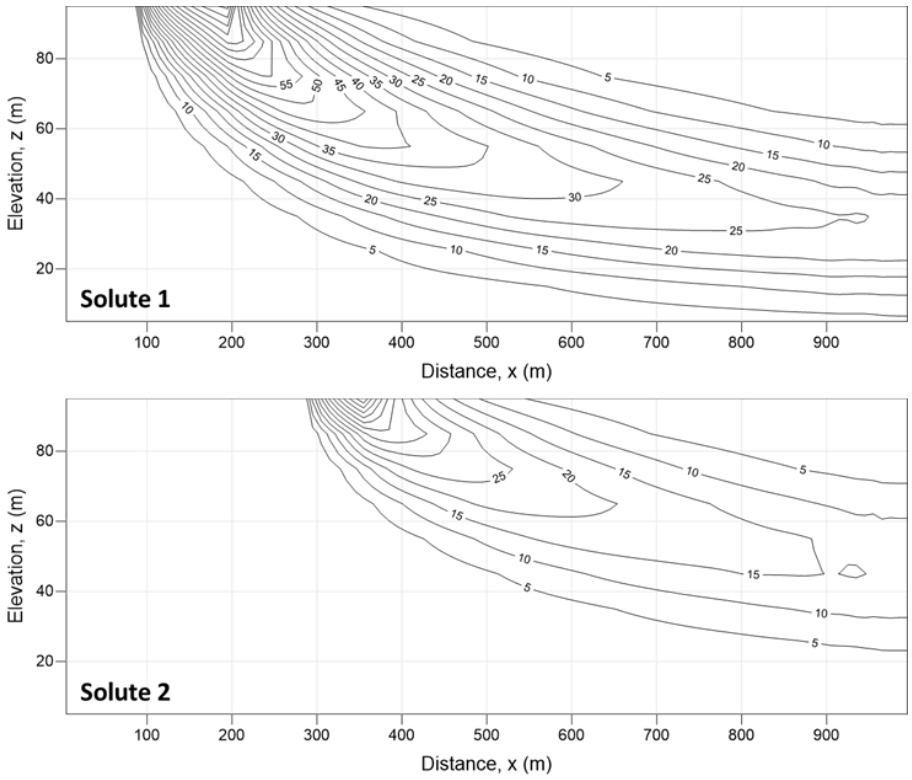


Figure 7.2 – Plumes for solute 1 and solute 2 for Simulation 1 – RT3D code without reaction.

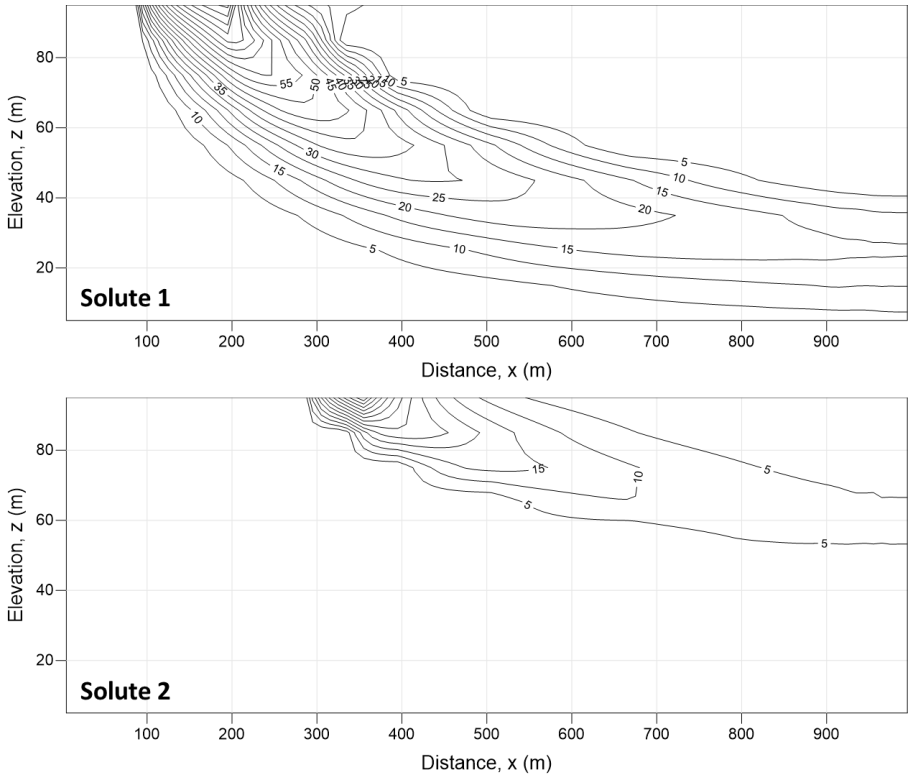


Figure 7.3 – Plumes of solute 1 and solute 2 reacting with each other for Simulation 2 run with RT3D.

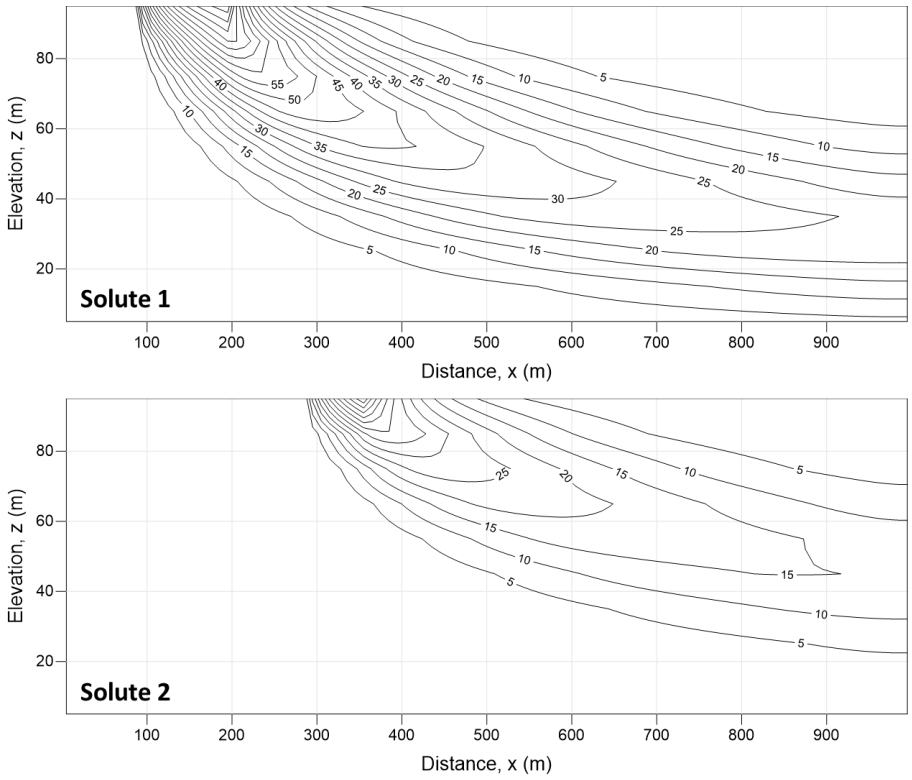


Figure 7.4 – Plumes for solute 1 and solute 2, conservative tracers simulated with DRT3D (Simulation 3).

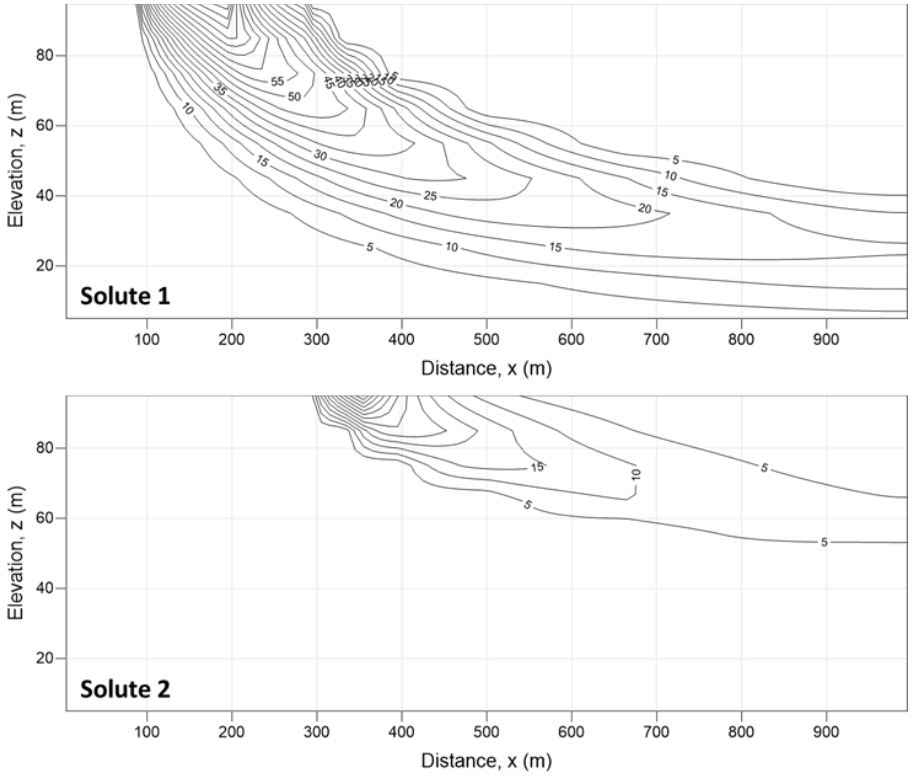


Figure 7.5 – Plumes for solute 1 and solute 2 for Simulation 4 run for reactive transport using DRT3D.

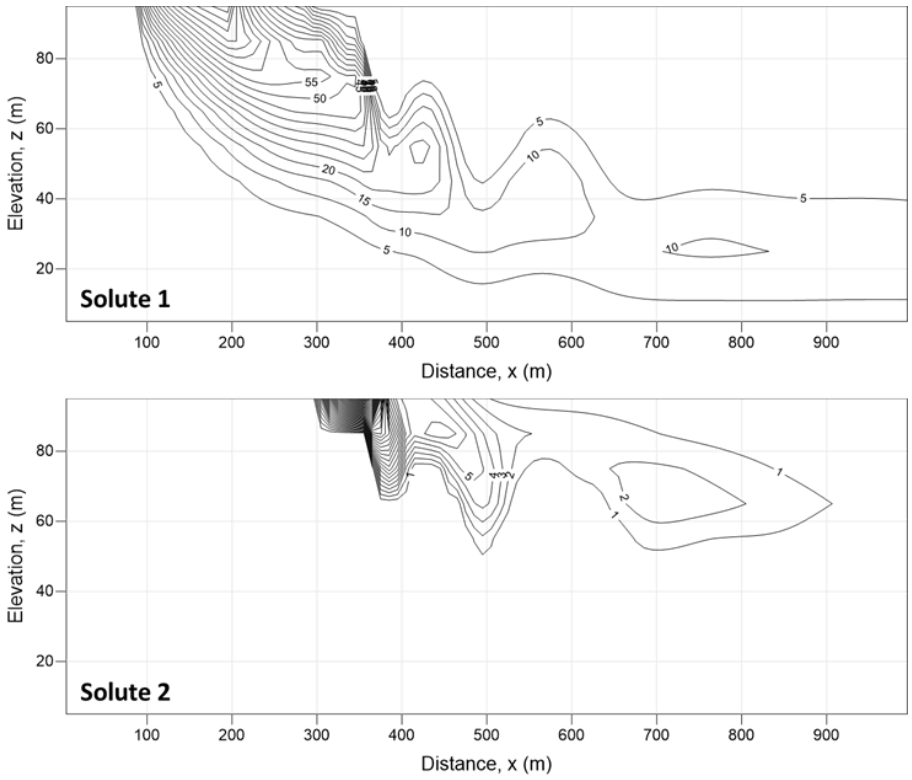


Figure 7.6 – DRT3D Simulation 5 results with reaction and density for solute 2, with $\partial\rho/\partial C = 0.1$.

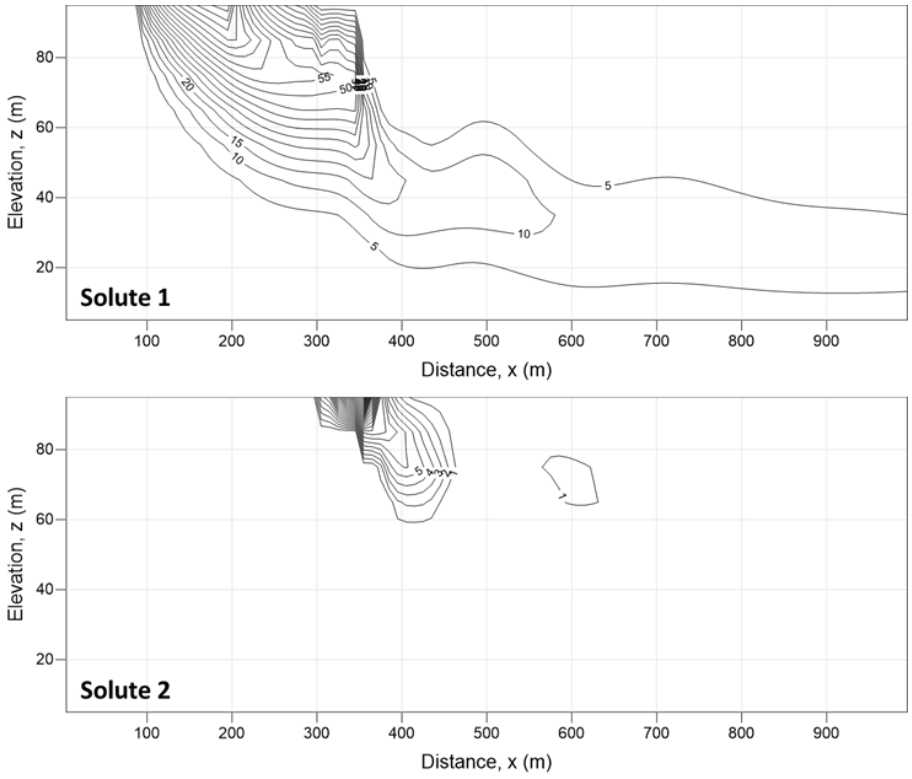


Figure 7.7 – DRT3D Simulation 6 results with reaction and density for solute 2, with $\partial\rho/\partial C = 0.2$.

## 7.5 Conclusions

A new DRT3D simulation code was developed by integrating RT3D and SEAWAT. The DRT3D simulator is capable for simulating multi-species reactions coupled with variable-density flow and transport. The implementation in DRT3D is based on the operator splitting approach to sequentially simulate reactions followed by flow and transport solutions. A verification example was presented to demonstrate the functionality of the newly developed DRT3D code. It was confirmed that the reaction modules of RT3D have been correctly implemented in the DRT3D code. Results for the simulation of reactions in combination with variable-density flow demonstrates that mixing and enhanced reactions were observed in the verification problems. These results, however, need further verification tests to validate DRT3D results.

# Chapter 8 – Conclusions

The key conclusions of this dissertation effort can be summarized as follows:

1. An updated version of MT3D, MT3D-USGS was developed that is capable of simulating solute transport in the lakes and streams, above-ground pump and treat systems with a contaminant treatment system package, multi-species kinetic reactions, and handling transport within dry model cells. The new code improves the storage-term formulation for the finite-difference approximation. The details of the new code are summarized in a peer-reviewed USGS report (Bedekar et al, 2016a).
2. A practical solution was provided to mitigate any erroneous concentrations in the solute transport solution resulting from local flow balance errors of a flow model. The proposed approach was published in Panday, Bedekar, Langevin (2017a).
3. A new methodology was developed to simulate axisymmetric models using the unstructured grid capability offered by MODFLOW-USG. A summary of this effort is published in Bedekar et al (2019a).
4. A numerical modeling study was conducted to examine the impact of lake formation on low-lying islands with dry climates. The study demonstrated that on islands with negative water budgets, i.e. where evapotranspiration exceeds precipitation, lake inundation can cause more than twice the loss of fresh groundwater resources relative to an equivalent amount of coastal inundation. The study is published in Gulley et al (2016).
5. A study comprising of a laboratory-scale sand tank experiments, numerical modeling of the sand tank, and numerical modeling of a real-world scenario showed that natural systems exhibit an efficient non-linear feedback mechanism where the groundwater

system loses water slowly during a dry cycle, but it can recover fast by gaining water rather rapidly during a wet cycle. This non-linear feedback mechanism and its implication on faster freshwater recovery greatly emphasizes the importance of implementing careful recharge management strategies to maximize groundwater recharge for freshwater storage in small island aquifers. This effort is published in Bedekar et al (2019b).

6. A new numerical code, DRT3D, was developed by implementing reactive simulation capabilities of RT3D into the density-dependent code SEAWAT. The impetus for creating DRT3D code was to provide a simulation tool for designing and analyzing density enhanced mixing and reactions for improving the performance of in-situ remediation at contaminated sites.

## 8.1 Recommendations for Future Work

Although this dissertation presents some new developments and a few new findings, the work presented here is nothing but a speck in the vast field of solute transport modeling in porous media systems. Lot more needs to be done. In particular, the research presented here could be advanced in the following possible ways:

1. Perform laboratory-scale experiments to provide benchmark data for the DRT3D code.
2. Perform laboratory-scale experiments to analyze plume diving based on horizontal velocity and plume density as a way to examine and control the mixing processes of denser plumes.
3. Several enhancements to the MODFLOW-family of codes are needed:
    a. Add transport capability in surface water components of MODFLOW-USG and MODFLOW 6.

b. Add reactive transport capabilities in MODFLOW-USG and MODFLOW 6.

c. Incorporate land use and water supply components into MODFLOW-USG and MODFLOW 6.

d. Add reaction capability within surface water transport of MT3D-USGS.

e. Add a module to simulate heat transport using MT3D-USGS.

f. Add capability in SEAWAT to incorporate lakes with variable-density simulations.

## References


Abarca, E., and T.P. Clement. 2009. A novel approach for characterizing the mixing zone of a saltwater wedge: Geophysical Research Letters 36, no. 6.

Abdoulhalik, A., and A.A. Ahmed. 2018. Transience of seawater intrusion and retreat in response to incremental water level variations: Hydrological Processes 32, no. 17: 2721-2733.

Anderson, M. 1976. Unsteady groundwater flow beneath strip oceanic islands: Water Resources Research 12, no. 4: 640-644.

Appelo, C.A.J., 1994. Cation and proton exchange, pH variations, and carbonate reactions in a freshening aquifer. Water Resources Research 30 (10), 2793–2805.

Appelo, C.A.J., Willemsen, A., Beekman, H.E., Griffioen, J., 1990. Geochemical calculations and observations on salt water intrusions, 2, validation of a geochemical model with column experiments. Journal of Hydrology 120 (1–4), 225–250.

Ayers, J. F., and H. Vacher (1986), Hydrogeology of an atoll island: A conceptual model from detailed study of a Micronesian example, Ground Water, 24(2), 185–198.

Bear, J., 1979. Hydraulics of Groundwater, McGraw-Hill, New York, 569 pp.

Bedekar, V., Scantlebury, L. and Panday, S. (2019a), Axisymmetric Modeling Using MODFLOW-USG. Groundwater. doi:10.1111/gwat.12861

Bedekar, V., Memari, S.S., Clement, T.P., 2019b. Investigation of Transient Freshwater Storage in Island Aquifers. Journal of Contaminant Hydrology. Vol. 221, February 2019, p. 98-107. https://doi.org/10.1016/j.jconhyd.2019.02.004

Bedekar, V., Clement, P.T., Memari, S.S., 2018. Understanding Transient Changes in Freshwater Lens Volumes in Island Aquifers. Poster presentation at the American Geophysical Union Fall Meeting 2018, Abstract # H13L-1910.

Bedekar, V., Morway, E.D., Langevin, C.D., and Tonkin, M., 2016a, MT3D-USGS version 1: A U.S. Geological Survey release of MT3DMS updated with new and expanded transport capabilities for use with MODFLOW: U.S. Geological Survey Techniques and Methods 6-A53, 69 p., http://dx.doi.org/10.3133/tm6A53

Bedekar, V., Morway, E.D., Langevin, C.D., and Tonkin, M., 2016b, MT3D-USGS version 1.0.0: Groundwater Solute Transport Simulator for MODFLOW: U.S. Geological Survey Software Release, 30 September 2016, http://dx.doi.org/10.5066/F75T3HKD

Bedekar, V., E. Morway, C. Langevin, and M. Tonkin, 2015. New and Expanded Transport Capabilities of MT3D-USGS. Presentation at MODFLOW and More 2015, May 31–June 3, Golden, CO.

Bessinger, B., V. Bedekar, M. Truex, and M. Tonkin, 2015. Simulation of a Co-Precipitated Chromate-Calcite at a Large Waste Site. Presentation at MODFLOW and More 2015, May 31–June 3, Golden, CO.

Bedekar, V., T.P. Clement, and J. Vasconcelos, 2013. Stability and Accuracy of Implicit and Explicit Linear and Non-linear Schemes. Presentation at MODFLOW and More 2013, June 2-5, Golden, CO.

Bedekar, V., E. Morway, C. Tana, C. Langevin, T. Rooze, and M. Tonkin, 2013. Enhancing MT3DMS for Simulating Solute Transport in a Coupled Groundwater/Surface-water System. Presentation at MODFLOW and More 2013, June 2-5, Golden, CO.

Bedekar, V., R.G. Niswonger, K. Kipp, S. Panday, and M. Tonkin, 2012a. Approaches to the Simulation of Unconfined Flow and Perched Groundwater Flow in MODFLOW. Ground Water, v. 50, pp. 187–198. doi: 10.1111/j.1745-6584.2011.00829.x

Bedekar, V., M. Tonkin, and A. Spiliotopoulos, 2011. Implementation of a Contaminant Treatment System (CTS) Module in MT3DMS. Presentation at MODFLOW and More 2011, June 5-8, Golden, CO.

Bedekar, V., and M. Tonkin, 2011. The Dry Cell Problem: Simulation of Solute Transport with MT3DMS. Presentation at MODFLOW and More 2011, June 5-8, Golden, CO.

Cant, R. V., and P. S. Weech (1986), A review of the factors affecting the development of Ghyben-Hertzberg lenses in the Bahamas, J. Hydrol., 84(3–4), 333–343, doi:10.1016/0022-1694(86)90131-9.

Chang, S.W., K. Nemec, L. Kalin, and T.P. Clement. 2016. Impacts of climate change and urbanization on groundwater resources in a barrier island: Journal of Environmental Engineering 142, no. 12.

Chang, S.W., and T.P. Clement. 2013. Laboratory and numerical investigation of transport processes occurring above and within a saltwater wedge: Journal of contaminant hydrology 147: 14-24.

Chang, S. W., and T. P. Clement (2012), Experimental and numerical investigation of saltwater intrusion dynamics in flux-controlled groundwater systems, Water Resour. Res., 48, W09527, doi:10.1029/2012WR012134.

Chang, S.W., T.P. Clement, M.J. Simpson, and K.K. Lee. 2011. Does sea-level rise have an impact on saltwater intrusion?: Advances in Water Resources 34, no. 10: 1283-1291.

Christensen, F.D., Basberg, L. and Engesgaard, P., "Modeling transport and biogeochemical processes in dense landfill leachate plumes," In: Computational Methods in Water Resources; Proceedings of the XIVth International Conference, Delft, Netherlands, June 23-28, 2002.

Clement, T.P. 2014. Authorship matrix: a rational approach to quantify individual contributions and responsibilities in multi-author scientific articles: Science and Engineering Ethics 20, no. 2: 345-361.

Custodio, E., and G.A. Bruggeman. 1987. Groundwater problems in coastal areas. Studies and reports in hydrology 45.

Clement, T.P. 2003. RT3D v2.5 Updates to User's Guide. Richland, Washington: Pacific Northwest National Laboratory.

Clement, T.P, 1997, RT3D - A modular computer code for simulating reactive multi-species transport in 3-Dimensional groundwater aquifers, Battelle Pacific Northwest National Laboratory Research Report, PNNL-SA-28967, September 1997. Available at: http://bioprocess.pnl.gov/rt3d.htm.

Dasgupta, S., B. Laplante, C. M. Meisner, D. Wheeler, and J. Y. Yan (2009), The impact of sea level rise on developing counties: A comparative analysis, Clim. Change, 93(3–4), 379–388.

DeConto, R. M., and D. Pollard (2016), Contribution of Antarctica to past and future sea-level rise, Nature, 531(7596), 591–597.

DHI, 2004. MIKE SHE: An Integrated Hydrological Modeling System. Danish Hydraulic Institute, Hørsholm, Denmark.

Díaz Arenas, A., and J. Febrillet Huertas. 1986. Hydrology and water balance of small islands: a review of existing knowledge. In Technical documents in hydrology: UNESCO.

Diersch, H.J.G. 2002. FEFLOW Finite Element Subsurface Flow and Transport Simulation System—User's Manual/Reference Manual/White Papers. Release 5.0. Berlin, Germany: WASY Ltd.

Diersch, H-J.G., 2002, About the difference between the convective form and the divergence form of the transport equation. FEFLOW White Papers – Vol. I, WASY Ltd, Berlin.

Diersch, H-J.G. 2005, FEFLOW Reference Manual. WASY Software: 292p.

Dose, E.J., L. Stoeckl, G.J. Houben, H. Vacher, S. Vassolo, J. Dietrich, and T. Himmelsbach. 2014. Experiments and modeling of freshwater lenses in layered aquifers: steady state interface geometry: Journal of hydrology 509: 621-630.

Duncan, D. 2011. Freshwater Under Threat/Pacific Islands: United Nations Environment Programme, Bankok.

Elder, J. W. (1967), Transient convection in a porous medium, J. Fluid Mech., 27, 609– 623.

Falkland, A.C. 1992. Small Tropical islands: Water resources of paradise last. In IHP Humid Tropics Programme series: Unesco.

Falkland, A.C., and E. Custodio. 1991. Hydrology and water resources of small islands: A practical guide: Unesco.

Fetter Jr., C. W. (1972), Position of the saline water interface beneath oceanic islands, Water Resources Research, 8(5), 1307–1315, doi:10.1029/WR008i005p01307.

Freedman, V., Ibaraki, M., 2002. Effects of chemical reactions on density-dependent fluid flow: on the numerical formulation and the development of instabilities, Advances in Water Resources 25, 439–453.

Goode, D.J., 1992, Modeling transport in transient ground-water flow: An unacknowledged approximation: Ground Water, v. 30, no. 2, p. 257-261.

Goswami, R.R., and T.P. Clement. 2007. Laboratory-scale investigation of saltwater intrusion dynamics. Water Resources Research.

Gulley, J., A. Mayer, J. Martin, and V. Bedekar. 2016. Sea level rise and inundation of island interiors: Assessing impacts of lake formation and evaporation on water resources in arid climates: Geophysical Research Letters 43, no. 18: 9712-9719 doi:10.1002/2016GL070667.

Gulley, J. D., J. B. Martin, P. Spellman, P. J. Moore, and E. J. Screaton (2014), Influence of partial confinement and Holocene river formation on groundwater flow and dissolution in the Florida carbonate platform, Hydrol. Process., 28(3), 705–717, doi:10.1002/hyp.9601.

Guo, W., and C. D. Langevin (2002), User's guide to SEAWAT: A computer program for simulation of three-dimensional variable-density ground water flow, U.S. Geol. Surv. Open File Rep., 01–434, 77pp.

Harbaugh A.W., 2005. MODFLOW-2005, the U.S. Geological Survey modular ground-water model -- the Ground-Water Flow Process: U.S. Geological Survey Techniques and Methods 6-A16.

Harbaugh, A.W., Banta, E.R., Hill, M.C., and McDonald, M.G., 2000, MODFLOW-2000, the U.S. Geological Survey modular ground-water model -- User guide to modularization concepts and the Ground-Water Flow Process: U.S. Geological Survey Open-File Report 00-92, 121 p.

Healy, R.W., 1990, Simulation of solute transport in variably saturated porous media with supplemental information on modifications to the U.S. Geological Survey's Computer Program VS2D: U.S. Geological Survey Water-Resources Investigations Report 90-4025, 125 p.

Henry, H.R. 1960. Salt intrusion into coastal aquifers. Columbia University, New York.

Henderson, T.H., Mayer, K.U., Parker, B.L. and Al, T.A. 2009. Three-Dimensional Density-Dependent Flow and Multicomponent Reactive Transport Modeling of Chlorinated Solvent Oxidation by Potassium Permanganate. Journal of Contaminant Hydrology, 106: 195-211.

Henry, H.R. 1964. Effects of dispersion on salt encroachment in coastal aquifers. U.S. Geological Survey Water-Supply Paper. 1613-C.

Holding, S., and D. M. Allen (2015), From days to decades: Numerical modelling of freshwater lens response to climate change stressors on small low-lying islands, Hydrol. Earth Syst. Sci., 19(2), 933–949, doi:10.5194/hess-19-933-2015.

Houben, G.J., L. Stoeckl, K.E. Mariner, and A.S. Choudhury. 2018. The influence of heterogeneity on coastal groundwater flow-physical and numerical modeling of fringing reefs, dykes and structured conductivity fields: Advances in Water Resources 113: 155-166.

HydroGeoLogic (HGL), 2011. MODHMS/MODFLOW-SURFACT: A Comprehensive MODFLOW-based Hydrologic Modeling System, HydroGeoLogic, Reston, VA.

HydroGeoLogic, 1998. MODFLOW-SURFACT v. 3.0: A comprehensive MODFLOW-based flow and transport simulator. Code Documentation Report. HydroGeoLogic, Reston, VA.

Huyakorn, P., and G. Pinder, 1983, Computational Methods in Subsurface Flow, Academic, San Diego, California, 473 pp.

Ibaraki M., A robust and efficient numerical model for analyses of density-dependent flow in porous media. J Contam Hydrol 1998; 34:235–46.

Jocson, J. M. U., J. W. Jenson, and D. N. Contractor (2002), Recharge and aquifer response: Northern Guam lens aquifer, Guam, Mariana Islands, J. Hydrol., 260, 231–254, doi:10.1016/S0022-1694(01)00617-5.

Ketabchi, H., D. Mahmoodzadeh, B. Ataie-Ashtiani, A. D. Werner, and C. T. Simmons (2014), Sea-level rise impact on fresh groundwater lenses in two-layer small islands, Hydrol. Process., 28(24), 5938–5953, doi:10.1002/hyp.10059.

Kipp, K.L., 1997, Guide to the Revised Heat and Solute Transport Simulator: HST3D -- Version 2: U.S. Geological Survey Water-Resources Investigations Report 97-4157, 149 p.

Langevin, C.D., Hughes, J.D., Banta, E.R., Niswonger, R.G., Panday, Sorab, and Provost, A.M., 2017, Documentation for the MODFLOW 6 Groundwater Flow Model: U.S. Geological Survey Techniques and Methods, book 6, chap. A55, 197 p., https://doi.org/10.3133/tm6A55.

Langevin, C. D. (2008), Modeling Axisymmetric Flow and Transport. Groundwater, 46: 579-590. doi:10.1111/j.1745-6584.2008.00445.x.

Langevin, C.D., Thorne, D.T., Jr., Dausman, A.M., Sukop, M.C., and Guo, Weixing, 2007, SEAWAT Version 4: A Computer Program for Simulation of Multi-Species Solute and Heat Transport: U.S. Geological Survey Techniques and Methods Book 6, Chapter A22, 39 p.

Louwyck, A., Vandenbohede, A., Bakker, M., & Lebbe, L. (2014). MODFLOW procedure to simulate axisymmetric flow in radially heterogeneous and layered aquifer systems. HYDROGEOLOGY JOURNAL, 22(5), 1217–1226.

Lu, C., and A.D. Werner. 2013. Timescales of seawater intrusion and retreat: Advances in Water Resources 59: 39-51.

Lu, G., T.P. Clement, C. Zheng, and T.H. Wiedemeier. 1999. "Natural Attenuation of BTEX Compounds: Model Development and Field-Scale Application." Ground Water, 37(5):707-717.

Mansour, M M, Hughes, A G, and Spink, A E F. 2007. User manual for the layered R-theta numerical model. British Geological Survey, 58pp. (OR/07/029)

Mao, X., H. Prommer, D. A. Barry, C. D. Langevin, B. Panteleit, and L. Li (2006), Three-dimensional model for multi-component reactive transport with variable density groundwater flow, Environ. Modell. Software, 21, 615–628.

Martin, J., and J. Gulley (2010), Distribution of fresh water on Rum Cay and implications for generation of secondary porosity, in Proceedings of the 14th Symposium on the Geology of the Bahamas and Other Carbonate Regions, edited by F. Siewers and J. Martin, pp. 140–149, Gerace Research Centre, San Salvador, Bahamas.

Masterson, J. P., M. N. Fienen, E. R. Thieler, D. B. Gesch, B. T. Gutierrez, and N. G. Plant (2013), Effects of sea-level rise on barrier island groundwater system dynamics–ecohydrological implications, Ecohydrology, doi:10.1002/eco.1442.

Mayer, K.U., Frind, E.O., Blowes, D.W., 2002. Multicomponent reactive transport modeling in variably saturated porous media using a generalized formulation for kinetically controlled reactions. Water Resour. Res. 38, 1174. doi:10:1029/2001WR000862.

Maxwell, R.M., S.J. Kollet, S.G. Smith, C.S. Woodward, R.D. Falgout, C. Baldwin, W.J. Bosl, R. Hornung, S. Ashby, ParFlow User's Manual. International Ground Water Modeling Center Report GWMI 2009-01, 129p.

McDonald, M.G., and Harbaugh, A.W., 1988, A modular three-dimensional finite-difference ground-water flow model: U.S. Geological Survey Techniques of Water-Resources Investigations, book 6, chap. A1, 586 p.

Michael, H. A., C. J. Russoniello, and L. A. Byron (2013), Global assessment of vulnerability to sea-level rise in topography-limited and recharge-limited coastal groundwater systems, Water Resour. Res., 49, 2228–2240, doi:10.1002/wrcr.20213.

Michael, H.A., A.E. Mulligan, and C.F. Harvey. 2005. Seasonal oscillations in water exchange between aquifers and the coastal ocean: Nature 436, no. 7054: 1145-1148.

Monod, J., 1949, The growth of bacterial cultures: Annual Reviews in Microbiology, v. 3, p. 371–394.

Morway, E., V. Bedekar, C. Langevin, M. Tonkin, R.G. Niswonger, 2015. Demonstration of Enhanced Groundwater Solute Transport Capabilities in MT3D-USGS. Presentation at MODFLOW and More 2015, May 31–June 3, Golden, CO.

Morway, E., V. Bedekar, and C. Langevin, 2014. Recent Enhancements to MT3DMS for Simulation of Solute Exchange in Hydraulically Connected Stream-Aquifer Systems. Presentation at the 2014 National Ground Water Association (NGWA) Ground Water Summit, Denver, CO, May 5-7.

Morway, E. D., Niswonger, R. G., Langevin, C. D., Bailey, R. T. and Healy, R. W. (2013), Modeling Variably Saturated Subsurface Solute Transport with MODFLOW-UZF and MT3DMS. Groundwater, 51: 237–251. doi: 10.1111/j.1745-6584.2012.00971.x

Neuman, S.P., 1974. Effect of partial penetration on flow in unconfined aquifers considering delayed gravity response, Water Resources Research, vol. 10, no. 2, pp. 303-312.

Neville, C.J., 2014: ATRANS: Analytical Solutions for Three-Dimensional Solute Transport from a Patch Source, Version 1.08, S.S. Papadopulos & Associates, Inc., Waterloo, Ontario. Available at http://www.sspa.com/software/atrans

Niswonger, R.G., Panday, Sorab, and Ibaraki, Motomu, 2011, MODFLOW-NWT, A Newton formulation for MODFLOW-2005: U.S. Geological Survey Techniques and Methods 6-A37, 44 p.

Niswonger, R. G., D. E. Prudic, et al. (2006). Documentation of the Unsaturated-Zone Flow (UZF1) Package for modeling unsaturated flow between the land surface and the water table with MODFLOW-2005, U. S. Geological Survey Techniques and Methods 6-A19, 62 pg.

Nurse, L. A., R. F. McLean, J. Agard, L. P. Briguglio, V. Duvat-Magnan, N. Pelesikoti, E. Tompkins, and A. Webb (2014), Small islands, in Climate Change 2014: Impacts, Adaptation and Vulnerability. Contribution of Working Group II to the Fifth Assessment Report of the Intergovernmental Panel on Climate Change, edited by V. R. Barros et al., pp. 1655–1713, Cambridge Univ. Press, Cambridge, U. K., and New York.

Panday, S., Bedekar, V. and Langevin, C. D. (2017a), Impact of Local Groundwater Flow Model Errors on Transport and a Practical Solution for the Issue. Groundwater. doi:10.1111/gwat.12627

Panday, S., Langevin, C., Provost, A., Bedekar, V., 2017b. A Hydraulic Head Formulation for Density Dependent Flow and Transport. Presentation at MODFLOW and More 2017, May 21-24, Golden, CO.

Panday, Sorab, Langevin, C.D., Niswonger, R.G., Ibaraki, Motomu, and Hughes, J.D., 2017, MODFLOW-USG version 1.4.00: An unstructured grid version of MODFLOW for simulating groundwater flow and tightly coupled processes using a control volume finite-difference formulation: U.S. Geological Survey Software Release, 27 October 2017, https://dx.doi.org/10.5066/F7R20ZFJ

Panday, S., 2017. Block-Centered Transport (BCT) Process for MODFLOW-USG. GSI Environmental, 17 Oct. 2017. https://gsi-net.com/en/software/free-software/modflow-usg.html

Panday, S., and P.S. Huyakorn. 2008. MODFLOW-SURFACT: A state-of-the-art use of vadose zone flow and transport equations and numerical techniques for environmental evaluations. Vadose Zone J. 7:610–631

Panteleit, B., 2004. Geochemical Processes in the Salt–Freshwater Transition Zone, Reports of the Department of Earth Sciences, University Bremen, Nr. 225: Bremen, Germany.

Parkhurst, D.L. 1995. User's guide to PHREEQC: A computer program for speciation, reaction-path, advection-transport, and inverse geochemical calculations. Technical Report 95-4227. U.S. Geological Survey Water-Resources Investigations Report.

Poonoosamy, J., Wanner, C., Alt Epping, P., Águila, J. F., Samper, J., Montenegro, L., Kosakowski, G. 2018 (online first). Benchmarking of reactive transport codes for 2D simulations with mineral dissolution–precipitation reactions and feedback on transport parameters. Computational Geosciences. doi:10.1007/s10596-018-9793-x

Post, V. E. A., and H. Prommer (2007), Multicomponent reactive transport simulation of the Elder problem: Effects of chemical reactions on salt plume development, Water Resour. Res., 43, W10404, doi:10.1029/2006WR005630.

Presley, T.K. 2005. Effects of the 1998 drought on the freshwater lens in the Laura area, Majuro Atoll, Republic of the Marshall Islands.

Prommer H, D.A. Barry, and C. Zheng. 2003. MODFLOW/MT3DMS based reactive multi-component transport modeling. Ground Water 41, no. 2: 247–257.

Pruess, K. TOUGH2-A General Purpose Numerical Simulator for Multiphase Fluid and Heat Flow. Lawrence Berkeley Laboratory Report LBL-29400, Berkeley, CA, 1991.

Reilly, T.E., and Harbaugh, A.W., 1993, Simulation of cylindrical flow to a well using the U.S. Geological Survey Modular Finite-Difference Ground-Water Flow Model: Ground Water, v. 31, no. 3, p. 489-494.

Robinson, C., L. Li, and H. Prommer. 2007. Tide-induced recirculation across the aquifer-ocean interface: Water Resources Research 43, no. 7.

Rotzoll, K., and C. H. Fletcher (2013), Assessment of groundwater inundation as a consequence of sea-level rise, Nat. Clim. Change, 3(5), 477–481.

Saaltink M.W., J. Carrera and S. Olivella, 2004. Mass balance errors when solving the convective form of the transport equation in transient flow problems, Water Resources Research, 40, W05107, doi:10.1029/2003WR002866.

Sallenger, A. H., Jr., K. S. Doran, and P. A. Howd (2012), Hotspot of accelerated sea-level rise on the Atlantic coast of North America, Nat. Clim. Change, 2(12), 884–888.

Samani N, Kompani-Zare M, Barry DA (2004) MODFLOW equipped with a new method for the accurate simulation of axisymmetric flow. Adv Water Resour 27:31–45.

Simpson, M.J., and T.P. Clement. 2003. Theoretical analysis of the worthiness of Henry and Elder problems as benchmarks of density-dependent groundwater flow models: Advances in Water Resources 26, no. 1: 17-31.

Šimůnek, J., M. Th. van Genuchten, and M. Šejna. 2006. The HYDRUS Software Package for Simulating Two- and Three-Dimensional Movement of Water, Heat, and Multiple Solutes in Variably-Saturated Media, Technical Manual, Version 1.0, PC Progress, Prague, Czech Republic, pp. 241.

Šimůnek, J., K. Huang, and M. Th. van Genuchten, The HYDRUS code for simulating the one-dimensional movement of water, heat, and multiple solutes in variably-saturated media. Version 6.0, Research Report No. 144, U.S. Salinity Laboratory, USDA, ARS, Riverside, California, 164 pp., 1998.

Steefel CI, Yabusaki SB. OS3D/GIMRT: Software for modeling multicomponent-multidimensional reactive transport; user manual and programmer's guide. Technical Report PNL-11166, Pacific Northwest National Laboratory, Richland, WA, 1996.

Stoeckl, L., M. Walther, and T. Graf. 2016. A new numerical benchmark of a freshwater lens: Water Resources Research 52, no. 4: 2474-2489.

Stoeckl, L., G.J. Houben, and E.J. Dose. 2015. Experiments and modeling of flow processes in freshwater lenses in layered island aquifers: Analysis of age stratification, travel times and interface propagation: Journal of Hydrology 529: 159-168.

Stoeckl, L., and G. Houben. 2012. Flow dynamics and age stratification of freshwater lenses: Experiments and modeling: Journal of Hydrology 458: 9-15.

Svyatskiy D. and K. Lipnikov, 2017. Consistent Nonlinear Solver for Solute Transport in Variably Saturated Porous Media. In: Cancès C., Omnes P. (eds) Finite Volumes for Complex Applications VIII - Hyperbolic, Elliptic and Parabolic Problems. FVCA 2017. Springer Proceedings in Mathematics & Statistics, vol 200. Springer, Cham.

Taylor, M. A., F. S. Whyte, T. S. Stephenson, and J. D. Campbell (2013), Why dry? Investigating the future evolution of the Caribbean low level jet to explain projected Caribbean drying, Int. J. Climatol., 33(3), 784–792.

Teeter, J. W. (1995), Holocene saline lake history, San Salvador Island, Bahamas, in Terrestrial and Shallow Marine Geology of the Bahamas and Bermuda, edited by H. A. Curran and B. White, pp. 117–124, Geol. Soc. Am., Boulder, Colo.

Therrien, R., R. G. McLaren, E. A. Sudicky, and S. M. Panday (2005), HydroGeoSphere: A three-dimensional numerical model describing fully-integrated subsurface and surface flow and solute transport, 322 pp., Groundwater Simulations Group, Univ. of Waterloo, Waterloo, Ont., Canada.

UN-OHRLLS. 2015. Small Island Developing States In Numbers: Climate Change (2015 ed.).

Underwood, M.R., F.L. Peterson, and C.I. Voss. 1992. Groundwater lens dynamics of atoll islands: Water Resources Research 28, no. 11.

US EPA, (1998). BIOPLUME III, Natural Attenuation Decision Support System – User's Manual, Version 1.0." Publication No. EPA/600/R-98/010.

USEPA (2003). User's Manual "CHEMFLO-2000, Interactive Software for Simulating Water and Chemical Movement in Unsaturated Soils." Publication No. EPA/600/R-03/008

USEPA (1996) "BIOSCREEN, Natural Attenuation Decision Support System - User's Manual, Version 1.3 (PDF)." (100 pp, 1.15 MB, About PDF) Publication No. EPA/600/R-96/087. August 1996

Vacher, H. L. (1988), Dupuit-Ghyben-Herzberg analysis of strip-island lenses, Geol. Soc. Am. Bull., 100(4), 580–591.

Vacher, H. L., and T. O. Bengtsson (1989), Effect of hydraulic conductivity on the residence time of meteoric ground water in Bermudian- and Bahamian-type islands, in Proceedings of the Fourth Symposium of the Geology of the Bahamas, edited by J. E. Mylroie and D. T. Gerace, pp. 337–351, Bahamian Field Station, San Salvador, Bahamas.

Vacher, H. L., and J. E. Mylroie (2002), Eogenetic karst from the perspective of an equivalent porous medium, Carbonates Evaporites, 17(2), 182–196.

Vacher, H. L., and T. M. Quinn (2004), Geology and Hydrogeology of Carbonate Islands, Elsevier, New York.

Vacher, H. L., and T. N. Wallis (1992), Comparative hydrogeology of fresh-water lenses of Bermuda and Great Exuma Island, Bahamas, Ground Water, 30(1), 15–20.

Waddill, D.W., and M.A. Widdowson. 1998. A three-dimensional model for subsurface transport and biodegradation. ASCE Journal of Environmental Engineering 124, no. 4: 336–344.

Wallis, T. N., H. L. Vacher, and M. T. Stewart (1991), Hydrogeology of freshwater lens beneath a Holocene strandplain, Great Exuma, Bahamas, J. Hydrol., 125, 93–109.

Werner, A.D.; Sharp, H.K.; Galvis, S.C.; Post, V.E.A.; Sinclair, P. Hydrogeology and management of freshwater lenses on atoll islands: Review of current knowledge and research needs. J. Hydrol. 2017, 551, 819–844.

Werner, A. D., Bakker, M., Post, V. E. A., Vandenbohede, A., Lu, C., Ataie-Ashtiani, B., Simmons, C. T., Barry, D. A., 2013. Seawater intrusion processes, investigation and management: Recent advances and future challenges. Adv Water Resour 51: 3-26.

Wheatcraft, S.W., and R.W. Buddemeier. 1981. Atoll Island Hydrology: Ground Water 19: 311–320.

Whitaker, F. F., and P. L. Smart (2004), Chapter 4 Hydrogeology of the Bahamian archipelago, in Geology and Hydrogeology of Carbonate Islands, vol. 54, pp. 183–216, Elsevier, New York.

White, M.D., and M. Oostrom. 2000. STOMP Subsurface Transport Over Multiple Phases, Version 2.0, Theory Guide. PNNL-12030, UC-2010, Pacific Northwest National Laboratory, Richland, Washington.

Widdowson, M.A. 2002. SEAM3D, A numerical model for three-dimensional solute transport coupled to sequential electron acceptor-based biological reactions in groundwater. Documentation and user's guide. Vicksburg, Mississippi: U.S. Army Engineer Research and Development Center.

Woodroffe, C. D. (2008), Reef-island topography and the vulnerability of atolls to sea-level rise, Global Planet. Change, 62(1), 77–96.

Yamano, H., H. Kayanne, T. Yamaguchi, Y. Kuwahara, H. Yokoki, H. Shimazaki, and M. Chikamori (2007), Atoll island vulnerability to flooding and inundation revealed by historical reconstruction: Fongafale Islet, Funafuti Atoll, Tuvalu, Global Planet. Change, 57(3), 407–416.

Zhang, H., Schwartz, F.W., Wood, W.W., Garabedian, S.P. and LeBlanc, D.R. "Simulation of variable-density flow and transport of reactive and non-reactive solutes during a tracer test at Cape Cod, Massachusetts," Water Resources Research, 34 (1), 67-82 1998.

Zheng, Chunmiao, 1990. MT3D, A modular three-dimensional transport model for simulation of advection, dispersion and chemical reactions of contaminants in groundwater systems, Report to the U.S. Environmental Protection Agency, 170 p.

Zheng, C. 1999. MT3D'99, a modular 3D multispecies transport simulator. Bethesda, Maryland: S.S. Papadopulos & Associates, Inc.

Zheng, C. (2009), Recent Developments and Future Directions for MT3DMS and Related Transport Codes. Ground Water, 47: 620–625. doi:10.1111/j.1745-6584.2009.00602.x.

Zheng, C., and G. D. Bennett, 2002, Applied Contaminant Transport Modeling, Second Edition, John Wiley & Sons, New York, 621 pp.

Zheng, Chunmiao, and P. Patrick Wang, 1999, MT3DMS, A modular three-dimensional multi-species transport model for simulation of advection, dispersion and chemical reactions of contaminants in groundwater systems; documentation and user's guide, U.S. Army Engineer Research and Development Center Contract Report SERDP-99-1, Vicksburg, MS, 202 p.